A FIBER-OPTIC CONFOCAL SCANNER
FOR SCATTERING TISSUE

_____

A Dissertation presented to the
Faculty of the Graduate School
University of Missouri

_____

In Partial Fulfillment
Of the Requirements for the Degree

Doctor of Philosophy

_____

by
JEFFREY THOMAS LaCROIX

Dr. Mark A. Haidekker, Dissertation Supervisor

MAY 2009

The undersigned, appointed by the Dean of the Graduate School, have examined the dissertation entitled

A FIBER-OPTIC CONFOCAL SCANNER
FOR SCATTERING TISSUE

Presented by Jeffrey Thomas LaCroix

A candidate for the degree of Doctor of Philosophy

And hereby certify that in their opinion it is worthy of acceptance.

_____
Mark A. Haidekker, Ph.D., Department of Biological Engineering

_____
Gang Yao, Ph.D., Department of Biological Engineering

_____
John A. Viator, Ph.D., Department of Biological Engineering

_____
Ping Yu, Ph.D., Department of Physics and Astronomy

DEDICATION

This work is dedicated to:

Jesus Christ, for His enduring love, guidance, and presence;

My wife Tiffany, for her love and support. The completion of this work is hers as
much as it is mine;

Mom and Dad, for the values and work ethic they have instilled in me;

Jason and Jaime, for showing me what it means to take care of a family;

Rhys, for showing me what it means to be a role model;

All other family and friends for shaping me into the person I am today;

Mark Haidekker for teaching me true engineers know that things are made to be
taken apart;

Gang Yao for showing me to connect what I learn in the classroom to my work,

Ping Yu for introducing me to new research;

And John Viator for giving me a lab to do research and for teaching me balance.

Thank you all for your guidance and support.

ACKNOWLEDGMENTS

I would like to thank the following people at the University of Missouri and the University of Georgia for their help throughout the completion of this work:

-Darcy Lichlyter, *Senior Research Specialist*, UGA

-Jinjun Xia, Ph.D., and William Kisaalita, Ph.D., *Department of Bio and Ag Engineering*, UGA

-Nicolas L'Heureux, Ph.D., *Cytograft Tissue Engineering*, Novato, CA

-Karen Edison, M.D., Jon Dyer, M.D., Louanne Chance, RN, Sue Prenger, RN, and Gretchen Carlisle, RN, *Department of Dermatology*, MU

-Scott Holan, Ph.D., *Department of Statistics*, MU

-Gordon Ellison and Cliff Mongler, *Senior Research Engineering Technicians*, MU

-Pat Harrell and Steve McDonald, *Technical Staff*, UGA

-Sheila Grant, Ph.D., *Department of Biological Engineering*, MU

-David Grant, *Senior Research Design Engineer*, MU

-Linda Little, *Administrative Assistant*, MU

-Kiran Bhattacharyya, *Undergraduate Research Assistant*, MU

TABLE OF CONTENTS

LIST OF FIGURES

viii

LIST OF TABLES

LIST OF ABBREVIATIONS

CCD = Charge Coupled Device

PMT = Photomultiplier Tube

λ = Wavelength

NA_{Obj} = Numerical Aperture of objective lens

n = Index of refraction

z_{min} = Axial resolution limit

S/B = Signal-to-Background atio

SNR = Signal-to-Noise Ratio

μ_s = Scattering coefficient

μ_a = Absorption coefficient

DC = Direct current

CAD = Computer-Aided Design

SMA = Sub Multi Assembly

QWP = Quarter Wave Plate

FC/PC = Fiber Channel/Physical Contact

FC/APC = Fiber Channel/Angle-polished Physical Contact

FWHM = Full-Width at Half-Maximum

OCT = Optical Coherence Tomography

PC = Personal Computer

R^2 = Correlation coefficient

LoG = Laplacian-of-Gauss

MCML = Monte Carlo for Multi-Layered media

IRB = Institutional Review Board

HIPAA = Health Insurance Portability and Accountability Act

A FIBER-OPTIC CONFOCAL SCANNER
FOR SCATTERING TISSUE

Jeffrey T. LaCroix

Dr. Mark Haidekker, Dissertation Supervisor

ABSTRACT

Confocal microscopy has become an important diagnostic tool in examining scattering tissues. The high resolution of confocal microscopy and its optical sectioning capabilities lend itself as a desirable modality in examining structures on the micrometer scale. The presented work offers a prototype device based on the principle of confocal microscopy that is versatile enough to be used not only as a small scale scanner, but adaptable for a wide range of situations. The automated capabilities of the scanner were tested to be used as a method of quality control for tissue-engineered cell sheets, identifying thickness and determining homogeneity. The device was also evaluated as a method of examining scattering in common phantoms of Intralipid and collagen gels, and applied *in vivo* to determine optical effects in intrinsically aged skin. The abilities and shortcomings of the scanner are investigated, and future adaptations of the device are proposed.

CHAPTER 1

INTRODUCTION

1.1 Confocal Microscopy

Confocal microscopy employs the use of spatial filtering techniques in order to create optical slices in a sample. The excitation light (coherent light) is sent through one pinhole placed in a conjugate plane of the focal point of a condenser lens. Backscattered or fluorescent light pass through either a beamsplitter or a dichroic mirror, through an additional aperture, also conjugate through the focal point, to a detector. This kind of filtering, along with tightly focused illumination, rejects backscattered or fluorescent light outside of the focal plane of the objective lens.

Marvin Minsky, inventor of the stage-scanning confocal optical system identified many advantages including a reduction in image blurring due to the scattering of light from a sample, an increase in axial resolution over conventional optical systems, an improvement in the signal-to-noise ratio, and the capability of an axial scan [47]. These advantages have been realized over the years by many research groups identifying that a confocal system essentially reduces the point spread function leading to an increase in resolution [6,66]. It is also these advantages that allows confocal microscopy to be extremely useful in biological imaging, providing versatility in the field of fluorescence [85] and three-dimensional imaging [9]. It has also shown promise for *in vivo* applications [44].

1.2 Confocal Instrumentation

In order to achieve high resolution, there are a few common optical elements among almost all confocal microscopes. These optical elements were arranged in Minsky's original patent application and have continued to show up in modern systems. The following elements are necessary in order to achieve the confocal mechanism, and are shown in Figure 1.1. As these elements are discussed, the plane in which the focus lies of the objective will be referred to as the xy-plane, the signal acquisition of which is known as lateral scanning. Signal acquisition through the optical axis takes place along the z-direction and is known as axial scanning.
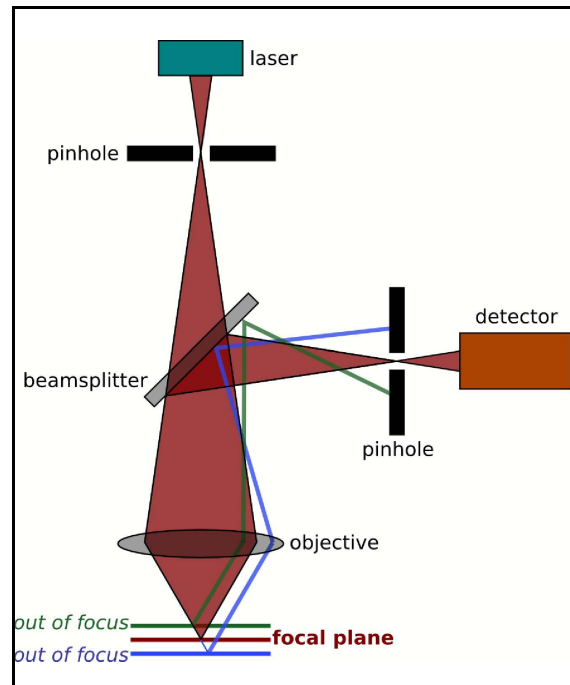
Figure 1.1. Basic principle of a confocal system. The pinhole in front of the detector blocks out-of-focus light.

1.2.1 Light Source

Pointwise illumination is an integral part in the confocal mechanism and is accomplished through the use of a small aperture (pinhole). In biological applications this light source needs to be powerful enough to provide adequate penetration of the sample. Many modern confocal microscopes employ the use of

a laser in order to provide such high power. The use of a laser is especially

significant within fluorescent applications which require a defined wavelength as a

excitation source. The pinhole assures that detected light from the focal plane of the

sample is the same as the focused light.

1.2.2 Beamsplitter

A 50/50 beamsplitter is used in order to redirect the light path that is reflected

or backscattered onto the detector. When non-cubic beamsplitters are used, the

confocal pinhole can eliminate ghost reflections.   In the case of fluorescent

applications, a dichroic mirror usually takes the place of the beamsplitter, allowing

excitation light to pass through the sample while simultaneously reflecting emission

light from the sample. There are typically fluorophore specific dichroic mirror/filter

combinations when the excitation source is broadband rather than a laser.

1.2.3 Microscope Objective Lens

The microscope objective is typically placed in the optical path following the

illumination aperture and the beamsplitter. The objective should be carefully chosen

based on the applications. Spherical aberration has a profound effect on confocal

axial response, and by slightly reducing the aperture of the lens, aberrated axial

response can actually be improved [65]. Magnification and focal length of the

objective can also determine confocal response [71]. The numerical aperture of the

objective characterizes the point spread function, therefore affecting resolution as

well as depth response [34].

1.2.4 Confocal Pinhole

The confocal pinhole is placed in the conjugate focal plane of the objective lens. It is positioned in the reflected path of the light after the beamsplitter in which the optical path from the illumination aperture to the focal plane is equivalent to the optical path from the focal plane to the confocal pinhole, providing there are no index of refraction mismatches. The size of the confocal pinhole governs axial and lateral resolution, and determines the amount of blurring reduced due to light scattering. Typically there is an optimal pinhole size, as an overly large pinhole allows a greater amount of scattered light to reach the detector. Conversely, a pinhole that is too small may decrease the signal-to-noise ratio beyond applicable means.

In the case of spinning disk confocal microscopes, the confocal pinhole is actually a series of pinholes arranged in an Archimedes spiral. The opaque wheel containing these pinholes is known as a Nipkow disk. As the Nipkow disk spins, the sample is scanned in a raster pattern in the xy-plane. The Nipkow disk can be used to obtain a planar section at video rate.

1.2.5 Detector

Reflected or backscattered light from the focal plane that passes through the confocal pinhole is measured with a detector. In the case of spinning disk confocal microscopes the detector may be a CCD camera, or no physical detector may exist as the image may be viewed by the user of the microscope. In other setups requiring a quantitative measurement of reflected or backscattered photons a photomultiplier tube (PMT) or a photodiode is used. While CCD or direct-view may

be able to view samples at video rate, a PMT may be beneficial in detecting weak signals among high background. These detection devices are application specific and further promote the added versatility of a confocal microscope.

1.3 The Effect of the Confocal Pinhole

The confocal pinhole has a profound effect on system resolution, signal-to-background ratio, signal-to-noise ratio, and penetration depth. It is important that the confocal pinhole be chosen based on the desired application of the device.

1.3.1 Resolution

Illumination of the sample is distributed as the point spread function, which is seen as an Airy pattern at the focal point. An Airy diffraction pattern as seen in Figure 1.2 consists of a bright central spot surrounded by concentric dark and bright rings of progressively weaker intensities. The Airy pattern is the result of Fraunhofer diffraction due to a circular aperture and is given by the function

$$\frac{I(ka\sin\theta)}{I_0} = \left(\frac{2J_1(ka\sin\theta)}{ka\sin\theta}\right)^2 \tag{1.1}$$

where J_1 is a Bessel function of the first kind of order one, k is the angular wavenumber (2π divided by the incident wavelength), a is the radius of the aperture, and θ the angle of observation. The radius of the first dark ring after the central spot (r_{Airy}) is given by the equation

$$r_{Airy} \;=\; 0.61\frac{\lambda}{NA_{Obj}} \tag{1.2}$$

in which λ is the wavelength of incident light and NA_{Obj} is the numerical aperature of the objective lens. NA_{Obj} is given by the following

$$NA_{Obj} \;=\; n \sin\Theta \tag{1.3}$$

Iwhere n is the index of refraction of the immersion medium and Θ is the half-angle of the cone of light entering or emerging from the lens. An infinitely small object has an image of a circular Airy diffraction pattern.
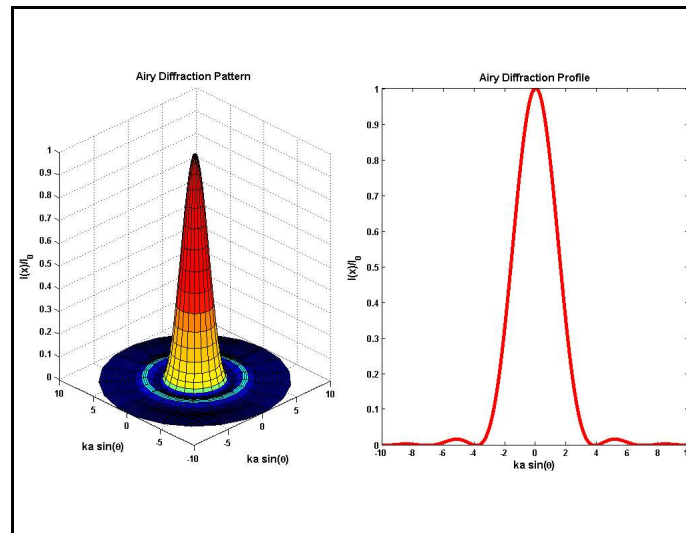
Figure 1.2. Airy diffraction pattern resulting from a circular aperture with accompanying profile. Z-axis units are given in normalized intensity.

When the image of two infinitely small objects are separated by a small distance in the image plane, they are said to be resolvable if the first Airy minimum of one of the objects coincides with the Airy maximum of the other. This is referred

6

to as the Rayleigh criterion for minimum resolvable detail. Here the minimum resolution can be defined as the radius of the Airy disk. If this criterion is met, the imaging process is referred to as being diffraction-limited. This is shown in Figure 1.3.
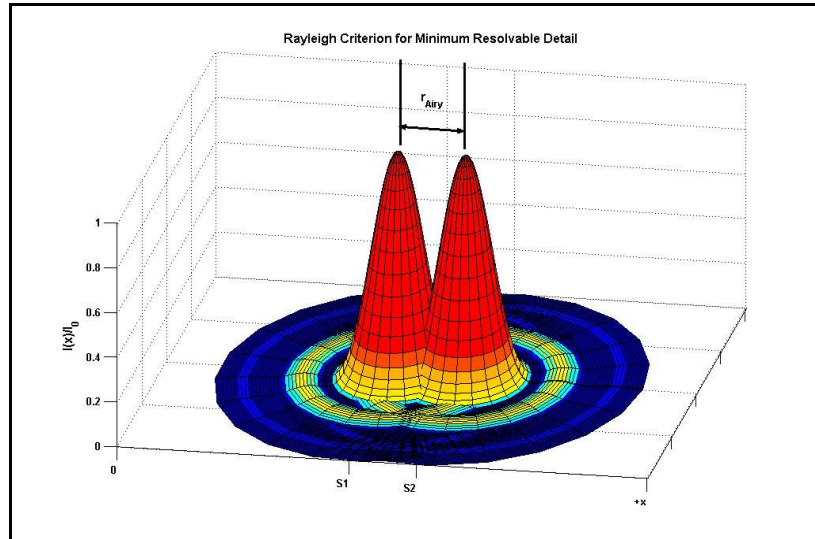
Figure 1.3. Diffraction limited resolution in the lateral dimension is defined where the Airy minimum of one infinitely object *S1* coincides with the Airy maximum of the other *S2*.

Diffraction-limited resolution in the axial dimension applies as well (Figure 1.4), but its reduction is inversely proportional to the square of the numerical aperture. The axial resolution limit z_{min} is given by the equation

$$z_{min} = \frac{2\lambda n}{(NA_{Obj})^2}$$ (1.4)

where in this case **n** is the refractive index of the object medium [33]. The ratio of axial-to-lateral resolution is given by

$$\frac{z_{min}}{r_{Airy}} = \frac{3.279\,n}{NA_{Obj}} \qquad (1.5)$$

demonstrating that lateral resolution will always be smaller than axial resolution.
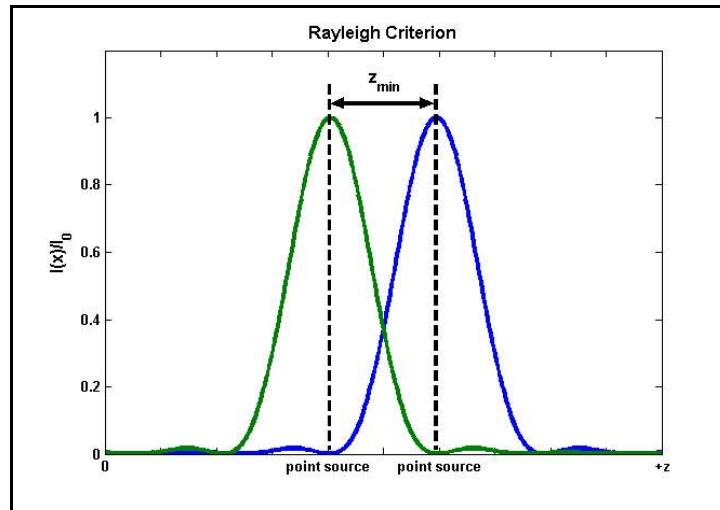
Figure 1.4. Diffraction-limited resolution in the axial dimension shown in terms of intensity signal resulting from focus translation along the z-direction.

When a pinhole is involved, the axial resolution becomes a function of the radius of the confocal pinhole **a** and the magnification of the objective **M**. The 3 dB separation of two focal planes, d_z**(3dB)** is shown by

$$d_z(3\,dB) = \frac{7.4\,n\,a^2}{\lambda\,M^2} \qquad (1.6)$$

per confocal theory[14]. A more rigorous theory for axial resolution taking into account electromagnetic forces along with polarization and detector type is given by

8

Török and Wilson [72]. Additional theory given by Sharma and Sheppard is for the case of using fiber optics in place of pinholes [64].

1.3.2 Background Rejection

In measuring background rejection, one can define the signal-to-background ratio as S/B, with S as the detected intensity of a focused point source from the $1/e^2$ resolution focal volume, and B as scattered light in the image plane collected from outside the same volume. In practice, S/B increases as pinhole radius increases. As mentioned in section 1.2.4, too small of a pinhole results in too little detected light. Opening the confocal pinhole allows more light to pass, but in the process increases B. Essentially, brightfield microscopy can be modeled this way with a confocal pinhole of infinite size. For a circular aperture, the fraction of power ***P(x)/P₀*** contained within circles of radii in the Airy pattern is described by the equation

$$\frac{P(ka\sin\theta)}{P_0} = 1 - J_0^2(ka\sin\theta) - J_1^2(ka\sin\theta) \qquad (1.7)$$

obtained from the integration of Equation 1.1[5]. Assuming that pinhole size is determined by the power contained within these circles of radii, the effect of pinhole size on power output with respect to the Airy function is shown in Figure 1.5. From the expression above, the 83.8% of light is contained in the area bounded by the first dark ring.
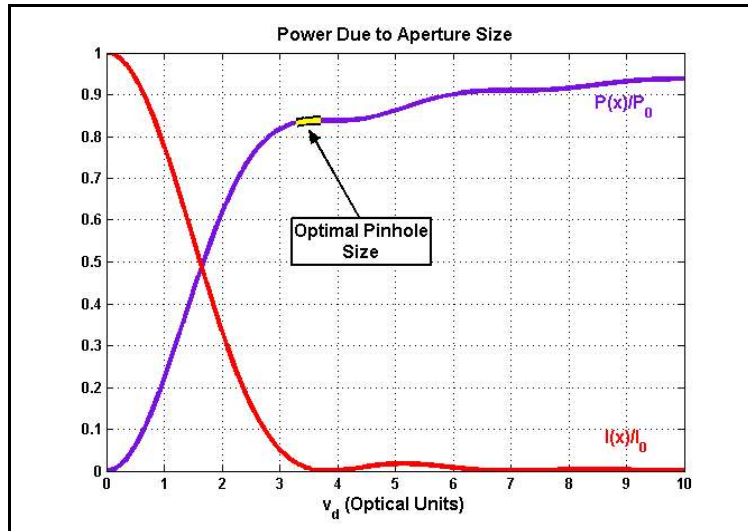
Figure 1.5. Effect of confocal aperture on power (purple) in terms of the Airy function (red). The optimal pinhole size for general biomedical imaging applications in displayed.

Optimum pinhole size varies with wavelength of illumination light, numerical aperture of the objective, and index of refraction of the sample. Sandison and Webb provide an example of optimal pinhole size in their work as a relation to S/B. Typically they found that for a confocal microscope, S/B is 100 times greater than that of a conventional microscope. Signal-to-noise ratio (SNR) for a confocal microscope is also increased by a factor of 10 over a conventional microscope when an optimal pinhole size is used [57]. Due to the variation of equipment, the detector aperture radius v_d is presented in normalized optical units (ou) and calculated according to the following equation:

$$v_d = \frac{2\pi}{\lambda} r_d \left(\frac{NA_{Obj}}{M_{tot}} \right) \tag{1.8}$$

10

where r_d is the distance from the optical axis, essentially the physical size of the confocal pinhole, and M_{tot} is the total magnification in the image plane [1]. M_{tot} is set to one when determining the size of the Airy disk in the image plane. In general biomedical imaging applications, an optimum detector aperture radius would be 3.5 o.u. [58], and is also shown in Figure 1.5 just before the first dark ring of the Airy diffraction pattern. By knowing the desired power needed for imaging purposes from Figure 1.5, one can backcalculate the physical radius from the dimensionless aperture using equation 1.8.

1.3.3 Penetration Depth

Decreasing the radius of the confocal pinhole can theoretically increase the penetration depth of the system due to the reduction of background light that is detected. Smithpeter attempted to verify this concept experimentally, in which his group constructed a confocal reflectometer and measured reflected light as a function of focal depth within a tissue phantom. Their results showed that for a confocal system identifying index of refraction mismatches of 0.05 with dimensionless pinhole $v_p \approx 3$, the signal-to-noise ratio limits penetration depth to approximately 3-4 optical depths (OD), calculated as

$$OD = \mu_t \cdot depth \tag{1.9}$$

where μ_t is a function of scattering coefficient μ_s and absorption coefficient μ_a [69]. They also concluded that for a pinhole of $v_p \approx 8$, the limiting factor is signal-to-

background ratio and penetration depth is determined by scattering coefficient of the sample [69].

1.4 Z-Axis Scanning

As mentioned by Minsky in his original patent application, a scan can be taken through the sample along the optical axis. This is called a z-scan. The optical sectioning capabilities of a confocal system blocks light from outside of the focusing spot. When combined with scans in the x and y directions, it is feasible to create a three-dimensional image based on the reflected or backscattered light collected by the detector. The detector picks up variations in the signal, due to sources of contrast in the sample. For biological tissue, these sources of contrast are typically variations in index of refraction, scattering coefficient and absorption coefficient.

1.4.1 Index of Refraction

If the light during a z-scan passes through one medium to another with a different refractive index, part of the light will be refracted according to Snell's Law

$$n_1 \sin \theta_1 \; = \; n_2 \sin \theta_2 \qquad \qquad \text{(1.10)}$$

where n_1 is the refractive index of the first medium, n_2 is the refractive index of the second medium, θ_1 is the propagation angle of the incident beam and θ_2 is the propagation angle of the refractive beam. Light that is not refracted is reflected at

the same angle of the incident light. The amount of reflection is given by the equation

$$\frac{I_{ref}}{I_0} = \left(\frac{n_1 - n_2}{n_1 + n_2}\right)^2 \qquad (1.11)$$

where I_{ref} is the intensity of the reflected light and I_0 is the intensity of the incident light [10]. The intensity of the reflected light is lower for smaller refractive index mismatches than for larger index mismatches.

The specular reflection of an interface between two mediums shows up as a sharp peak in a z-scan, indicating the intensity of the reflected light. If an object such as a glass slide is placed within the scan path, there will be two sharp peaks indicating the boundaries of the sample. This is confirmed through Monte Carlo simulations [18]. It is also worth noting that while index mismatches as low as 0.05 can be recorded at shallow image depths, the ability to recognize small mismatches is reduced at higher optical depths.

1.4.2 Scattering Coefficient

When performing a z-scan over a sample of turbid media, the scattering coefficient is reflected as a broad peak over the entire sample. As scattering coefficient increases in the sample, the overall signal-to-background ratio increases as well. This is due to an increase in the number of photons that are backscattered to the detector. Monte Carlo scans confirm S/B relationship to scattering coefficient [18].

It is also worth noting that an increase in scattering coefficient results in a degraded performance of optical sectioning capabilities. Essentially, light outside of the focal plane may exhibit multiple scattering events in optically dense samples, and find its way into the focal plane to be scattered back to the objective. In addition to some blurring around areas adjacent to the focus, these multiple scattering events reduces the ability of the confocal pinhole to reject out-of-focus photons [61].

The changes in signal due to the changes of scattering coefficient has enabled some research groups to use confocal microscopy in order to estimate scattering coefficient of various tissues [12,13].

1.4.3 Absorption Coefficient

When light travels through a biological sample, some of the photons will get absorbed due to the absorption coefficient μ_a. The higher the absorption coefficient and the longer the optical path, the greater probability a photon will be absorbed. The absorption coefficient helps define penetration depth in this manner. The amount of light that gets absorbed in a defined optical path is given by the equation

$$I = I_0 e^{-\mu_a t} \tag{1.12}$$

where I is the transmitted intensity and t is the absorption path.

In terms of a z-scan, absorption coefficient translates to a reduction in signal-to-background ratio. This is especially true for high absorbers. For the case of detecting absorption as a source of contrast, while the front edge of a sample can

be recognized by the drop in signal-to-background ratio, the back edge of the sample cannot as easily due to the confocal rejection of the resulting scattered and absorbed photons [18].

1.4.4 Anisotropy

The anisotropy parameter **g** is the average cosine of the scattering angle. It is often derived from the Henyey-Greenstein phase function

$$p(\theta) = \frac{1-g^2}{\left(1+g^2-2g\cos\theta\right)^{3/2}} \tag{1.13}$$

which is a cumulative probability function.

Biological tissue is typically forward scattering, and contrast in a confocal system is generally not affected by the anisotropy parameter [61]. Even so, anisotropy parameter changes little in layered tissues [11].

1.5 Focal Shift Due to Refractive Index Mismatch

Differences in refractive indices of the immersion medium and the sample will produce geometric distortions. The movement of the focus spot is extended when compared to the movement of the objective in the case of entering a medium that has a higher index of refraction than the immersion medium. The ratio of the movement of the focus spot z_2 at the maximum entrance angle α to the movement of the objective z_1 can be derived in terms of **NA** and the indices of refraction of both mediums n_1 and n_2 as

$$\frac{z_2}{z_1} = \sqrt{\frac{n_2^2 - NA^2}{n_1^2 - NA^2}} \qquad\qquad \textbf{(1.14)}$$

derived from the geometry in Figure 1.6 [16,77]. Since objectives are filled with rays incident at all angles between 0 and α, there is a difference between paraxial and marginal rays in cases with high numerical aperture. Conversely, for small aperture objectives, this ratio is essentially $\textbf{\textit{n}}_{\textbf{2}}\textbf{/\textit{n}}_{\textbf{1}}$ [8].
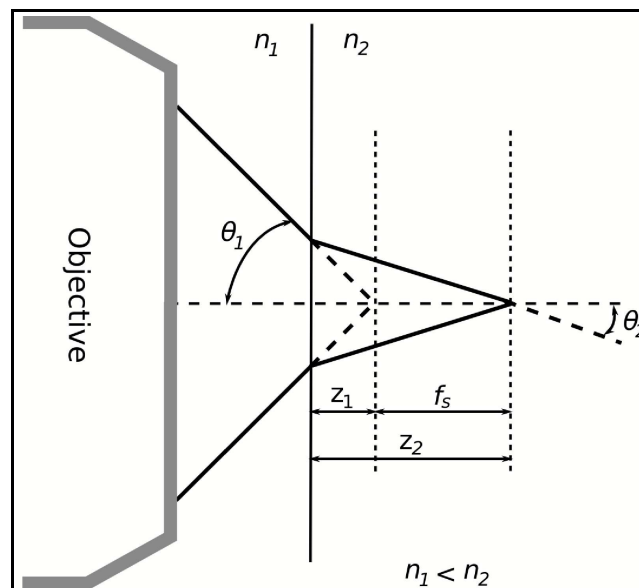
Figure 1.6. Geometric representation of marginal rays bending towards the normal due to entering a medium of higher refractive index, resulting in a focal shift.

The focus shift $\textbf{\textit{f}}_\textbf{\textit{s}}$ is non-linearly dependent on the depth of focus within the sample. However, linear approximations to determine the true geometry can be

used. Efforts to refine calculations have been made to accurately determine this

focal shift for specialized cases in order to still fit a linear model [73].

CHAPTER 2

SCANNER DESIGN

2.1 Introduction

The confocal scanner was originally designed to provide data to determine the thickness and density of a tissue-engineered cell sheet fabricated inside a T225 flask. In order to accomplish this purpose, the scanner must be able to operate on three-independent axes for a complete volume scan. Axial measurement along the optical axis is the most crucial in this case, so much of the design is focused here in order to achieve a high axial resolution in conjunction with a high sampling rate. Transverse resolution may be important around particular areas of interest such as in cases of tissue delamination, but is not nearly as crucial as axial resolution in determining homogeneity of a cell sheet. Transverse resolutions may further be reduced in an effort to forego lengthy scan times.

Our goals called for a design that is not normally found in confocal microscopes, where we take a z-scan along the axial direction, before stepping to an adjacent point. This is opposite of most confocal microscopes, as through a Nipkow disk they record many adjacent points before stepping along the axial direction[33,37]. In order to handle such a task, we designed a rugged XY translational stage to handle the lateral movement as well as to support a heavy Z-stage. An additional goal was to allow the design to be modular so we could transport the device easily if needed.

18

2.2 Original Confocal Scanner Design

Some of the elements described below such as the XY translation stage and the Z translation stage have been incorporated into this and subsequent scanner versions. In this section, our original design is described in detail along with the issues associated with this design.

2.2.1 Design of an XY Translation Stage

The confocal scanner was designed to be used on any metric breadboard or optical table with tapped M6 holes on 25mm centers. The base consists of three aluminum plates of 3/8" thickness measuring 4" x 6" that can be mounted to the optical surface using M6 socket cap screws. The through holes for this purpose are countersunk into the aluminum. Each aluminum plate also contains two threaded #6-32 holes to mount linear motion slides (LMS-600/75 from Small Parts Inc.). The design for these plates was rendered in AutoCAD with units in inches and can be seen in Figure 2.1.

Resting upon the three linear slides was another aluminum plate of 3/8" thickness measuring 14" x 8". This plate was mounted upon the slides using #6-32 screws fitted through twelve countersunk holes, or four for each slide. When tightened down, this plate served to provide a base of motion in what the device would recognize as the X direction as all three linear slides would be aligned moving in uniform direction. This X plate contained four threaded #6-32 holes to
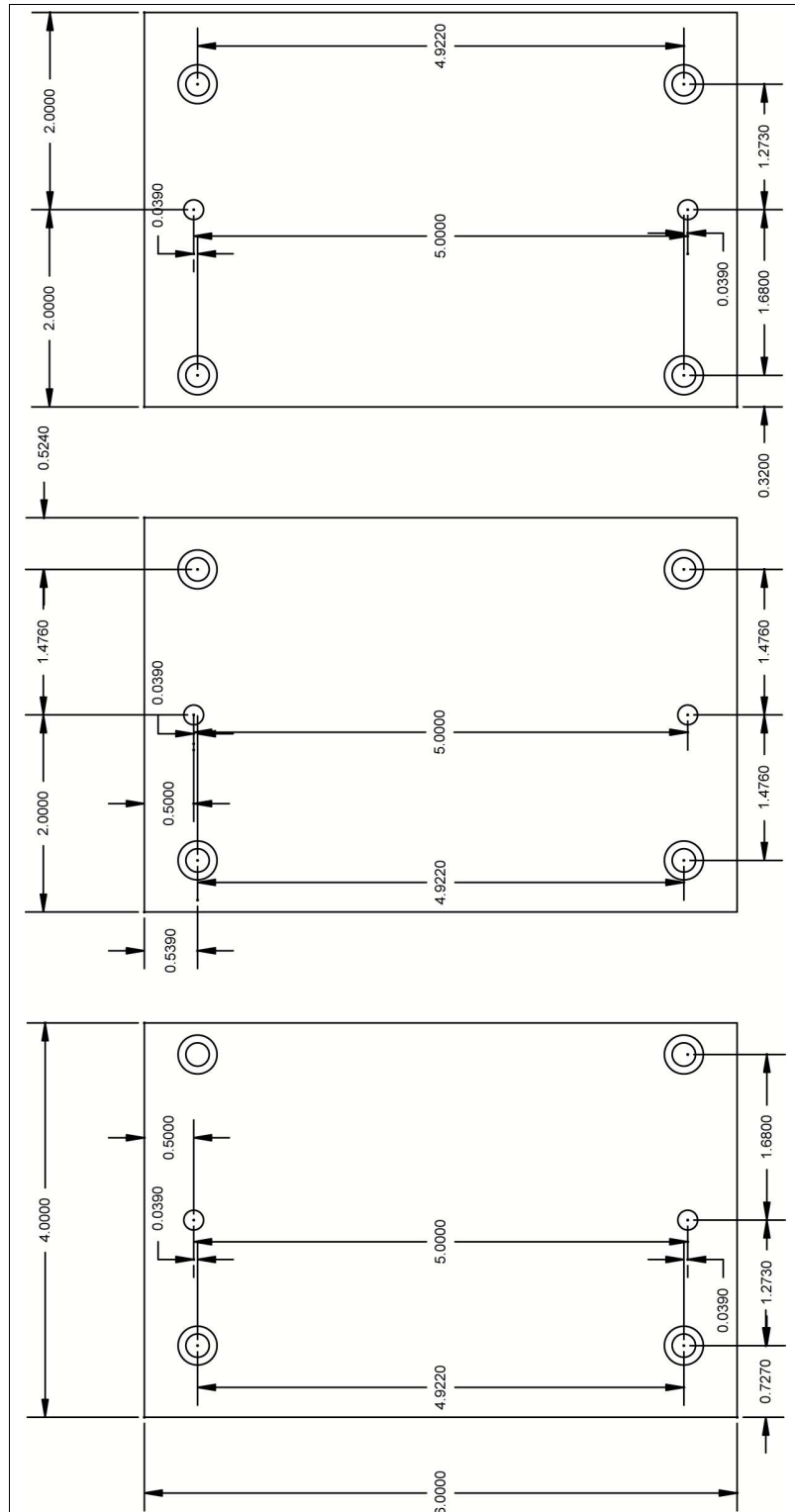
Figure 2.1. Base of confocal scanner. Linear slides are placed on the holes in the center which are used to move the entire apparatus in the X direction.

20

mount linear motion slides in the opposite direction. The design for the X plate was rendered in AutoCAD with units in inches and can be seen in Figure 2.2.

An additional aluminum plate of 3/8" thickness measuring 8" x 8" was mounted upon the two linear slides above the X plate. Eight #6-32 screws were fitted through countersunk holes in order to provide uniform direction and movement of the two linear slides. This plate served to provide a base of orthogonal motion to the X plate and would be recognized as the Y direction by the device. Six holes were used (four threaded, two untapped) to provide stability for a large right angle mounting bracket (AP90RL/M, Thorlabs). A ½" by 1.5" slot was milled to provide spaced for a partially submerged DC motor. In addition, four M3 threaded holes were provided for underside mounting of a circuit adapter for the DC motor. The design for the Y plate was also rendered in AutoCAD with units in inches and shown in Figure 2.3.

The X and Y plates are driven independently by two stepper-driven linear actuators (23A104A, Anaheim Automation) with each half-step traveling 3.175µm. 1 cm of each spindle was machined as a #10-32 thread and threaded into each plate. The X-axis spindle is 6" long, providing approximately 4" of travel, while the Y-axis spindle is 9" long and providing the full 6" of travel allowed by the linear motion slides. This allows a total scan area of 24 square inches, or 155 square centimeters, almost large enough to encompass an entire T225 flask. The linear actuators are driven by custom stepper motor drives and are microcontroller operated. Hard limits are provided when the actuator is fully retracted by means of
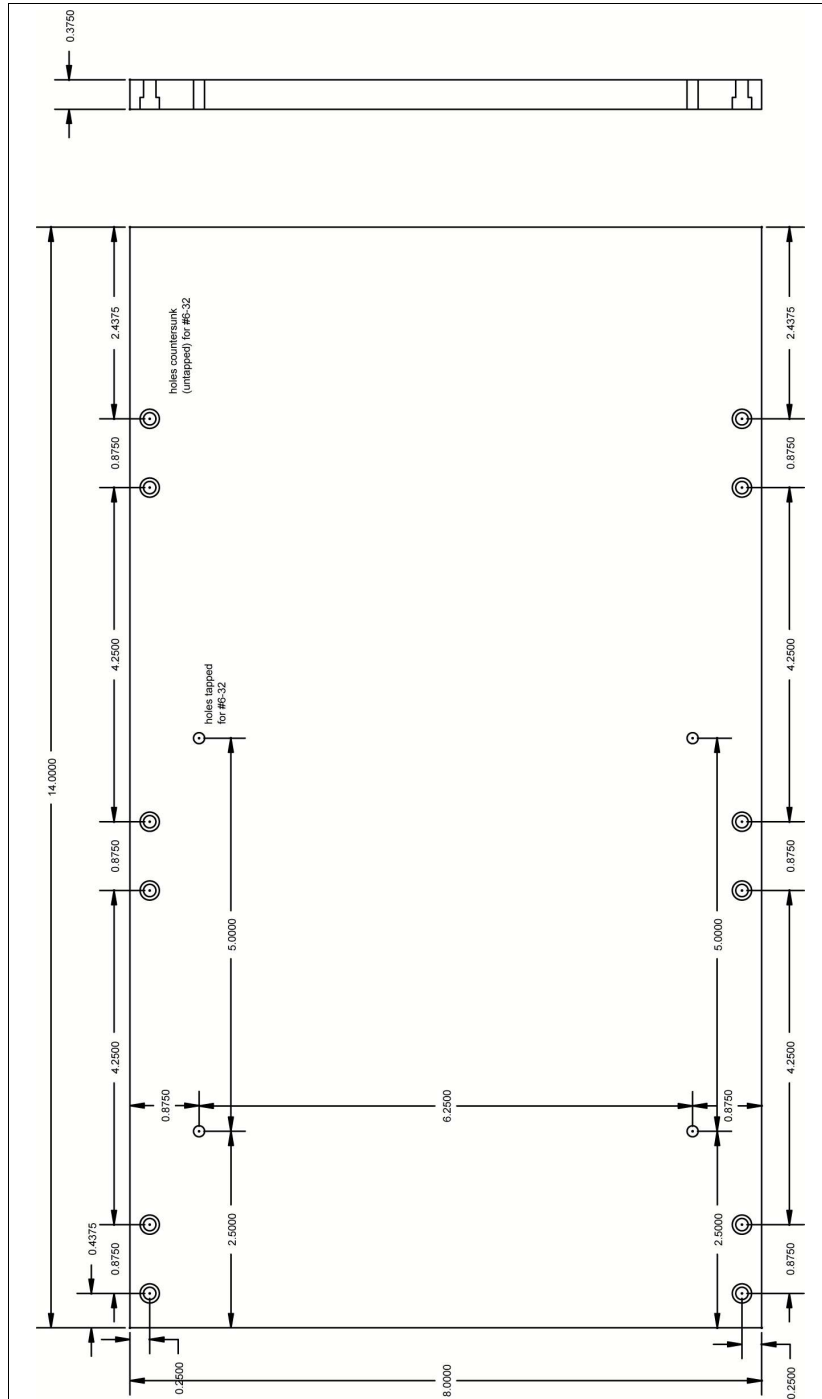
Figure 2.2. Top view and side view of the X plate of the confocal scanner. This plate screws into the three linear slides found on top of the three base plates. Two additional linear slides for the Y plate are mounted on top of the X plate, and move orthogonally to the X plate.
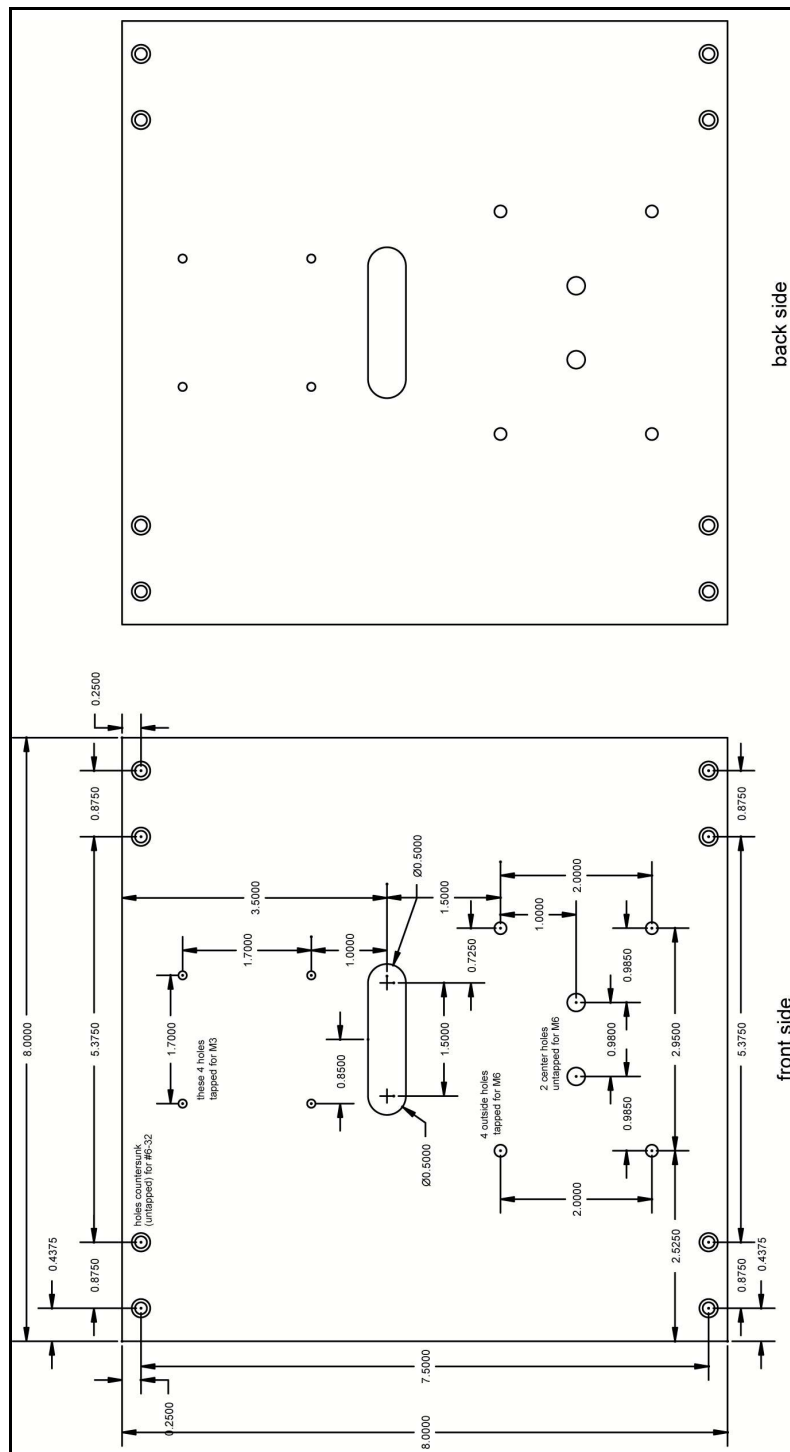
Figure 2.3. Top and bottom view of the Y plate. The Y plate screws into the two linear slides on the X plate and is stepper motor driven. A large angle bracket is mounted to the Y plate that is used to mount the scan head.

an optical switch. Soft limits are provided within the device firmware to prevent the actuator from fully extending into the limits governed by the linear motion slides.

2.2.2 Design of the Z Translation Stage

The base of the Z translation stage was a solid plate of aluminum measuring 5.9055" by 5.3150" (15cm by 13.5cm) with thickness of ½". Slightly off center, four countersunk holes in a square pattern were drilled in order to accommodate M6 screws. These screws fastened to a motorized translation stage (Thorlabs MT1-Z6) which was in turn fastened to the large angle bracket. This ensured that as the DC actuator raised and lowered the translational stage, the entire Z stage containing all necessary optics would rise with it.

Four holes were drilled in an offset T-pattern and countersunk from the back side of the plate. This allowed four mounting posts holding the optical system to be mounted directly to the plate without the use of post holders. By mounting directly to the posts, we ensure that all vibrations occurring in the optical system occur together. In addition, there is no risk of the heavy optical system slipping out of the post holders. A complete AutoCAD rendering is presented in Figure 2.4 with all units shown in inches.

In order to support the weight of the Z stage and all of the accompanying optics, a small pulley was mounted to the top of the large angle bracket. A small steel cable was attached to the top of the Z plate and pulled over the pulley. At the other end of a cable, a spring was attached which had a coefficient that could counterbalance the entire weight of the system. In addition, the recoil springs were

removed from the motorized translational stage in order to ensure that the only downward force acting on the plate and accompanying optics was gravity. The balance created by the spring and pulley system ensured that no unnecessary stress was added to the actuator driving the Z stage.
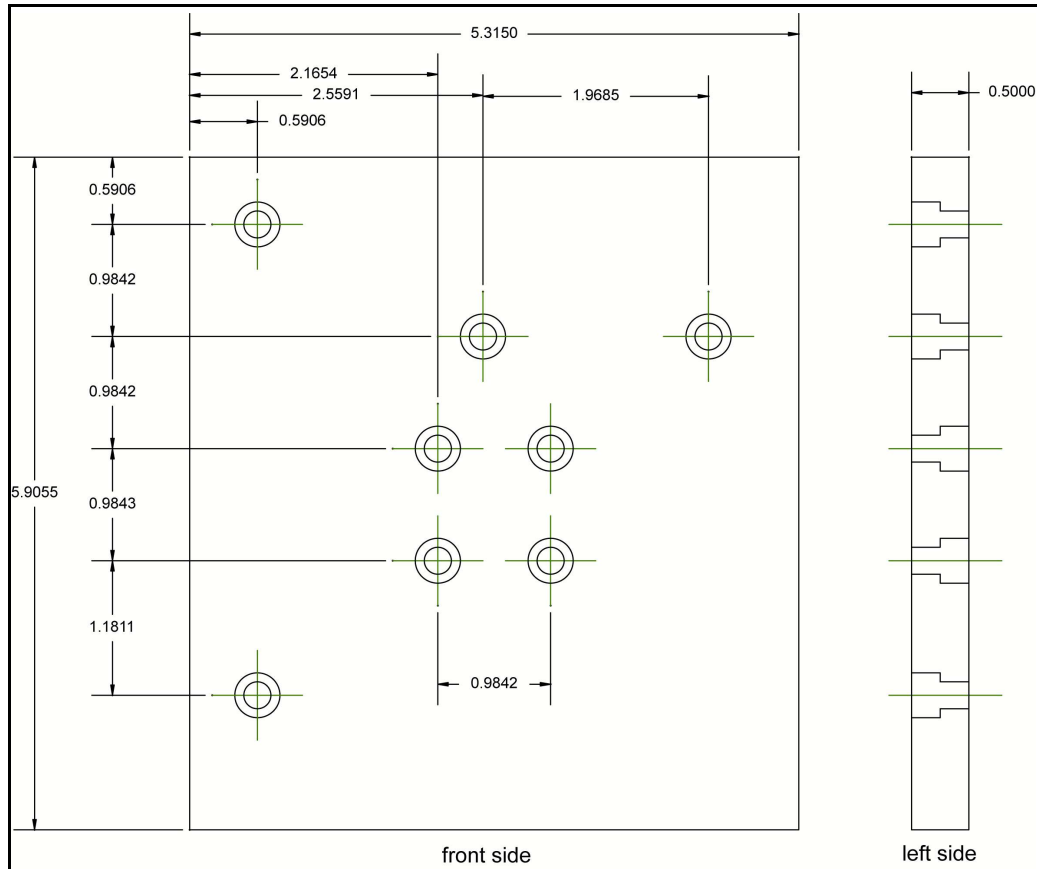
Figure 2.4. Front and side view of the Z-plate that formed the base of the scan head. The four holes in the center were used to anchor the Z-plate to the motorized translational stage mounted on the large angle bracket.

2.2.3 Design of Optics

A 30mm optical cage system was used to mount all optics in order to ensure that all reflected light would be orthogonal to the primary beam path. The complete

design is shown in Figure 2.5. At the heart of the optical path was a cube-mounted polarization-insensitive beamsplitter (Thorlabs CM1-BS1) designed for wavelengths in the visible spectrum. Cage rods (Thorlabs ER series) were used to align cage plates (Thorlabs CP02/M and CP02T/M) designed to incorporate 1" optics and threaded internally at 1.035"-40. These cage plates also accepted metric posts, which were mounted onto the Z plate. All descriptions used in this section are given looking at the optical system head on with the Z-plate in the back. The bottom of the cage system is closest to the XY stage, while the top of the cage system is nearest to the sample to be measured.

A kinematic mirror mount (Thorlabs KCT-1/M) was used to mount the 670nm laser which allowed for fine tuning and alignment, and was positioned at the bottom of the cage system. The laser was focused through a 50µm pinhole (Thorlabs P50S) which was mounted in a micrometer-driven cage plate (Thorlabs SM1Z) allowing for up to 1.5mm travel. Light exciting the pinhole then passed through the beamsplitter to a nearby focusing lens before finally reaching the microscope objective.

The microscope objective chosen for our design was a Mitutoyo 100X objective with numerical aperture of 0.70 and a working distance of 6mm (Edmund Optics NT46-147). The 6mm working distance provided ample room for maneuverability when accommodating samples inside of a thick flask. In order to mount the objective to the cage plate, an adapter was used to accommodate the cage plate threads to an RMS thread, followed by an additional adapter used to

convert the RMS to the Mitutoyo threading of 26mm at 36 TPI (Edmund Optics

NT58-296).

Focal Plane

Microscope
Objective

Adapter

Lens

Beamsplitter

PMT

Support
Rods

XY Translation
Stage w/ Pinhole

Z Translation
Stage w/ Pinhole

Kinematic Laser
Mount
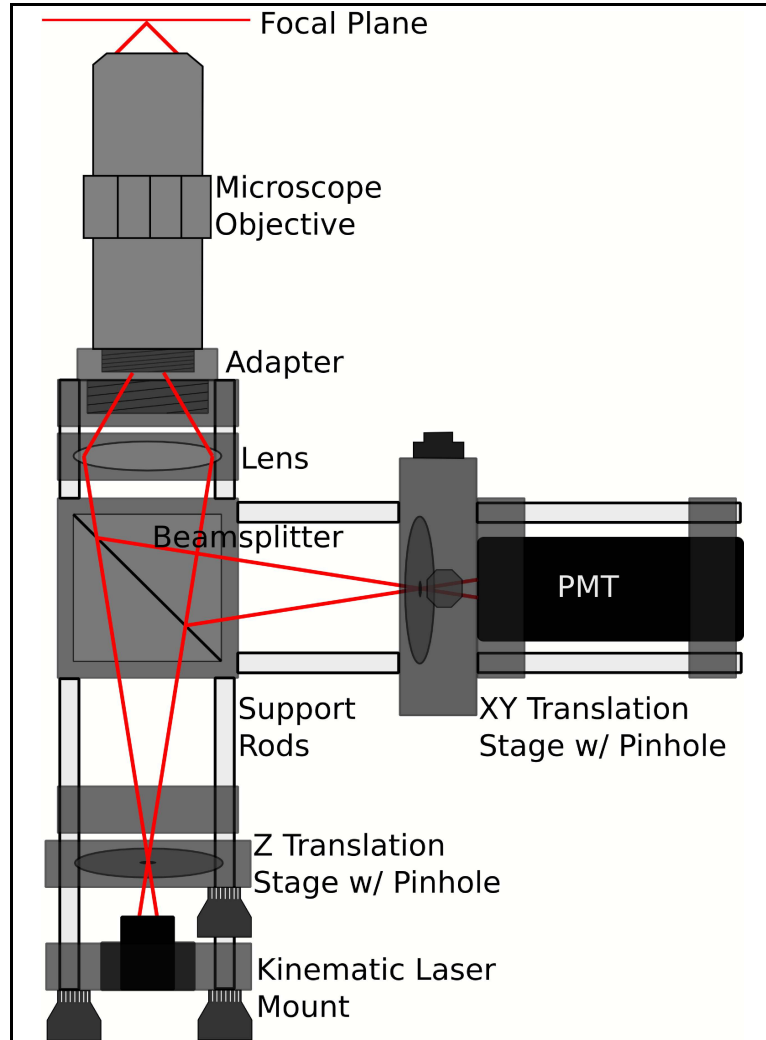
Figure 2.5. Scan head consisting of free space optics. All
optical elements are mounted in 30mm cage plates and
supported by rods.

When light is reflected or scattered in the focal plane, the light returns through

the microscope objective and is reflected by the beamsplitter. At the same linear

distance from the illumination pinhole, another 50µm pinhole is placed inside of an

XY translation mount designed to work with the cage systems (Thorlabs ST1XY-A). This allows for fine adjustment of the confocal pinhole so that it is properly aligned inside of the beam path. Behind this mount is our detector, which we have chosen to be a photomultiplier tube (Hamamatsu Photonics H5784-20) due to the low amount of light due to scattering.

2.2.4 Alignment of Optics

Alignment of the confocal system proved to be a rather daunting task, and was one of the reasons this original optical design was discarded. The microscope objective was removed and in its place a CCD camera was mounted. The PMT was also removed, and a laser was added behind the confocal pinhole with the ability to be mounted inside of the XY translation mount. As the lasers exited the pinholes, a diffraction pattern emerged and was detected by the CCD camera. This CCD camera was hooked up through a television monitor for real-time alignment.

In order to accomplish alignment in the XY directions, the leadscrews of the XY translation mount were turned so that the diffraction patterns from each of the lasers overlapped. Once this adjustment had been made, the microscope objective was replaced and the PMT was added back into the system. A highly reflective mirror was placed in the focal plane of the objective, so most of the illumination light would return through the optical system. The PMT was hooked up to an oscilloscope in order to monitor light intensity. More fine adjustments were made with the leadscrews in order to maximize the intensity of the light reaching the PMT. Once this maximum was attained, the confocal pinhole was assumed to be aligned

28

in the XY direction, and the setscrews of the XY translation mount were tightened in order to prevent any slipping of the confocal pinhole.

Alignment of the direction of the optical path (denoted as Z alignment) was achieved using the micrometer-driven cage plate attached to the illumination pinhole. Originally, this was aligned by taking a single axial Z-scan over the reflective mirror and calculating the full-width at half-maximum (FWHM) of the signal. The micrometer-driven cage plate was then adjusted, and the mirror was rescanned. When the FWHM of the signal was at a minimum, it was assumed that both pinholes lied in the conjugate plane of the objective, and the system was aligned. However, this method was tedious and unreliable due to the limitations of the software at the time, and the inability to zero-in on the exact spot to achieve confocality.

In order to overcome this problem, the afore mentioned method of using a CCD camera and two lasers was used. The laser behind the confocal pinhole was turned on, while the illumination laser was turned off. The resulting diffraction pattern was recorded by the use of a frame grabber. Pixel analysis was used in order to determine the distance between the second minimums across the diameter of the diffraction pattern, as shown in Figure 2.6. Once this distance was determined, the laser behind the confocal pinhole was then turned off. The illumination laser was turned on in its place, and the resulting diffraction pattern was recorded. Pixel analysis was then used to determine its distance between second minimums. If the distances matched, the pinholes were assumed to be in the conjugate focal plane of the objective. If not, the micrometer-driven cage plate was then adjusted until this distance was calculated to be the same. Once alignment

was complete, the laser behind the confocal pinhole was removed for the PMT and the objective replaced.
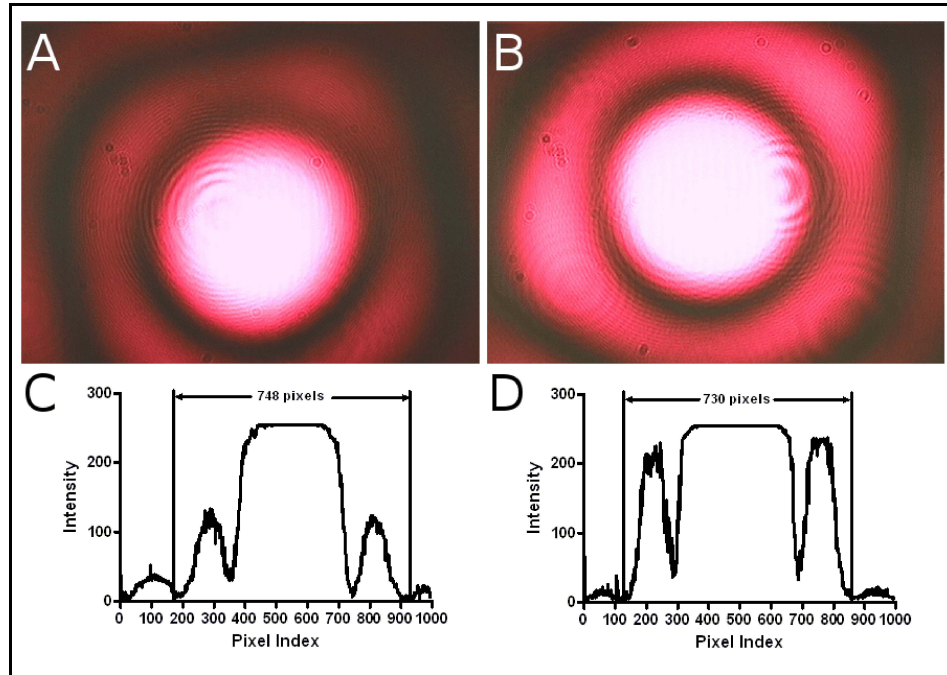
Figure 2.6. Technique to align the two pinholes. (A) CCD camera image of the diffraction pattern resulting from the laser exiting the illumination pinhole. (B) Similar image of the pattern from the confocal pinhole. (C) Profile of the diameter of the diffraction pattern in A. (D) Profile of B.

2.2.5 Difficulties with Free-Space Optics

As mentioned in the previous section, the primary drawback to using the free-space optics in this setup was the alignment. Perfect alignment of both pinholes was not only tedious, but was limited to the capabilities of the CCD camera and valley finding algorithms, and mostly to the eye of the operator. In addition, frequent scans resulted in slight shifts in the optical system, meaning that after a multitude

of scans, the system had to be realigned. Since, the system needed to be designed with an untrained end user in mind, frequent realignment was certainly undesirable.

The second major drawback was the weight of the system. Due to the size of the optical system and the Z plate it was mounted on, the force of gravity acting on the scanning stage was overpowering for the driving actuator. This put extreme strain on the actuator itself, resulting in an extremely slow scan speed along with frequent jamming of the actuator spindle. While the spring and pulley system worked to reduce this weight, a suitable system was unable to be found in order to completely counteract the gravitational forces. Even so, no decent way of mounting such a system existed, resulting in a positioning that was unaesthetic to the end user. Aside from the visual aspects of the spring and pulley system, this too had to be constantly readjusted in order to keep the spring from overstretching and losing its spring constant. It was a combination of these two aspects that led to a complete overhaul of the optical designs.

2.3 Improvement of the Optical System

In order to progress the confocal scanner and make it marketable to an end user, the issues of scan head weight and alignment needed to be addressed. In reducing this weight and eliminating alignment, we were able to make an attractive product for the end user.

2.3.1 Incorporation of Fiber Optics

In order to reduce the weight of the scan head, fiber optics were used in place of the pinholes. In each case, a 50 μm multimode patch cable (Thorlabs M14L01) with SMA termination was mounted to the micrometer-driven cage plate on the illumination side and the XY translation mount on the detector side. The laser was moved to the optical table (breadboard) away from the scan head and coupled into the fiber. The PMT was also removed from the scan head onto the optical table. The fibers were screwed into adapters compatible with the cage mounts (Thorlabs SM1SMA) and shown in Figure 2.7.   This technique has been accomplished by previous research groups[64] so its adaption to our system was the next logical step.

While utilizing fiber optics instead of traditional pinholes reduced the weight somewhat, a great amount of pressure still rested on the motorized actuator. However, incorporating these fiber optics did nothing to enhance alignment. In fact, because these were multimode fibers, there was no diffraction pattern in order to properly align them along the optical axis. In addition, the speckle pattern produced by using a single-wavelength light through the optical fiber made it that much more difficult to align the system.
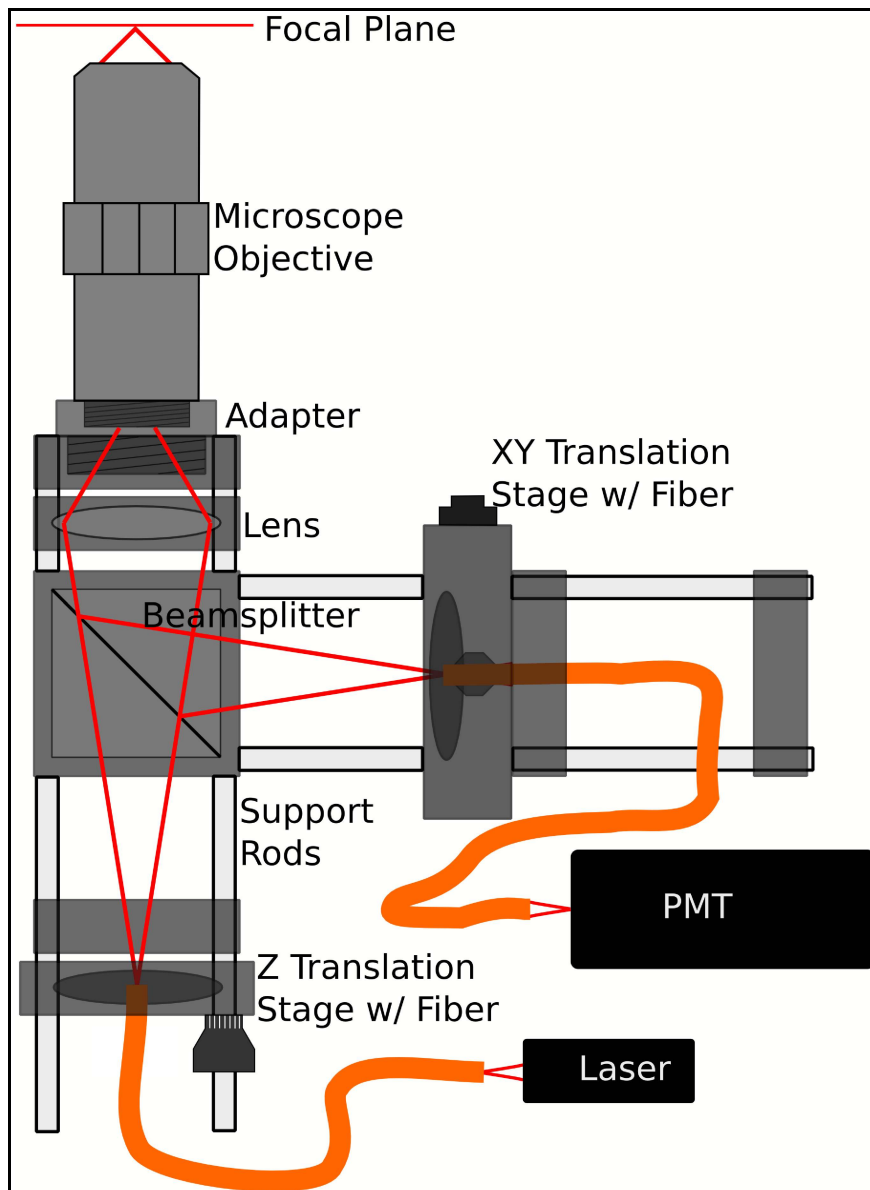
Figure 2.7. Scan head incorporating fiber optics. The fiber optics take the place of the pinholes in this case. Note that the PMT and Laser are not part of the scan head, but rather mounted on the XY stage.

2.3.2 Single Pinhole System

Our major solution for alignment resting in moving towards a single pinhole system, where one pinhole placed in the conjugate focal plane of the objective would act as both the illumination pinhole as well as the confocal pinhole. The benefit here is obvious as any alignment of the pinhole would essentially disappear since confocality would be achieved right from the start. In terms of setup, the orignal illumination and confocal pinholes would be removed. After the beamsplitter and before the objective, the single pinhole would be placed inside the optical system. By orientation of the beamsplitter, reflected or backscattered light passing through the pinhole would reach the PMT and be detected.

While this system completely eliminates the need of alignment, there were a few drawbacks that made it unfeasible. These problems resulted from an inability to reject background light. Since the PMT was no longer covered by a pinhole, a greater amount of ambient light was detected, therefore drastically reducing signal-to-background. While light-proofing the scan head could eliminate the ambient light, ghosting from the beamsplitter also contributed to the background. In addition, light reflecting from outside of the pinhole was reflected by the beamsplitter to the detector. Because this device is not used for fluorescent applications, there are no filters present to block out this illumination light. While possible to introduce a larger pinhole in order to account for the ghosting or pinhole reflections, the aspect of alignment has reentered the equation, thus negating the prospect of using a single-pinhole.

2.3.3 Polarization Dependent Single-Pinhole System

In order to address this problem, we used the concept of polarization in order to reduce or eliminate these unwanted reflections. A linear polarizer was positioned in front of the illumination laser in order to convert the light to a linear polarized state. An additional linear polarizer was positioned in front of the PMT, orthogonal to the first linear polarizer. Essentially, this drastically reduced the amount of light due to ghosting and unwanted reflections, as long as the polarizers are of good quality.

For backscattered or reflected light in the focal plane of the sample to be detected by the PMT, the light must be polarized at the same angle as the linear polarizer in front of the detector. In order to accomplish this, a quarter wave plate was positioned between the pinhole and the objective with the fast axis positioned at an angle 45 degrees from the linear polarizer. When linear polarized light passes through the pinhole, the quarter wave plate converts this light to a circular polarization state. Since the reflected light maintains its polarization state, it passes through the quarter wave plate again and is converted back to linear polarized light. The polarization angle is now 90 degrees from the first linear polarizer, allowing it to pass through the polarizer positioned in front of the detector, shown below using Mueller calculus.

$$
\begin{bmatrix} \frac{1}{2} \\ 0 \\ \frac{1}{2} \\ 0 \end{bmatrix}_{-45^\circ linear} = \begin{bmatrix} 1 & 0 & 0 & 0 \\ 0 & 1 & 0 & 0 \\ 0 & 0 & 0 & -1 \\ 0 & 0 & 1 & 0 \end{bmatrix}_{QWP} \begin{bmatrix} 1 & 0 & 0 & 0 \\ 0 & 1 & 0 & 0 \\ 0 & 0 & 0 & -1 \\ 0 & 0 & 1 & 0 \end{bmatrix}_{QWP} \begin{bmatrix} \frac{1}{2} & 0 & \frac{1}{2} & 0 \\ 0 & 0 & 0 & 0 \\ \frac{1}{2} & 0 & \frac{1}{2} & 0 \\ 0 & 0 & 0 & 0 \end{bmatrix}_{+45^\circ linear} \begin{bmatrix} 1 \\ 0 \\ 0 \\ 0 \end{bmatrix}_{unpolarized} \qquad \textbf{(2.1)}
$$

This process allows for signal-to-background that was comparable to that using two pinholes.

The major drawback of this design was due to the need to remount the laser and detector to the scan head, increasing the weight of the device. As mentioned previously, this provided added strain to the motorized actuator. In addition, while the concept of utilizing the polarizer and quarter wave plate combination was mostly successful, the extinction of the background light was not sufficient on preliminary testing. When combined with the issue involving the weight of the scan head, this idea was ultimately discarded.

2.4 Fiber-Optic Confocal Scanner

The final design of the system incorporates the many of the aforementioned ideas while specifically addressing the issues of alignment and scan head weight. It was important to be able to have a design that was somewhat modular and easy to transport while maintaining an ease of setup and operation.

2.4.1 Fiber-Optic Coupler

The final design involved replacing the beamsplitter and pinholes with a 50 μm fiber optic coupler (AC Photonics custom order). The fiber optic coupler (also called a splitter) has three ports. Two entrance ports (A and B) feed into an exit port (C) . Light coupled into ports A and B combine and exit port C. The device is passive and bidirectional, so light entering port C is split between ports A and B.

Therefore, the intensity of the light exiting port A is half of the intensity entering port C. The bidirectional properties of the fiber-optic coupler allow it to be an extremely marketable choice for maintaining the functionality of the confocal system.

As shown in Figure 2.8, port C replaces both pinholes in the free-space optical system and acts as a single pinhole, and idea used by prior research groups[15,35]. This immediately addresses the issue of alignment. As mentioned in the previous sections, with a single pinhole there is no need for alignment. The coupler itself acts as a beamsplitter, but without unwanted ghosting effects. While there is some crosstalk between ports A and B, the increase in background compared to signal is negligible. The illumination laser is coupled into port A while port B exits to the PMT.
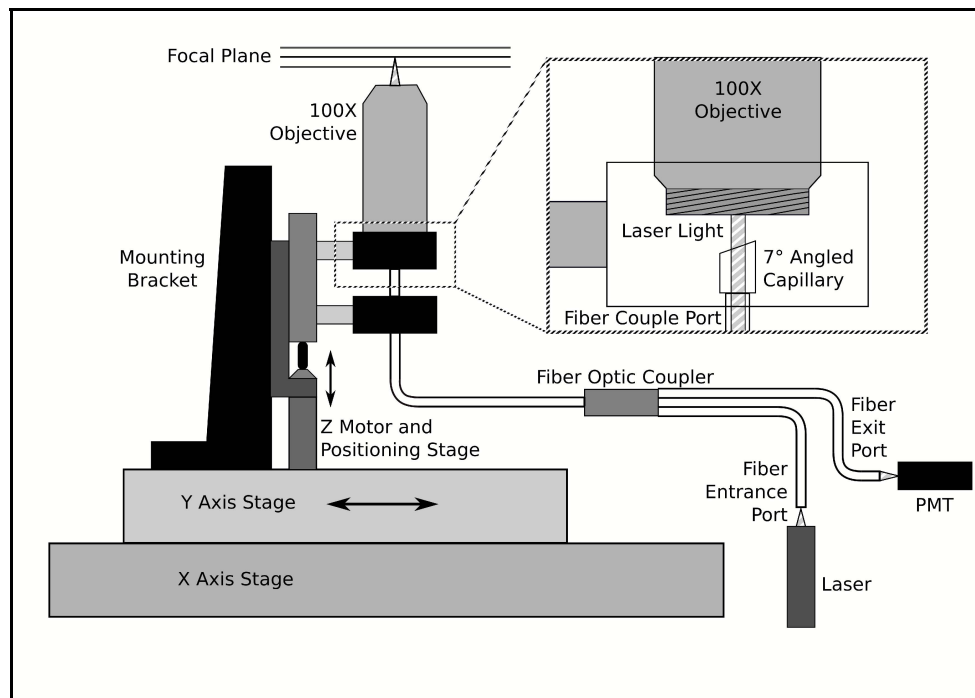
Figure 2.8. Schematic of the confocal system using a fiber optic coupler instead of free space optics. The fiber optic coupler acts as a single-pinhole system, dramatically reducing weight and system alignment. Inset: View of the fiber exit port and capillary.

The use of the fiber addresses the weight issue as no longer are the laser, beamsplitter, PMT, or mounting hardware part of the scan head. In addition, the Z-plate is no longer needed due to the footprint reduction of the scan head. The scan head only consists of port C of the fiber and the proper mounting of the objective lens. This reduction of the weight allows for the motorized actuator to move more freely and drastically reduces the likelihood of jamming.

Using a fiber optic coupler also eliminates the reflections at the pinhole which cause an increase in background. However, there is a similar phenomenon dealing with specular reflection at the interface of port C to the air. Specular reflected light travels back through the coupler and is split to be detected by the PMT. This results in a dramatic increase in background. In order to avoid this issue, port C was incased in a capillary and polished off at a 7 degree angle and coated with an anti-reflective material. This assured that any light specular reflected would not maintain total internal reflection and would be absorbed by the fiber cladding. The capillary was part of the custom design by AC Photonics.

In order to hold the capillary in place, a piece of delrin was machined to fit inside of a fiber collimator adaptor (Thorlabs AD11F). The delrin was machined to have a radial slot from a center hole. The center hole was about the same diameter as the capillary. When the fiber collimator adaptor was screwed down, the slot in the delrin compressed to hold the capillary in place. In this matter, the capillary was not damaged from excessive force.

2.4.2 Objective Lens

The microscope objective lens was also upgraded to allow thicker samples to be scanned. An 80X Mitutoyo objective (Edmund Optics NT46-400) with numerical aperture of 0.5 and working distance of 15mm was chosen for this case. The long working distance of this objective makes it possible to image samples inside of a flask or well plate that is up to 1 cm in thickness, without a significant compromise in resolution. It also provides the opportunity to add additional optical elements between the objective lens and the sample. The addition of this objective greatly improves the versatility of the confocal scanner.

2.4.3 Single-Mode Fiber

While the 50 µm multimode fiber accomplishes its goal of providing a versatile system with no alignment, axial resolution is not as high as desired. When scanning over a coverslip, the resulting peak has a full-width at half-maximum of between 25-30 µm. In order to achieve higher resolution, a smaller fiber would need to be used. This would in turn reject more out-of-focus light, improving not only the axial resolution, but increasing penetration depth as well.

In order to ensure that ample illumination light was present in a small fiber, and because coupling light into a single-mode fiber can be tedious, we opted to use a pigtailed laser diode (Thorlabs LPS-660-FC). The fiber is a single-mode fiber with FC/PC termination and has an output power of 7.5 mW with a wavelength of 660nm. This fiber was coupled to a single-mode coupler (Fiber Optic Network Technology Co. custom part) by use of a bulkhead. The coupler had FC/PC termination at the

PMT end (Port B) and utilized FC/APC termination at the objective end (Port C). The FC/APC termination is polished at an 8 degree angle in order to prevent specular reflection, in the same was as our fiber capillary. An adaptor (Thorlabs SM1FCA) was used to mount Port C behind the objective. This mount was angled at 4 degrees to ensure that the optical axis was perpendicular to the face of the objective.

The benefits of the single-mode fiber are noticed in the increased axial resolution. Scanning over a coverslip shows a FWHM at the air-to-glass interface to be less than the FWHM scanned by a multimode fiber, as shown in Figure 2.9. However, a drawback of using a
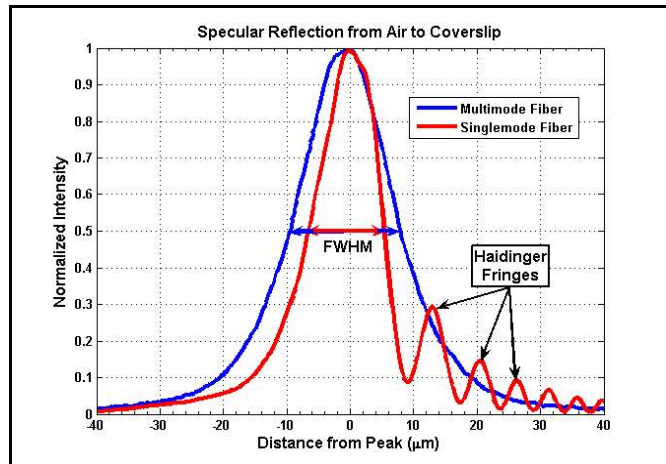
Figure 2.9. FWHM comparison between multimode and singlemode fibers. Haidinger fringes are averaged out by the multimode fiber.

single-mode fiber is the noticeable appearance of Haidinger fringes. In the case of a larger, multimode fiber these fringes are averaged out and blend into the FWHM of the resulting signal. Since resolution is dramatically increased, and since we are using a monochromatic light source these fringes become visible.

2.5 Specialized Additions

Since the confocal scanner was designed with versatility in mind, there is an ability to incorporate various optical components in order to adapt the scanner to a specialized application. These additions are meant for the final design using the fiber optic coupler, and as such are not intended for fluorescent use. This is because the fiber optic coupler is rated for monochromatic light at 660nm. While possible to adapt such a system to fluorescent applications by using wavelength dependent filters, it is beyond the scope of this scanner.

2.5.1 Backscattering Only

In some imaging cases, it may be necessary that the only source of contrast be scattering coefficient. In this situation, any contrast that arises from index of refraction changes need to be blocked out. This contrast is a result from specular reflection, and can be easily removed.

By adapting a similar method found in section 2.3.3, we can effectively eliminate specular reflection. Following the exit of the optical fiber, a circular polarizer is placed before the objective. This circular polarizer consists of a linear polarizer and a quarter wave plate. The fast axis of the quarter wave plate is positioned at a 45 degree angle from the axis of the linear polarizer. As mentioned before, linear polarized light is turned circular by the quarter wave plate. As reflected light passes back through the quarter wave plate, the polarization state

becomes linear again, but at a 90 degree angle to the original linear polarization state. This effectively blocks specular reflected light.

In our device, we used a glass linear polarizer (Edmund Optics 47216) and a zero-order quarter wave plate (Thorlabs WPQ05M-670) for our circular polarizer. With this device, we achieved an extinction ratio of approximately 5000:1.

2.5.2 Rotational Scanning

One of the major drawbacks with using a motorized actuator is the slow scan speed. A typical scan takes about 10-15 seconds depending upon the length of the scan. In order to compensate for this, we have designed an optical wedge for use in axial scanning. Due to the law of refraction, light passing into an optically denser medium bends towards the normal. When the cone of light from an objective passes through an object where there is a refractive index mismatch, a shift in the focal length of the objective occurs. An example of this phenomenon would occur when a glass plate is placed after the objective but before the focal point. The focal point will become longer due to the higher optical density of the glass plate. A thicker glass plate will shift the focal point f_{new} even further away from the objective according to the following equation

$$f_{new} = f_0 + x_g \left(1 - \sqrt{\frac{1 - NA^2}{n_g^2 - NA^2}} \right)$$

(2.2)

where f_0 is the original focal length of the objective, NA is the numerical aperture, n_g is the refractive index of the glass, and x_g is the thickness of the glass. The equation holds true provided that

$$x \leq f_0 \sqrt{\frac{n_g^2 - NA^2}{1 - NA^2}} \tag{2.3}$$

otherwise the focus will be inside of the glass. In this case, the immersion medium of the objective is assumed to be air.

Our design for rotational scanning calls for a glass disk that when viewed from the side carries the shape of a wedge (Vitriforms Custom Order), the design of which can be seen in Figure 2.10. The glass is mounted on a DC motor to rotate it so that glass in front of the objective becomes thicker as it
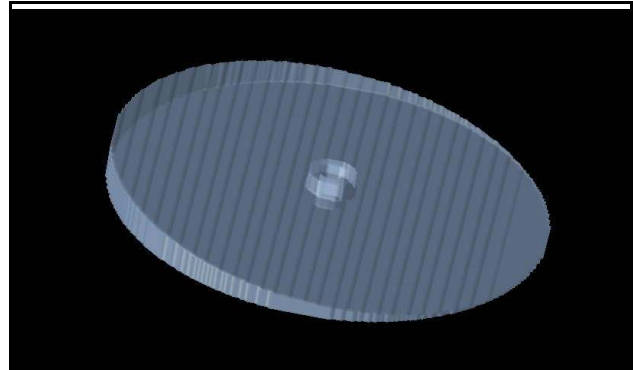
Figure 2.10. Rendering of the wedge-shaped glass that is used for rotational scanning. Changes in thickness as the disk rotates results in a change in focal length of the microscope objective.

scans through the sample. The rising edge of the glass wedge is color coded with black tape around the DC motor and checked with a photoreflective sensor so that the firmware can recognize when to begin scanning. Data is transmitted through a serial connection when the falling edge appears over the objective. This is to ensure that the scanning process is as quick as possible.

Preliminary tests with the glass wedge show that it does indeed change the focal length through the sample. Combined with the long-working distance objective, the glass wedge design should able to accommodate an entire scan in the axial direction at a precision at or below the resolution of the system.

2.6 Future Design

Future designs of the confocal scanner need to account for full-speed, video-rate acquisitions. As mentioned before, the current scan speed of the device is about 10-15 seconds per scan. If a three-dimensional scan was to be taken with 100 B-mode scans of 100 A-mode scans each, with 10 second scan time, it would take approximately 27.7 hours to complete the scan. With the glass wedge rotational scanner (assuming 2 seconds per scan), the same three-dimensional scan would take approximately 5.5 hours.

In order to speed up this process, a broadband source would need to replace the monochromatic laser as the illumination source. If an objective contained no correction for chromatic aberrations, the focal length would be determined by the wavelength of light. A spectrometer would be used as the detector in order to examine all wavelengths of light at once, resulting in an instantaneous axial scan. Axial precision would be based upon the accuracy of the spectrometer. Essentially, green light would have a different focal point than infrared light, completely eliminating the need of mechanical scanning. This method of using chromatic light

as a means of axial scanning has been accomplished in previous research groups[7,27,55].

CHAPTER 3

A FULLY AUTOMATED APPROACH TO QUANTITATIVELY DETERMINE THICKNESS OF TISSUE-ENGINEERED CELL SHEETS

3.1 Abstract

Sheet-based tissue engineering is an innovative field that has provided the scientific community with new tissue-engineered products such as skin, cornea, heart valves, and vascular grafts. As this area of tissue engineering progresses towards clinical implementation, quality control becomes more and more important. Imaging methods advertise themselves because of their high resolution and good tissue-fluid contrast. We present and compare two methods, one based on a custom-designed automatized large-area confocal scanner that uses backscattered light for image formation, and one based on optical coherence tomography (OCT). In both modalities, additional image processing is used to extract sheet thickness and density information and to create a quantitative tissue thickness map in a fully

automated fashion. In test objects (glass of known thickness and scattering samples) and engineered tissue sheets with artificially introduced defects we found high agreement between the two methods in the measurement of thickness and the visual representation of the defects. Both the OCT and the confocal scanner were able to provide high-detail images visually consistent to those obtained with brightfield microscopy. Both OCT and large-area confocal scanning in combination with specialized image processing algorithms promise to provide information on tissue homogeneity, density, and the presence of potential defects in tissue sheets in an unsupervised fashion and thus help establish new quality control methods in sheet-based tissue engineering.

3.2 Introduction

Rapid progress in tissue engineering technologies promises to deliver safe and biologically compatible replacement organs[25,28]. A new branch of tissue engineering technology has emerged, sheet-based tissue engineering[87]. Sheet-based tissue engineering uses thin cell layers as intermediate or final step, allowing flexible design of replacement parts such as cornea[42,86], heart valves[49,76], myocardial tissue[46,68], or arterial grafts[40,41]. As sheet-based tissue engineering progresses towards clinical studies and clinical application, there exists a need for a reliable method of quality control for tissue-engineered constructs. The primary goal of any quality control method is to accurately measure the thickness and density of the grown tissue sheets, and to monitor growth during the entire

47

manufacturing process. A secondary goal is the automation of the scanning process and the integration into the routine tissue manufacturing process. It is possible to use conventional or confocal microscopy to determine the upper and lower focal plane of the tissue sheet, but this manual process is highly time-consuming and prone to error as the transition from the in-focus region to the out-of-focus region occurs in a shallow gradient, thus making it difficult to precisely determine the tissue boundary.

Optical coherence tomography (OCT) is in the process of becoming a very popular imaging method particularly in the fields of dermatology and ophthalmology (see e.g. [23,31,53,60,83] for reviews). The reason is both its high resolution with pixel sizes in the order of 10μm or smaller, combined with very high fluid-tissue contrast. OCT penetration depth is on the order of few millimeters[26], but sufficient for the application in tissue sheets. OCT devices have recently become available as off-the-shelf units at a reasonable price. Clearly, a commercial general-purpose OCT device would have to be integrated with a positioning device to allow automated scans. Furthermore, a typical axial pixel size of 10μm would lead to a 10% discretization error in standard 100μm thick tissue sheets. Although a broader bandwidth light source would improve axial OCT resolution, a substantial increase in cost is associated with such an improvement. As an alternative, we have pursued the development of an inverted reflectance/scattering confocal scanner with an automated scanning mechanism to scan a variety of tissue flasks (up to T-225 flasks) and multi-well plates. Integrated unsupervised image analysis lends the device the capability to provide thickness maps, i.e., tissue thickness as a function

of the location inside the flask. The goal of this study is to examine the performance of the large-area confocal scanner and compare it to OCT as the gold-standard.

3.3 MATERIALS AND METHODS

3.3.1 Definitions

In the context of the characterization of the imaging devices, terms relating to the resolution of the devices are defined as follows. The <u>axial optical resolution</u> is theoretically set by the coherence length of the source in an OCT system, and by the focusing optics in a confocal system. The <u>lateral optical resolution</u> is theoretically set by the focusing optics in both OCT and confocal systems. The <u>axial pixel size</u> is set by the source and detector parameters in the spectral-domain OCT system, and the positioning stage in the confocal system. The <u>lateral pixel size</u> is set by the lateral positioning or scanning systems in both OCT and confocal systems. The <u>full-width at half-maximum</u> (FWHM) of an intensity peak is the measured intensity spread in the scan of a thin source (such as a mirror or an air-glass interface). As opposed to the definitions of resolution and pixel size, the FWHM is not an instrument parameter, but rather a measured quantity. The <u>point-spread function</u> is the intensity distribution near a peak when a thin interface (glass surface or mirror) was scanned, and it is characterized by its FWHM.

3.3.2 Confocal Scanner

The large-area confocal scanner was based on the design presented in Chapter 2, with the objective described in Section 2.2.3 and the fiber optics in 2.4.1. The setup can be seen in Figure on page . A 10mW, 635nm diode laser (Coherent, Santa Clara, CA) was used as the illumination source and coupled into one of the input ports of the fiber optic coupler. Digitized scan data was collected and further processed on a PC.

To provide a single axial scan (A-mode scan), the Z motor raised the positioning stage with the attached optics towards the sample, resulting in a change of focal plane as seen in Figure. Light scattered from the sample back into the fiber was directed onto the PMT through the fiberoptic coupler. The signal obtained by the PMT was processed through a 10-bit analog to digital converter, and was displayed as the scattered intensity as a function of z distance. With its X-Y positioning unit, the device had the ability to provide a B-mode scan (multiple A-mode scans along a straight line) as well as a complete 3D volume scan. Data from such a scan was provided as reflected/scattered intensity as a function of x,y, and z, symbolized with $I(x,y,z)$.

3.3.3 Optical Coherence Tomography

The OCT device used in this study was a Thorlabs OCT930SR spectral radar OCT with Handheld Probe and a broadband laser diode with a center wavelength of 930nm and 100nm FWHM of the bandwidth. Its nominal axial pixel size was 3.1μm per pixel, and the axial resolution 6.2μm according to the data sheet. The

scan head was mounted on a manual X-Y-Z translation stage (Thorlabs). The T-225 flask with the sample and the 6-well plate were held in place above the scan head with the same holder that was used for the confocal scanner. Unless mentioned otherwise, ten OCT scans of the same location were taken and averaged to improve the signal-to-noise ratio (SNR).

3.3.4 Scan Processing

In order to determine the thickness of a tissue sheet, images acquired from the confocal scanner and the OCT device were processed was used as follows. With a second-order Butterworth lowpass filter (cut-off frequency was set to a spatial frequency of 10, corresponding to 50µm) applied to each A-mode scan, the detector noise was greatly reduced and the tissue peak intensity isolated. The average and minimum scan intensities (I_{AV} and I_{MIN}, respectively) per individual A-mode scan were determined. A segmentation threshold T was computed from I_{AV} and I_{MIN} following Equation 3.1,

$$T = I_{AV} + (1 + a) \cdot (I_{AV} - I_{MIN}) \tag{3.1}$$

where a was an adjustable parameter generally set to 50%. In other words, tissue intensity was defined as any intensity that was by 50% higher than the scan average. Tissue thickness was determined by tracing from the highest tissue intensity peak towards background in both scan directions until the intensity dropped below the threshold. By using this segmentation method, the three-dimensional

51

intensity image I(x,y,z) was reduced to a two-dimensional thickness image T(x,y). For the confocal scans, a value of 37μm was subtracted from each pixel of T(x,y), because 37μm was an empirical value determined as the contribution of the reflectance peak from the adjacent flask bottom. Finally, the resulting thickness was scaled by the refractive index of the media of interest, which in this case was 1.37.

3.4.5 Performance Testing

The imaging performance of the confocal scanner was determined and compared to the OCT device in four different ways. First, the FWHM of the device was determined by scanning a mirror. Second, a reflecting phantom was created by placing a microscope cover slip (Fisher Scientific) in a T-225 flask. The cover slip thickness was measured with a caliper and determined to be 0.16±0.01mm. Twenty confocal scans were taken of the same point on the coverslip with axial measurements recorded every four steps of the encoder (0.652μm in air). These scans were averaged and displayed as a single scan to increase the signal-to-noise ratio (SNR). The thickness was determined using the method mentioned above with 1.47 as the refractive index of the media of interest (glass). Using the OCT device, ten B-mode scans consisting of 2000 A-mode scans each were taken of a 2mm strip of the coverslip and averaged. One arbitrary A-mode scan out of the B-mode image provided by the OCT device was compared to the confocal scanner in order to determine thickness of the coverslip. Third, six scattering phantoms were created by placing a small amount of silicone glue (DAP, Baltimore, MD) between two microscope slides. The slides were kept apart by six different shim spacers (Artus

Corporation, Englewood, NJ) and the final silicone layer thickness was determined with a micrometer caliper to be 0.196, 0.268, 0.326, 0.395, 0.616, and 0.703 mm, respectively. Silicone is a scattering material with a scattering coefficient of $\mu_s=5.3$ cm^{-1} and an refractive index of 1.40, both values related to those of tissue-engineered sheets. Specifically, silicone scattering was sufficiently high to generate a consistent scattering signal in both imaging devices. Ten confocal A-mode scans were acquired and averaged per sample, then the scattering region was segmented and its thickness determined. Similarly, OCT scans were performed by mounting the samples on a X-Y-Z translation stage to manually position them relative to the OCT scan head which was, in turn, mounted on a fixed post. Samples were manually adjusted to avoid aliasing with mirror images that are typically caused by the Fourier-domain image formation method of the OCT. Single B-mode scans were taken. In each B-mode scan, five A-mode scanlines were arbitrarily selected, thickness was determined from the scattering region and averaged for each slide. Fourth, a section of a tissue-engineered sheet as described in the next paragraph was scanned and repositioned ten times to determine the repeatability of the thickness measurement obtained by the segmentation algorithm. In addition, the sensitivity of the segmentation algorithm towards variation of the parameter *a* was determined.

Sample tissue sheets, grown in a 6-well plate, were provided for scanning by Cytograft Tissue Engineering (Novato, CA). During transportation, mold had developed in one plate. The tissue sheets were therefore fixated in 2% paraformaldehyde upon arrival, but both unaffected tissue and tissue affected by

mold were used for scanning. Intact tissue was used to determine the sensitivity and reproducibility of the segmentation algorithm. Tissue affected by mold was used to investigate the difference between normal tissue and mold - representing a highly abnormal feature - in the B-mode images. The confocal scanner was used to obtain a B-mode scan along a line of 4.76mm length spanning a section of mold and the adjacent tissue. The B-mode scan consisted of 1500 individual A-mode scans with a lateral pixel size of 3.175µm and axial points recorded every three steps of the encoder (corresponding to an axial pixel size of 0.489µm in air). A similar scan was taken by the OCT device of a 2mm strip spanning a section of mold and the adjacent tissue. This B-mode scan consisted of 1000 individual A-mode scans with an axial pixel size of 3.1µm.

To further simulate tissue defects, we mechanically disturbed the tissue in an adjacent well in order to provide additional artifacts for scanning and comparison. One hole was created in the tissue with a scalpel blade, which in turn scratched the plastic well. An additional hole was made with a 100µL pipette tip, which resulted in a cleaner puncture. A thin layer of tissue was scratched with a fine scalpel blade, and finally a felt tip pen was used to place a dark mark on the bottom for orientation. The area containing the defects was scanned by both devices. A rectangular section measuring 6.5 x 10.4mm encompassing all four defects was scanned with a lateral scan distance of 95.3µm in both directions by the confocal scanner with axial pixel size of 326nm. The same region was scanned with a lateral pixel size of 2µm by using the OCT device with an axial pixel size of 3.1µm. OCT B-mode scans were repeated with a 50µm offset by manually repositioning the OCT scanhead,

resulting in a highly anisotropic voxel size. The number of points in the horizontal

direction was then scaled by ten using linear interpolation to obtain voxels with close

to isotropic dimensions.

Finally, the tissue region containing the most prominent defect was also

photographed using a conventional inverted microscope for comparison, and one

additional high-resolution confocal scan was taken over the same defect: a square

region of size 635 x 635µm was scanned with a lateral pixel size of 3.175µm by the

confocal scanner with axial pixel size of 326nm. This region was also compared

visually to the microscope image.

3.4 RESULTS

Verification of the device performance following the four verification steps

described in the Methods section provided information on the confocal scanner

performance as follows. The scan of the mirror provided a sharp and clearly

identifiable peak, and full-width at half-maximum (FWHM) of the A-mode scan was

determined to be 45 pixels, which corresponds to 22.0µm in air. A similar scan with

the OCT device provided a FWHM of 6.2µm. The microscope cover slip placed

inside of a T-225 flask was scanned with both devices. The A-mode intensity profile

of the confocal scan is shown in Figure 3.1a. Each intensity peak was caused by

reflection at the interface of two media of different refractive index. FWHM values

of 21.51µm for peak A and 24.45µm for peak B were determined. The pixel-based,

uncorrected, peak-to-peak distance was 109.04µm. However, since the focal plane

is traveling through media with a refractive index other than air, this value needs to be scaled up by the refractive index of glass (n = 1.47) in order to compensate for the decrease of the focal plane movement in the media. This yields the corrected thickness value to be 160.3μm, very closely corresponding to the caliper measurement of the coverslip thickness, 0.16±0.01mm. The corresponding A-mode scan of the OCT device is shown in Figure 3.1b with an axial pixel size of 3.1μm. Peak A has a FWHM of 6.2μm while the FWHM of peak B is 18.6μm. Distance measurements in the OCT device are corrected by a function built into the proprietary software and yielded a thickness of 170.8μm after the refractive index value of n=1.47 was entered. By scanning over the edge of the coverslip, we were able to determine that the lateral optical resolution was smaller than the lateral pixel size in both devices.
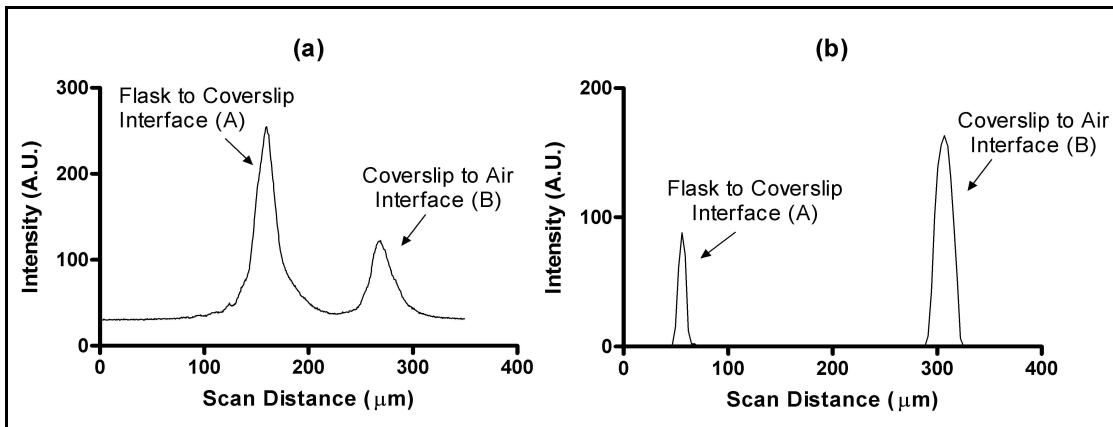
Figure 3.1. A-mode scans of a test phantom (a 0.16 mm microscope glass coverslip inside of a T225 flask). Shown is the region where the flask-coverslip interface and the coverslip-air interface create high-intensity peaks through reflection. (a) Confocal scan with values recorded every 3 encoder steps (489nm). (b) OCT scan with axial pixel values recorded every 3.1μm.

Figure 3.2 shows an A-mode scan of a grown tissue sheet inside a six-well plate. The confocal scanner was used with an axial pixel size of 326nm. Peak A is caused by reflection at the interface between the air and the bottom of the well and has a FWHM of 26.1µm. The reflection of the second interface between the well and the media causes a lower peak (peak B)

Figure 3.2. A-mode scan from the confocal scanner showing raw scan data (solid line) as well as the filtered data as used in the segmentation step to determine tissue thickness (dashed line).

with FWHM of approximately 13.4µm. The tissue itself appears as a much broader peak in Figure 3.2. The width of this peak reflects the tissue layer thickness. The dashed line in Figure 3.2 represents the scan after the application of software filtering in preparation for segmentation and thickness computation. After tissue segmentation and application of corrections for refractive index, actual tissue thickness was determined to be 109µm.

The ability of the segmentation algorithm to accurately and precisely determine tissue thickness was further examined. Six scattering samples of silicone were scanned with both devices. Their thickness, determined from the images, were compared to caliper measurements (Figure 3.3). Both confocal and OCT measurements yielded a thickness that was about 10% larger than the caliper-based thickness (the slope of both regression lines was 1.1 with a correlation coefficient R^2 larger than 0.999). The deviation between both optical methods was very small,

less than 1% in average. To assess the precision, a tissue sheet was scanned ten times with the sheet being repositioned between scans. The average value of all thickness measurements was determined to be 263μm with a standard deviation of ±7.1μm. Finally, the same tissue section was used to determine the sensitivity of the segmentation process towards the threshold parameter *a* in Equation 3.1. Over a wide range of *a* from 10% to 100%, a thickness decrease of 1 pixel per percent point was found. However, at the extreme values, a higher sensitivity than average was observed, and close to our reference value of *a*=50%, thickness decreased with only 0.5 pixels for each percent point.
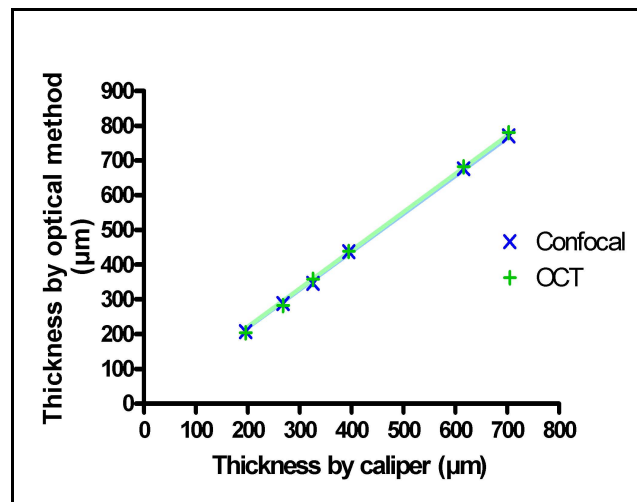
Figure 3.3. Result of the measurement of the thickness of scattering samples (silicone) with a conventional caliper and optical methods. A systematic deviation between caliper and optical measurements can be seen (regression slope of 1.1 with $R^2 > 0.999$ for both OCT and confocal with the caliper measurements), but OCT and confocal measurements deviate less than 1% from each other in average.

In Figure 3.4, the confocal scanner's ability to generate B-mode scans is demonstrated. To obtain a B-mode scan, multiple A-mode scans were arrayed to form an image of scattered intensity along a line in X direction and axial depth, I(x,z). Figure 3.4 shows the B-mode scan obtained from a section of the tissue sheet in which mold was allowed to accumulate. Two parts of this image are further broken down. The mold-free tissue on the left side of the
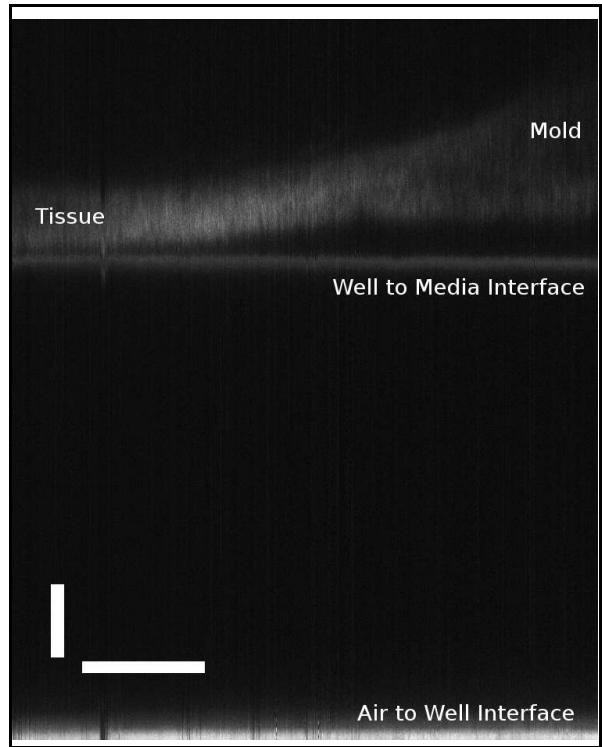
Figure 3.4. Confocal B-mode scan of a tissue sheet with mold using the confocal device. Horizontal scale bar is 1mm, and the vertical scale bar is 100µm.

image was found to be 124µm thick using the segmentation algorithm previously described. Two methods were used to calculate the thickness of the mold-grown tissue on the rightmost side of the image. Using the segmentation algorithm, the thickness of the tissue with the mold together was calculated to be approximately 215µm. On closer inspection, it can be seen that the segmentation algorithm failed to provide the correct thickness because of the scattering properties and the porosity of the mold. Manual measurement yielded mold thickness of up to 349µm. This value is further confounded by the unknown refractive index of mold. A similar B-mode scan was taken with the OCT device and shown in Figure 3.5. This image also shows a tissue layer with the mold growing on the right hand side. From this

image, it could be determined that the thickness of the mold-free tissue was 155.1μm, in close relationship to the tissue thickness obtained by the confocal scanner. The thickness of the mold on the thickest point was around 212μm. This was determined by using 1.37 as the refractive index of the tissue, and assuming 1.34 as the refractive index of the mold due to its lower density.
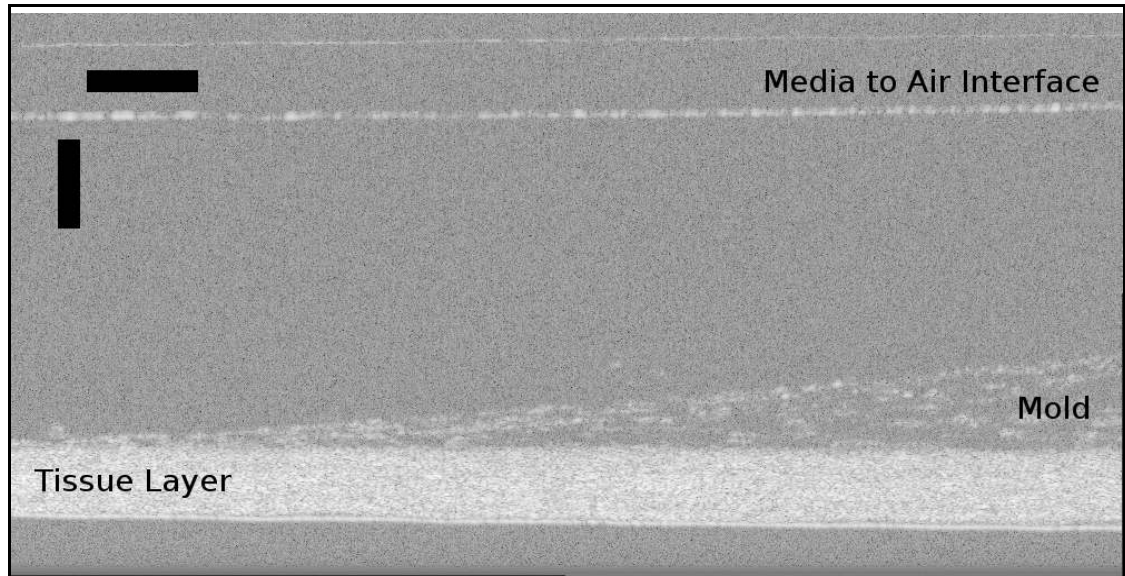
Figure 3.5. B-mode scan of a tissue sheet with mold using the OCT device. Horizontal scale bar is 200μm, and the vertical scale bar is 250μm.

The segmentation algorithm for the confocal scanner can be used on multiple B-mode scans to create a thickness map of large tissue sheets. Figure 3.6 shows the mechanically disturbed section of tissue sheet imaged over an area of approximately 68mm^2. Figure 3.6a is a thickness map obtained over the entire area using the segmentation algorithm. Thicker areas appear brighter in the map, with a maximum value in this case computed to be 189μm. Most of the tissue in this area appears to be approximately 100μm thick. For comparison, the thickness map of the same area is shown in Figure 3.6b taken by the OCT device.
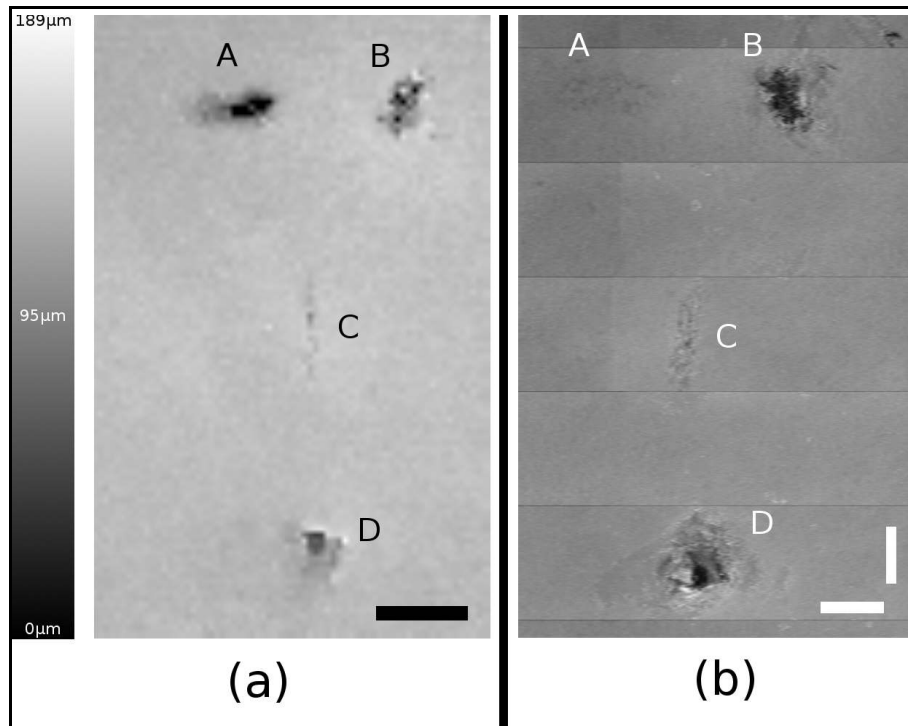
Figure 3.6. Side by side comparison of both modalities showing mechanically disturbed tissue. In both images, "A" is an external mark on the bottom of the well created by a fiber-tip pen. Hole "B" and slice "C" were created with a tip of a scalpel. Hole "D" was created with a 100µL pipette tip. (a) Confocal thickness map with calibrated intensity values (black: zero thickness to white: 189µm). Scale bar is 1.5mm. (b) Scaled thickness map of the same area scanned by OCT. Horizontal and vertical scale bars are each 1mm.

A close-up of the scan taken of the punched hole (feature D in Figure 3.6) is shown in Figure 3.7 covering a total area of 0.403mm^2. A microscope image was taken of this same hole for comparison and shown in Figure 3.8. It can be seen that the darkest areas in Figure 3.7 coincide with the area where the pipette tip completely penetrated the tissue (no cells visible in Figure 3.8). The surrounding tissue appears to be approximately 100µm in thickness. Large thickness variation exists within this small area of tissue, most likely due to the manipulation of the tissue when pressed down by the pipette tip.
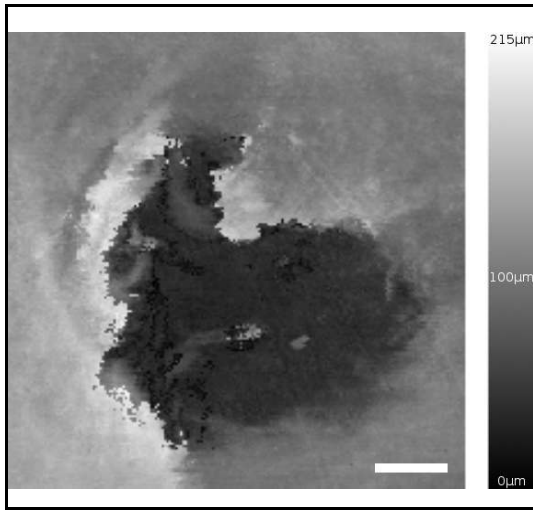
Figure 3.7. Confocal thickness map created by a high-resolution scan of area D in Figure 3.6. Scale bar is 100µm.
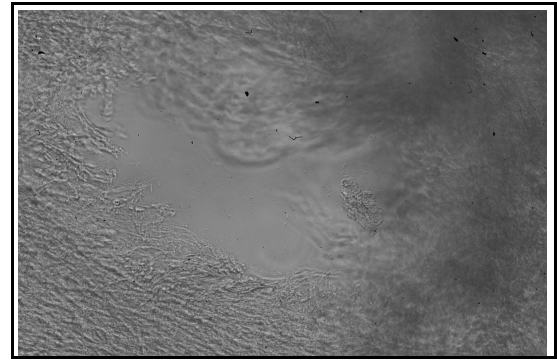
Figure 3.8. Conventional brightfield microscope image of the area scanned in Figure 3.7. The image was taken on an inverted microscope and mirrored along the Y-axis for comparison to the confocal thickness map.

3.5 DISCUSSION

In this study, we presented an automated method to determine thickness and density of large tissue sheets based on a confocal scanner and an OCT scanner. In both imaging modalities, the signal is generated by refractive index changes, either by large-scale changes at interfaces or by subresolution changes commonly called scattering. Absorption can also cause contrast. In tissue, light is primarily scattered by collagen, and scattered light intensity may turn out to be related to collagen matrix expression of the cells. Experiments performed with the confocal scanner match observations found in Monte Carlo simulations[18]. It can be seen that peaks caused by changes in refractive index are exhibited as sharper peaks, while peaks resulting from scattering regions appear broader. At interfaces,

reflected intensity depends on the degree of refractive index change. Consequently, peak B is lower than Peak A in Figure 3.2, since the change in refractive index from the well to the tissue is only about 0.1, while the change from the air to the well is 0.47. When examining the measured FWHM of the imaging device, it becomes evident in Figures 3.1 and 3.2 that the FWHM of the peaks are broader than those obtained with OCT. The source of image blur is different in both instruments. Since axial pixel size of the OCT device is 3.1µm, it is difficult to accurately determine a more accurate FWHM of the peaks. For example, in Figure 3.1b, the FWHM of peak A appears to be 6.2µm, although the true FWHM may lie anywhere between 6.2µm and 18.6 µm due to limitations of pixel discretization of the device and partial-volume effects. In addition, the FWHM of peak B which was determined to be 18.6µm, a value closer to that of the confocal scanner of 24.45µm. Clearly, the predominant factor that limits resolution in the confocal scanner is Gaussian blur, while the limiting factor in the spectral radar OCT device is the source bandwidth and the optical path difference between sample and reference beams.

Following confocal theory,[14] the 3 dB separation distance of two focal planes, d_z **(3dB)**, is related to the refractive index *n*, the pinhole size *a*, the wavelength λ, and the objective magnification *M* through Equation 3.2:

$$d_Z(3dB) \ = \ \frac{7.4 \cdot n \cdot a^2}{\lambda \cdot M^2} \qquad\qquad (3.2)$$

Applying Equation 3.2 to our system, we found d_z to be 0.73μm from which the standard deviation σ of the Gaussian point-spread function can be calculated as 0.87μm. From this value, a theoretical FWHM of 2.1μm follows, a value markedly lower than the FWHM of the peaks found in Figure 3.2 (26.1μm for peak A and 13.4μm for peak B). For the OCT, the axial optical resolution is defined as

$$\Delta z \ = \ \frac{2 \ln 2}{\pi \, n} \cdot \frac{\lambda^2}{\Delta \lambda} \tag{3.3}$$

where Δz is the theoretical FWHM of the Gaussian point-spread function and $\Delta \lambda$ is the FWHM of the bandwidth of the superluminescent laser diode. For our OCT system, Δz=3.8μm based on technical specifications, although the mirror scan yielded a FWHM of 6.2μm. Clearly, the main factor that limits the usability of the confocal scanner is the Gaussian blur introduced by several factors: the 50μm pinhole aperture that is dictated by the multimode fiber used in our prototype, possible underfilling of the objective, and our use of an objective that provided a long working distance at the expense of numerical aperture. A setup based on a very small single-mode fiber has been accomplished by a different research group,[32] and design of future prototypes will take this concept into account, since a smaller pinhole should greatly improve the axial resolution. In a similar fashion, multiple factors play a role in determining the point-spread function of the OCT. In addition to the bandwidth of the light source (Equation 3.3) , the point-spread function depends on the optical path difference between reference and sample path, and

similar to the confocal scanner, the point-spread function that was actually measured was broader than expected from theory. Since a smaller FWHM of the point-spread function may be expected from theory, we cannot exclude the influence of manufacturing tolerances.

One additional possible solution to reduce the width of the point-spread function would be software deconvolution. If tissue thickness is the main parameter of interest, the empirical adjustment of the segmentation threshold would provide accurate thickness values. This notion is further corroborated by the comparable accuracy and precision of the thickness measurements in the OCT and confocal scanners. In the case of the confocal scanner, an excellent match with OCT-based thickness was observed in spite of the poorer point-spread function. However, both devices show a systematic deviation from caliper measurements in silicone samples of known thickness (Figure 3.3). We assume that the pressure exerted on the silicone samples by a micrometer-type caliper may compress the samples and cause this type of deviation - more compression in thicker samples. This consideration raises the question of precision. Clearly, mechanical measurements cannot provide precise measurements of sheet thickness, even if sample contamination is not taken into account. An experiment with repeated thickness measurement of tissue thickness after sample repositioning provided a standard deviation of 7.1µm in a 260µm sample, corresponding to a coefficient of variation of 2.7%. Considering the point-spread function of the confocal scanner, precision is not a major factor that influences the usability of the confocal scanner. Precision is also determined by the thresholding algorithm, particularly by the arbitrarily

chosen factor *a* in Equation 3.1. Clearly, any Gaussian blur, whether caused by the optical system or by image processing, reduces the measured thickness with increasing *a*. While we consider a change of apparent tissue thickness of 0.5 pixels per percent-point change of a (this corresponds to roughly 3μm thickness change - about 1.2% of the thickness of a 260μm sheet - when *a* is changed from 50% to 60% to be sufficiently reliable, two avenues can be tried to further reduce this potential source of error. First, *a* can be calibrated using samples of known thickness, such as the silicone sheets. Second, other edge-detection methods can be experimented with, such as application of the LoG (Laplacian-of-Gauss) operator. However, since the main limiting factor of the confocal scanner is the axial optical resolution, the improvement of the optical system should remain the primary focus.

While the thickness measurement by the automated segmentation algorithm can be considered reliable for normal tissue layers, the measured thickness of disturbed tissue or non-tissue features (such as mold) is uncertain. Some of the segmentation parameters have been empirically chosen and warrant a more thorough analysis with a larger sample set. Modifications of the segmentation algorithm would not change the principle of the actual confocal scanner. Both the coverslip thickness and the tissue thickness match the expected values and the values determined with OCT within few percent. Major deviations in the thickness measurements were observed in the mold scans. This is most likely due to the lack of differentiation of the mold and tissue caused by the filter step in the segmentation process. However, we included the mold scans for illustration purposes, as any mold accumulated on the tissue would invalidate the practical application of the

tissue anyway. Therefore, determining the true thickness of the mold is irrelevant in this context.

A side by side comparison of the mechanically disturbed tissue images shown in Figure 3.6 illustrates the usefulness of the thickness map. It can be seen in the confocal image (Figure 3.6a) that there are thickness variations over the surface area of the tissue sheet. The thickness map generated by the confocal scanner is calibrated linearly over the thickness scale. Thickness variations are also visible in the OCT image (Figure 3.6b) but cannot easily be quantified because the OCT image was acquired with several scans, and the scans assembled manually to form the image in Figure 3.6b. Consequently, background intensity variations become visible that would adversely affect the estimated homogeneity of the tissue thickness. The source of these variations in a closed-source off-the-shelf OCT system remains unclear, and the observed intensity variations prohibit us from making a reliable comparison about thickness differences over the large scale. However, these considerations are limited to the specific OCT device that was used in this study. It is not unusual that details of the data collection and image formation software of off-the-shelf devices are not known, often being considered as trade secrets. A custom-built device, comparable to our custom confocal scanner, would not have any of these limitations, and a similar degree of automation would be possible. This notion can be taken further by custom-designing the optics at the end of the OCT sample arm. In fact, a more suitable sample scanning lens can be used to improve the lateral resolution of the device, as improving the bandwidth of the source would improve the axial resolution. However, the depth of focus is inversely

related to the lateral resolution, and the limiting factor is the thickness of the flask bottom.

The ability of the confocal scanner to provide a wide range of lateral pixel sizes is illustrated further in Figure 3.7 which was taken at approximately 30 times higher resolution in each direction that Figure 3.6a. Such a scan would take 100 times longer over the same area than the low-resolution scan. On the other hand, the high-resolution scan compares well to the microscope brightfield image (Figure 3.8), where similarities in the hole shape can clearly be seen. The time factor could give rise to two scan modes: One initial scan at a low resolution, followed by high-resolution spot scans wherever thickness variations or other potential defects have been identified by software. Further software image processing is possible. One example is illustrated in Figure 3.9. A threshold of 125 μm has been applied, creating dark areas wherever tissue thickness falls below 125μm. This could be useful in quality control to determine where large areas of
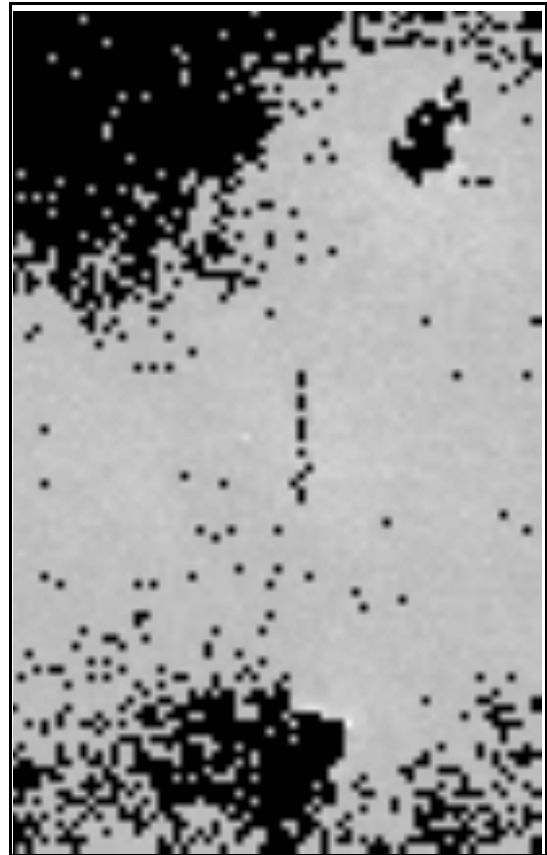
Figure 3.9. Confocal image showing mechanically disturbed tissue with thresholding at 125μm. Black regions indicate tissue sections with a thickness below 125 μm. This processed image is provided to demonstrate the ability of the confocal scanner to automatically identify inhomogeneous or thin tissue regions.

68

the tissue have not reached matured thickness. Similarly, the analysis of thickness variation could reveal inhomogeneously grown sheets.

A comparison of the OCT and confocal scanners reveals advantages and disadvantages in both systems. Compared to OCT, a higher signal-to-noise ratio was observed in single (non-averaged) scans. Voxel size was smaller in the confocal scanner, leading to a potentially higher spatial resolution. In this specific case, confocal spatial resolution was primarily confounded by the large FWHM. Furthermore, the OCT scanner was dramatically faster than the confocal scanner. The z-stage used in the confocal scanner prototype allowed us to perform one A-mode scan in 9 seconds, while the OCT scanner provided one B-mode scan in 0.25 seconds. Acquisition and averaging of ten OCT B-mode scans for improved SNR was still faster than one confocal A-mode scan. Clearly, the two most important areas for improvement of the confocal scanner are the axial translation mechanism (faster fine-positioning in the axial direction by using, for example, a piezoelectric positioner) and the fiberoptic system, where an optimum pinhole size needs to be found.

In conclusion, we found that both OCT and confocal scattered-light imaging in combination with suitable image processing are viable methods to determine the thickness of tissue-engineered sheets. Our experience with the off-the-shelf OCT device showed us that a custom design allows for more complete system integration and full automation. This study also demonstrated that a confocal scattered-light scanner is feasible, but additional improvements are required to convert our prototype into a device that can be used in routine quality control for engineered

tissue sheets. In sheets that are typical for this application, that is, sheets between 100µm and 300µm thickness, both the OCT and the confocal principle can be used. Provided that the FWHM of the confocal scanner can be improved, its smaller voxel size makes confocal imaging more suitable than OCT for thin tissue sheets, while thicker sheets cannot be imaged with the confocal scanner. Both imaging techniques, in combination with suitable image processing, promise to become useful enabling technologies for automated quality control in tissue engineering.

CHAPTER 4

MEASURING SCATTERING EFFECTS WITH SINGLE-MODE

FIBER-OPTIC CONFOCAL MICROSCOPY

4.1 Abstract

Confocal microscopy has become an option for examining tissues *in vivo* as a diagnostic tool for skin. However, low penetration depth of confocal microscopy presents the need to recognize contrast at shallow depths in order to accurately image the skin. Since collagen is the primary scattering element in skin, it would be useful to quantify the relative concentration of collagen present. For this reason, we built a fully automated confocal scanner to examine how light scatters in Intralipid, a common tissue phantom, and three-dimensional collagen gels. By measuring light attenuation at interface reflections of various thicknesses using our device, we were able to extract the scattering coefficient of Intralipid at increasing concentrations in water. We were also able to measure the amount of scattering of various concentrations of collagen in gels directly using backscattered light. The results show a direct linear increase in backscattering for a positive change in density of collagen within the gels.

4.2 Introduction

Confocal microscopy is beginning to establish itself as a method of examining tissues *in vivo* as a diagnostic tool for the human cornea [44,51] and for skin [45,52]. In utilizing confocal microscopy as a reliable method of diagnostic imaging, it is important to be able to evaluate the potential of the confocal system in terms of the ability to recognize scattering and refractive index changes as sources of contrast. This needs to be done at shallow imaging depths due to low penetration depth limits of the system. Penetration depth has been examined in confocal microscopy in previous studies[34,69] and is largely governed by confocal pinhole size and absorption in the system. Confocal microscopy has also been shown as a method of determining scattering coefficient [12,13], which is something we will examine in this study.

In this chapter, we use a customized confocal system to look at scattering in Intralipid and in collagen gels. Intralipid is a common phantom with similar optical properties as that of biological tissues[17,48]. The properties of Intralipid have been thoroughly studied, providing us with a reliable method for comparison[24,75]. With our device, we will attempt to estimate the scattering coefficient at various concentrations of Intralipid by measuring reflection at various depths from refractive index mismatches.

Collagen is a major source of scattering in skin[3], and therefore is a main source of contrast in imaging. It is beneficial to quantify these scattering properties in order to use them for diagnostic purposes, such as imaging the extracellular

matrix in skin. In order to accomplish this, we will directly measure backscattering from collagen gels. Collagen gels are typically used as *in vitro* systems used to model cell behavior in three-dimensions[19-21,62]. Using these gels, we can determine how directly backscattered light correlates with increasing densities of collagen.

4.3 Materials and Methods

Our scanner was developed based upon to the principle of single-pinhole confocal microscopy and was built according to the specifications set forth in Chapter 2, specifically with the improvements of the objective described in Section 2.4.2 and with the single-mode fiber optic coupler in Section 2.4.3. For the first part of this study, 20% Intralipid (Sigma Aldrich) was diluted to concentrations of 0.5%, 1.0%, 1.5%, and 2.0%. Small volumes of each Intralipid concentration were placed between two glass slides separated by shim spacers of known thicknesses of 127, 191, 254, 318, 381, and 508μm,
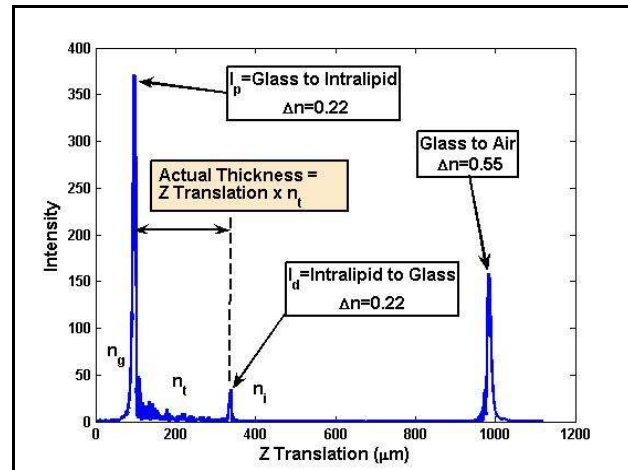
Figure 4.1. A-mode scan of Intralipid. The intensity of the resulting peak from the refractive index change from Intralipid to Glass is recorded. Actual thickness is determined by scaling the Intralipid peaks by the refractive index of Intralipid.

creating 24 total samples. The volumes were held in place on the slides due to surface tension. A B-mode scan of lateral pixel size 3.175μm consisting of 5 A-mode scans of axial pixel size 326nm (as seen in Figure 4.1) was taken for each sample. Each set of A-mode scans was aligned so that the refractive index change from glass to Intralipid was aligned at the left of the image. The 5 A-mode scans were averaged together for analysis.

In order to ensure that our signal would not be overly attenuated at these imaging depths, we computed the maximum depth that we would be able to resolve a 0.22 refractive index change using Beer's Law. Beer's Law equation was modified so that the primary attenuation factor is scattering coefficient μ_s instead of absorption coefficient, since absorption in Intralipid at 660nm is approximately 0.002cm^{-1}[24]. The modified equation is given by

$$I = I_0 e^{-\mu_s t} \tag{4.1}$$

where I is the intensity of light after distance t from incident light I_0. Since we are concerned with reflected signals at refractive index mismatches, we use the following equation describing specular reflected light

$$\frac{I_{ref}}{I_0} = \left(\frac{n_1 - n_2}{n_1 + n_2} \right)^2 \tag{4.2}$$

74

in which I_{ref} is the intensity of the reflected light and n_1 and n_2 are the refractive indices of the two mediums at the interface. After mathematical manipulation of these two equations for multilayer analysis, we can predict the maximum imaging depth t_{PD} as a function of scattering coefficient and refractive indices of each medium. This yields the following equation

$$t_{PD} = \frac{-\ln\left[\dfrac{I_d\left(\dfrac{n_t-n_g}{n_t+n_g}\right)^2}{I_p\left[1-\left(\dfrac{n_g-n_t}{n_g+n_t}\right)^2\right]^2\left(\dfrac{n_t-n_i}{n_t+n_i}\right)^2}\right]}{2\mu_s} \tag{4.3}$$

where the limits of detection are given as ratio I_d/I_p (ratio of 2nd interface peak to the peak from container to media), and the refractive indices are given as n_t for the scattering media, n_g for the initial container, and n_i for the detecting interface. These values are referred to in Figure 4.1.

In our calculations, we define maximum imaging depth at the point where I_d is 2% of I_p, chosen so that the
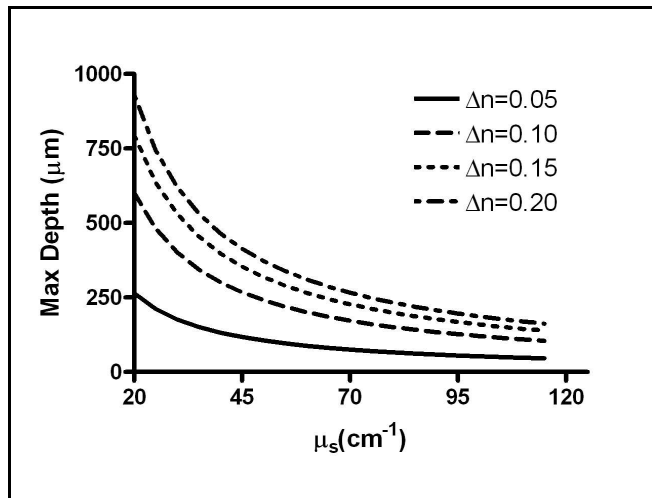
Figure 4.2. Theoretical maximum imaging depth due to scattering coefficient. The maximum depth to detect refractive index changes of 0.05, 0.10, 0.15, and 0.20 are shown.

75

intensity would be sufficiently above baseline to be recognized as a peak. We varied scattering coefficient of the media at fixed refractive index change (n_t to n_i) to determine maximum imaging depth, with the results shown in Figure 4.2.

From Figure 4.2, we can see that as long as scattering coefficient is below 70cm^{-1}, we can easily resolve a refractive index change of 0.20 at thicknesses below 250µm, with deeper depths available for more diluted concentrations. This validates our choice of shim stock for the Intralipid experiments. It is important to note that while a reflection signal can be attained at such high imaging depths, the resolution decreases heavily at higher thicknesses due to specimen-induced spherical aberration[4].

For the second part of the study, we used collagen gels in order to determined the effect of collagen scattering directly, rather than through refractive index changes. Gels were fabricated using high concentration Type 1 (8.00mg/mL) rat tail collagen (BD Biosciences, Bedford, MA). Twenty-one concentrations were made ranging from 0.30mg/mL to 3.30mg/mL at 0.15mg/mL intervals. Volumes for each desired concentration were mixed into test tubes (Fisher Scientific) which were kept on ice. 10% of the desired original volume consisted of 10X phosphate buffer solution. Volume of collagen was determined as the ratio of the product of desired original volume of solution and final desired concentration to the concentration of the stock volume, but not added yet. 1N NaOH (2.3µL per 100µL collagen) was added to the test tube. Enough cold 18MΩ-cm ultrapure water was added to the test tube to bring the solution to the desired original volume. The solution was further diluted with the addition of 333µL cell culture media per 1mL original volume and mixed

before the addition of the collagen, bringing our total volume to 1.333mL. A 500µL aliquot of each concentration was pipetted twice into 24-well plates (Becton Dickinson Labware, Franklin Lakes, NJ) and allowed to gel for 1 hour at 37°C. A B-mode scan of lateral pixel size 3.175µm consisting of 30 A-mode scans of axial pixel size 652nm was taken for each sample. As in the penetration depth study, each set of A-mode scans was aligned so that the refractive index change from well to gel was at the left of the image. The 30 A-mode scans were averaged together. The scattering signal obtained from 196 to 522µm after the peak was averaged again in order to determine a single-quantity scattering signal. The lower bound was chosen for analysis in order to avoid specular reflection from the well to gel interface while the upper bound was chosen in order to ensure sufficient signal prior to losses due to penetration depth.

4.4 Results

The natural logarithm (from Beer's Law, Equation 4.1) of the intensity of the peak measurements for the Intralipid-glass interface were recorded for each concentration and plotted against thickness of the tissue phantom as shown in Figure 4.3. Tissue phantom thickness was
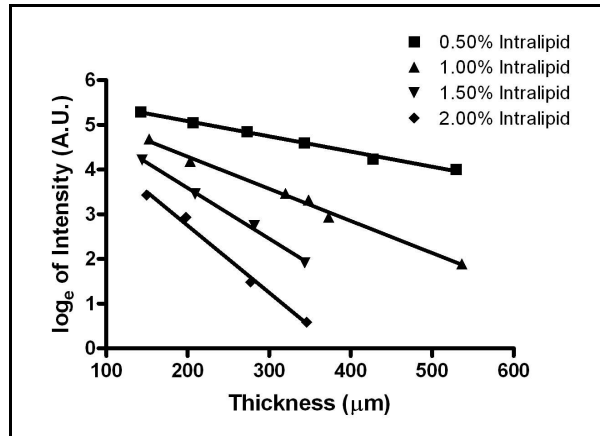
Figure 4.3. Natural logarithm of the intensity signal from a 0.22 refractive index change (Intralipid to air) at various thicknesses at four concentrations. Each concentration was fit to a linear regression to obtain the decay constants.

determined by scaling the peak-to-peak distance from z actuator translation by approximate index of refraction of the phantoms (assumed to be 1.33) as shown in Figure 4.1. The natural logarithm of the data where sufficient signal was above baseline was gathered and fit to a linear regression, with the decay constants recorded. All six thicknesses recorded reflection peaks sufficiently above baseline for the 0.5% and 1.0% Intralipid concentrations, with decay constants of $0.003405\mu m^{-1}$ and $0.007189\mu m^{-1}$ respectively. Scattering coefficient limited the penetration depth of the confocal system in the 1.5% and 2.0% Intralipid concentrations, with usable peaks for the first four thicknesses up to 318μm. Regression of these concentrations yielded decay constants of $0.01133\mu m^{-1}$ and $0.01502\mu m^{-1}$ respectively. R^2 goodness of fit values were all greater than 0.99 for each concentration. All linear regressions had a significant non-zero slope.

The decay constants obtained from the regression were used in order to extract scattering coefficient of the various concentrations of Intralipid. Since absorption in Intralipid and water is low, we can assume that the prominent decay factor in these regressions is scattering coefficient μ_s. After considering the round-trip
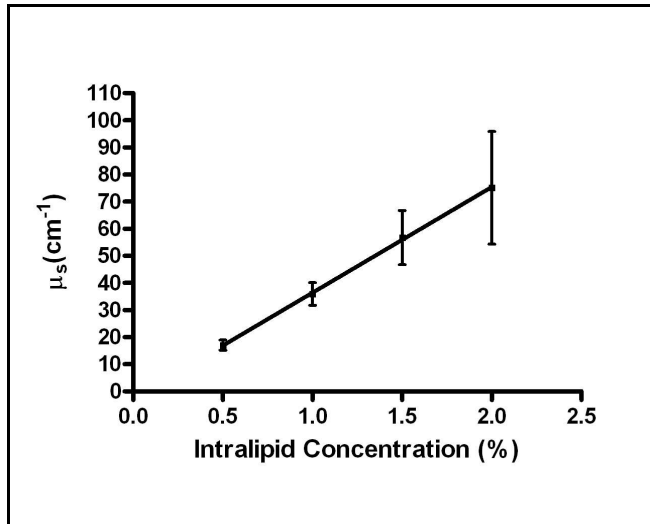
Figure 4.4. Extracted scattering coefficient from the decay constants in Figure 4.3. Error bars denote 95% confidence of the decay constants. This was fit to a linear regression in order to extrapolate additional concentrations.

attenuation for the Beer's Law function, we assume μ_s to be equal to 17.025cm^{-1} for

0.5% Intralipid, 35.945cm^{-1} for 1.0%, 56.65cm^{-1} for 1.5%, and 75.1cm^{-1} for 2.0%.

The values for μ_s were plotted against Intralipid concentration in Figure 4.4. Linear

regression of the data yielded a slope of 38.99 ± 0.5904 with a Y intercept of -2.553

± 0.8084cm^{-1}. R^2 goodness of fit value was approximately 1.0 with P-value 0.0002,

showing a significant non-zero slope.

Referring back to Equation 4.3, we can now model the maximum imaging

depth as a function of refractive index change at the fixed scattering coefficients

obtained from Figure 4.3 in order to validate our peak detections recorded in Figure

4.3. This model is shown in Figure 4.5.
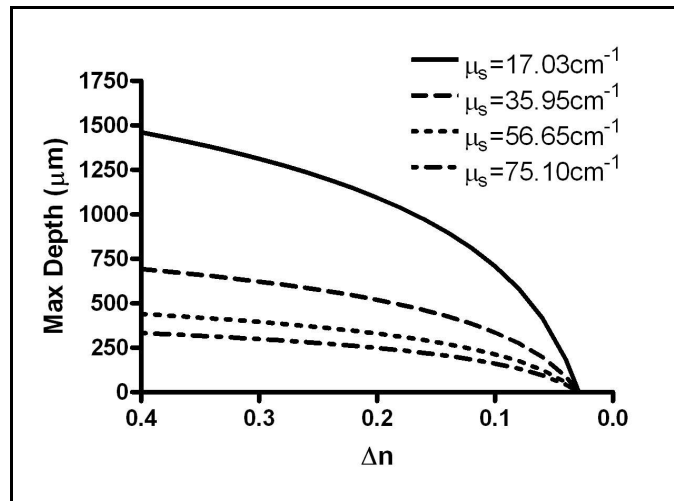
Figure 4.5. Theoretical penetration depth in order to identify a specific refractive index change at the four scattering coefficients shown in Figure 4.4.
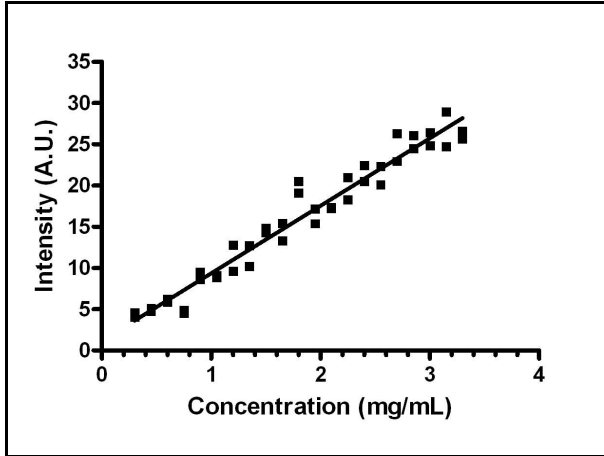
Figure 4.6. Quantified backscattering from increasing concentrations of collagen gels.

In the case of collagen gel scattering, the averaged scattering signal from each of the 42 samples was plotted against the collagen gel concentration with the results shown in Figure 4.6. Linear regression of the data points yielded a slope of 8.173 ± 0.2819 with a Y intercept of 1.184 ± 0.5685, in arbitrary units of intensity. R^2 goodness of fit value was 0.95 with P-value of less than 0.0001, showing a significant non-zero slope. Analysis of residuals show a random normal distribution of mean approximately zero and standard deviation of 0.0141. Pearson Product Moment correlation is 2.183×10^{-9} with p-value 1.0, therefore showing no correlation of residuals and indicating our model was appropriate in defining collagen scattering.
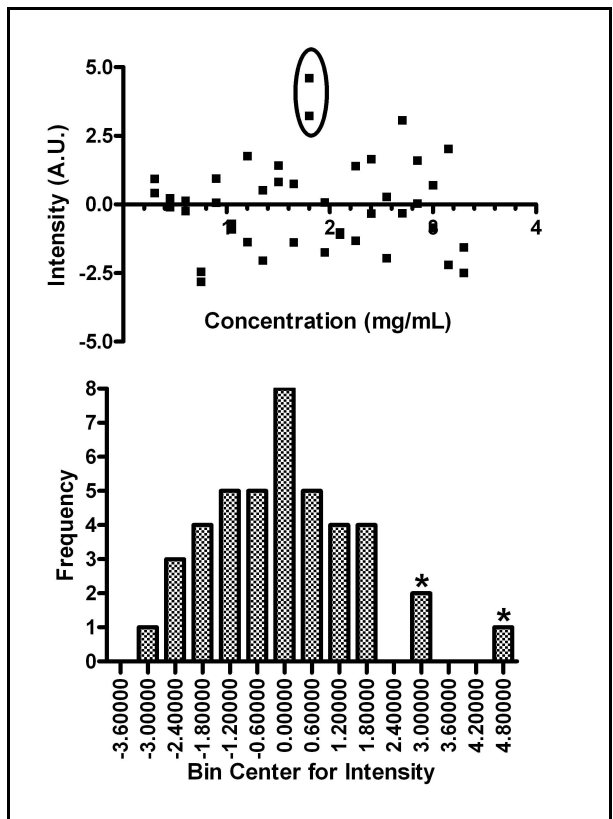
Figure 4.7. Residual analysis of Figure 4.6. Concentration of 1.8mg/mL is circled with values denoted as asterisks on the histogram.

4.5 Discussion

In this study we determined the scattering coefficient of Intralipid for various concentrations based on the amount of light reflected from a 0.22 index of refraction change at different thicknesses. From Figure 4.5 we can verify that our obtained peaks fall within the maximum imaging depths for each shim stock, concluding that these peaks were due to the expected interface rather than an unknown artifact or noise. The exponential regressions of the Intralipid signals resulting from a 0.22 refractive index change were consistent with Beer's Law. By using the regression in Figure 4.3, extracting the scattering coefficient for plotting against Intralipid concentration, our linear scale in Figure 4.4 can be used to predict scattering at higher concentrations. For our case, a prediction at 10% Intralipid for example would be $390cm^{-1}$ at 660nm. This value falls between the values measured by Flock[24]and van Staveren[75].

Direct backscattering of the collagen gels rises as concentration of collagen within the gels are increasing. Since this is due to an increase in scattering coefficient, this function is assumed to be linear, which the statistical analysis supports. It is worth noting that in the residual analysis, both repeats of collagen gel concentration 1.8mg/mL are viewed as minor outliers (Figure 4.7). While it is possible that this is a naturally occurring phenomenon, it is more likely due to a small error in pipetting.

In conclusion, we showed that our confocal scanner can be used to investigate the scattering properties of turbid media. The use of Intralipid

demonstrates our ability to measure reflection within low scattering medium in order to extract optical properties when absorption coefficient is negligible, providing typical confocal resolution is not needed at high imaging depths. The optical sectioning capability of the single-mode fiber provides the necessary penetration to accomplish this task. The recognition of increased scattering from higher density collagen gels provides supportive evidence that this device can be used to analyze collagen density in terms of contrast for *in vivo* applications.

CHAPTER 5

MEASURING DERMAL SCATTERING USING A PROTOTYPE

CONFOCAL SCANNER

5.1 Abstract

There are many products on the market claiming to restore collagen in skin in order to reduce visible wrinkles for the user to appear more youthful. However, evaluation of these products is subjective with a "before and after" effect. Since side-to-side comparisons and dermatological grading scales make no attempt to determine the restructuring of the extracellular matrix, we used the customized scanner based on confocal microscopy in order to examine underlying collagen structure. Since the extracellular matrix changes with age, we attempted to locate a trend due to incident light backscattering from the collagen. We also evaluated the effects of gender and skin type on collagen backscattering on 150 healthy volunteers. Results show that while a significant effect was observed with age, it is contrary to our hypothesis that backscattering should decrease with age due to losses of collagen. This is most likely due to the high variability of subsamples, which we address. Nevertheless, the results indicate that with a few changes to the system to ensure direct measurement of the collagen, a stronger trend may be observed comparable to that seen in nature.

5.2 Introduction

The anti-aging industry is flourishing with many new products claiming to restore collagen in photoaged skin, reducing wrinkles and improving elasticity. While there is much research in establishing the claims of such products[29,36,63,82], the methods of doing so are largely subjective, normally involving side-to-side comparisons or through dermatological grading scales. These methods do not view the collagen structure directly, but rather determine the effectiveness of the product based upon visual inspection. An objective method of quantifying how the skin benefits from these products would be highly desirable in substantiating the products' claims.

Confocal microscopy is one method that could serve as a diagnostic tool for human skin [45,52]. Confocal microscopy in terms of diagnostic imaging, relies upon scattering and refractive index changes as sources of contrast. Collagen has been shown to be a major source of scattering in skin[3], and therefore can be analyzed using confocal microscopy. As we showed in Chapter 4, higher concentrations of collagen results in an increase of scattering coefficient of the underlying tissue, and can be detected.

In this study, we will attempt to use our customized confocal scanner in order to identify a trend among healthy volunteers of all ages through measurement of the skin on the finger. Skin can essentially be described in three general layers: the epidermis, dermis, and subcutaneous tissue. The epidermis is the outermost layer, and consists of five layers itself, the topmost being the stratum corneum, which is

the permeability barrier of the skin[30]. The epidermis contains specialized cells that produce melanin (melanocyte) and are involved in immune response (Langerhans cell)[50]. In the epidermal layer, melanin is the primary optical absorber. The dermis contains collagen fibers, which provide tensile strength and anchors the epidermis[84]. Subcutaneous tissue consists of mostly fat and connective tissue. While age related changes of skin have been identified through various methods before[56,59], we will focus primarily on light scattering through the skin specifically due to collagen. We will quantify the amount of backscattering due to collagen based on parameters of age, gender, and skin type. A correlation would provide information as to the feasibility of utilizing our confocal scanner as an objective diagnostic tool for the effectiveness of anti-aging medications.

5.3 Materials and Methods

Our confocal scanner is shown in Figure 5.1, with the setup described in Chapter 2. The optical fiber is described in section 2.4.1, and the objective is described in 2.4.2. The 7.5mW, 660nm laser diode fiber pigtail mentioned in 2.4.3 was attached to one of the input ports of the
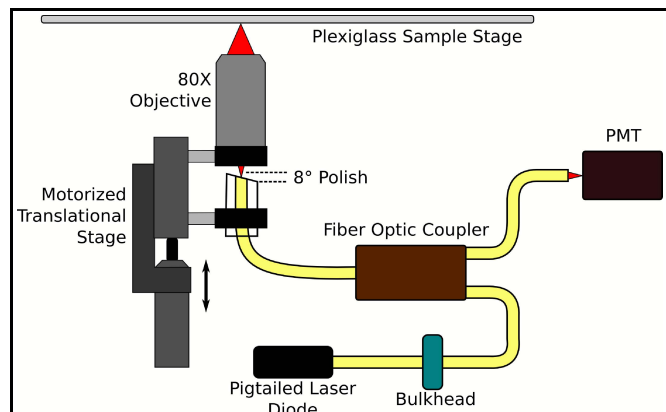
Figure 5.1. Schematic of confocal scanner. Light from the pigtailed laser diode travels through the fiber and exits to the 80X objective. The fiber termination acts as a confocal pinhole providing a depth response. Backscattered light is collected by the PMT.

fiber optic coupler with a makeshift bulkhead. The output port of the fiber was cleaved and secured inside an acrylic holder, and polished at an 8 degree angle in order to avoid specular reflection at the fiber-air interface.

The use of human subjects for this study was approved by the University of Missouri Health Sciences Institutional Review Board. 150 healthy volunteers ranging in ages from four months to 79 years (demographics shown in Table 5.1) had the middle pad of the middle finger on their right hand scanned after supplying informed written consent. This area was chosen in order to minimize jitter from the subjects as well as to minimize pigmentation variation. Gender and Fitzpatrick skin type were also used as

Figure 5.2. Sample scanning setup. The middle finger rests between two microscope slides (dashed box) above a coverslip. Both the slides and the coverslip are secured to a plexiglass stage with a hole above the microscope objective.

identifiers. The finger was placed between to microscope slides that formed a channel and acted as spacers. Below the finger was a coverslip to serve as a possible reference between scans. This setup is shown in Figure 5.2. The specular reflection from the coverslip would theoretically remain consistent from subject to subject. When possible, 10-A mode scans was taken in order to ensure sufficient sub-sampling and to average jitter. Each scan had an axial pixel size of 489nm.

Table 5.1 Demographic data of healthy volunteers.

Age of Subject (years)		Gender	Fitzpatrick Skin Type	
<10	7		**1**	13
10-20	14	111 **Female**	**2**	62
20-30	29		**3**	60
30-40	21		**4**	4
40-50	28		**5**	9
50-60	25	39 **Male**	**6**	2
60-70	17		**Total** 150	
>70	9			

Backscattered light from each subject showed up as a single peak. The intensity above background for the peak was recorded along with the full-width at half-maximum (FWHM). Also, an intensity value approximately 167μm past the peak was recorded in order to ensure that scattering was recorded in the dermal layer of skin. A
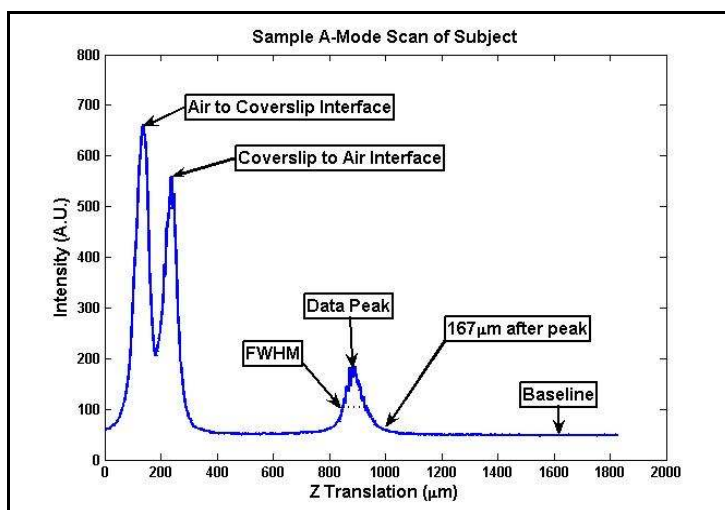
Figure 5.3. Sample A-mode scan of a subject. The two sharp peaks on the left denote the coverslip used as a reference. Data from the subject is the third peak in the center.

sample A-mode scan highlighting each measurement is shown in Figure 5.3.

5.4 Results

Analysis of data used the following regression model employing subsamples among the group of samples

$$y_{ijkl} = \mu + age_i + skin_j + gender_k + skin^*gender_{jk} + e_{ijk} + d_{ijkl}$$
$$i = 1,2,...,150 \; ; \;\; j = 1,2,...,6 \; ; \;\; k = 1,2 \; ; \;\; l = 1,2,...,10$$

$$(5.1)$$

where μ is the overall mean, **age**, **skin**, and **gender** are the fixed effects of the ith, jth, and kth factors, respectively, **skin*gender** is the interaction between fixed effects $skin$ and $gender$, **e** is a random error, and **d** is the random effect due to the lth subsample. For each subject, ten measurements were taken in order to obtain a more accurate response for each subject by reducing the variability. Our model contains an extra random effect term which accounts for the variability due to the subsamples. The model in Equation 5.1, assumes that e_{ijk} and d_{ijkl} are normally and independently distributed with means zero and respective variances σ_e^2 and σ_d^2. Using this formulation, F-tests can be developed in order to test our four null hypotheses: no factor differences do to age, gender, or skin type, and no interaction between gender and skin type. Kuehl presents a comprehensive discussion on this topic[39]. In the context of this chapter, the factors for **age** is the age in years of the subject, the factors for **gender** are male and female, and the factors for **skin** are the categorical assignments of the Fitzpatrick Skin Type. A significance level of 0.05 is assigned for all data sets. Results from the raw data set are shown in Table 5.2.

Table 5.2 P-values from our analysis using all skin types. Values that are statistically significant are italicized. When the interaction is significant, the other fixed effects become irrelevant.

Fixed Effects	Data Peak	167μm past Peak	FWHM
Age	*0.0349*	0.2869	0.6237
Gender	0.4611	~~0.0069~~	0.3366
Fitzpatrick Skin Type	0.8123	~~0.0860~~	0.8677
Gender/Skin Type Interaction	0.3081	*0.0485*	0.0739

When the dependent variable was the overall peak above baseline, the fixed effect of age was significant with a p-value of 0.0349, while the fixed effects of gender and skin type were not significant with p-values of 0.4611 and 0.8123, respectively. Furthermore, there was no significant interaction between gender and skin type. From Figure 5.4 it can be seen
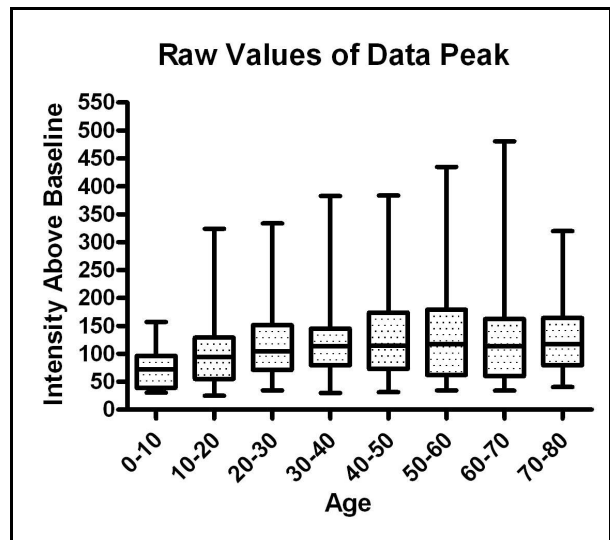
Figure 5.4. Overall data peak as dependent variable. The box plot shows a positive trend in the medians of each sample group.

that while there is much variability among the measurements, there is an indication of a positive trend among the medians for each sample.

Using the intensity of the light obtained 167μm past the overall peak as a dependent variable, the interaction between gender and skin type became

significant, with a p-value of 0.0485. With the interaction term significant, the fixed effects of gender and skin type is irrelevant. The fixed effect of age was not significant, with a p-value of 0.2869.

Full-width at half-maximum as the data peak when used as a dependent variable showed no significant effects among age, gender, and skin type. These effects had p-values of 0.6237, 0.3366, and 0.8677, respectively. As in the case using the overall peak, there was no significant interaction between gender and skin type. A box plot of this data can be seen in Figure 5.5.
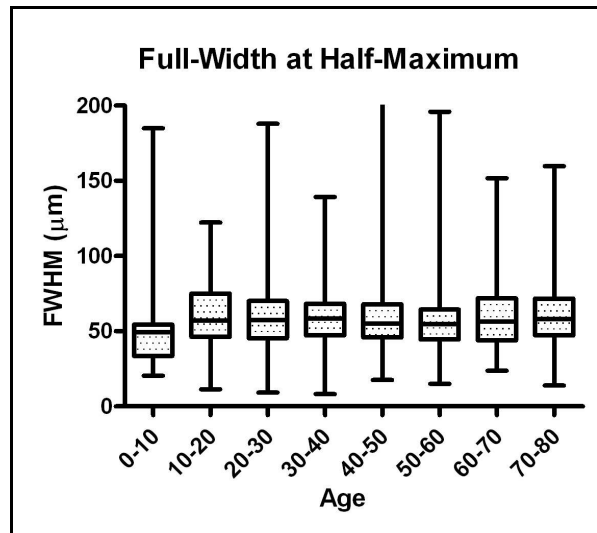
Figure 5.5. FWHM as a dependent variable. As expected, this was not determined to be affected by age.

The model was run again using skin type from 1 to 5 instead of from 1 to 6. This is because there were no males with skin type 6 that participated in the study. The results of this test is shown in Table 5.3.

As in the model using all skin types, when the dependent variable is overall peak above baseline, the fixed effect of age is significant. When the dependent variable is 167μm past the overall peak, interaction between gender and skin type is significant. These trends can be seen in the box plots in Figure 5.6. All other treatments are not statistically significant.

90

Table 5.3 P-values from our analysis using skin types 1-5. Values that are statistically significant are italicized.

Fixed Effects	Data Peak	167μm past Peak	FWHM
Age	*0.0353*	0.2862	0.6248
Gender	0.4621	~~0.0068~~	0.3383
Fitzpatrick Skin Type	0.8042	~~0.0496~~	0.7647
Gender/Skin Type Interaction	0.3103	*0.0480*	0.0754
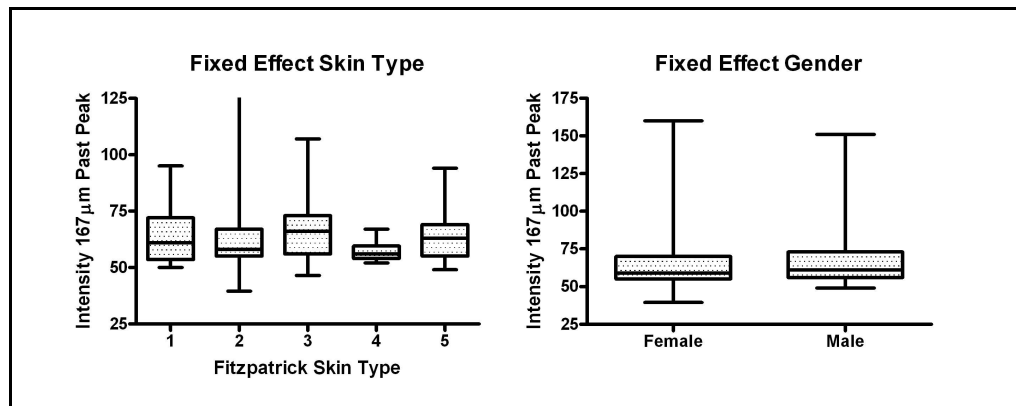
Figure 5.6. 167μm past data peak as dependent variable. There is a slight positive trend in the medians the subjects in response to darker skin. There also appears to be a gender effect.

The previous two tests were run again using a different data set. This time, the baseline obtained from the specular reflection at the coverslip-to-air interface was used to normalize all data for the dependent variables overall peak above baseline, and 167μm past the peak. With the test including all Skin Type data, no significant fixed effects were observed when the dependent variable was 167μm past the peak. However, with dependent variable overall peak above baseline, age

had a significant effect, p-value of 0.0056, the trend of which is shown in Figure 5.7.

All other effects were not significant. When gender and skin type fixed effects were

removed, age still had a significant effect with p-value of 0.0205. All p-values for

this test is shown in Table 5.4.

Table 5.4 P-values from our analysis using all skin types after normalization by baseline specular reflection. Values that are statistically significant are italicized.

Fixed Effects	Data Peak	167μm past Peak
Age	*0.0056*	0.3705
Gender	0.8833	0.9895
Fitzpatrick Skin Type	0.7117	0.9481
Gender/Skin Type Interaction	0.7077	0.7532

Rerunning the second test in which we omitted skin type 6 using the normalized values, no significant effects were observed for dependent variable of 167μm past peak. As with before, when the dependent variable was the overall peak above background, age was significant with p-value of 0.0057. All other effects were not significant. When age was run alone as a fixed effect, it was still significant with a p-value of 0.0247. These results can be seen in Table 5.5.
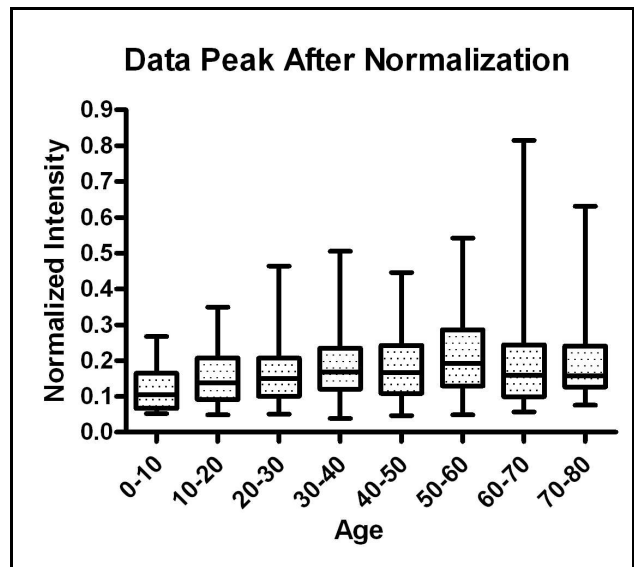
Figure 5.7. Normalized intensity of data peak above baseline as dependent variable. There is a positive trend in the medians of each sample group.

Table 5.5 P-values from our analysis using skin types 1-5 after normalization by baseline specular reflection. Values that are statistically significant are italicized.

Fixed Effects	Data Peak	167μm past Peak
Age	*0.0056*	0.3705
Gender	0.8833	0.9895
Fitzpatrick Skin Type	0.7117	0.9481
Gender/Skin Type Interaction	0.7077	0.7532

5.5 Discussion

It should first be noted that while plots of residuals show a moderate departure from normality, the t-statistics and F-statistics are still known to be robust[43]. The analysis of our collected data implies that there is an effect of age on scattering in skin. However, the data we obtained does not necessarily support our original hypothesis that there is a negative effect from age due to skin scattering, as seen by the trend described by Figures 5.4 and 5.7. It is possible that a few of the outliers affects the trend of the data.

The trend for the intensity recorded 167μm after the peak shows a positive trend as the skin of the individual darkens, as seen in Figure 5.6. This is surprising due to the fact that melanin is a primary absorber in the epidermis, as one would expect to see a negative trend due to the round-trip attenuation of the incident light.

From Figure 5.6 it would also seem that the intensity recorded from males is higher than that of females from this measurement. It is unlikely that the effects are due to a difference in epidermal thickness, since there is much debate on gender

being significant variable[70]. It may be possible that the use of hand creams and lotions attenuate the signal due to their effects on the epidermis. Since women have a tendency to use hand creams and lotions more than men, this could explain some of the interaction that we see in Figure 5.6.

The use of full-width at half-maximum as a dependent variable was in purpose to provide a general idea on penetration through the skin. It can be seen in Figure 5.5 that as expected, this was not dependent upon age of the individual.

Although this study did not support our original hypothesis, the results that were statistically significant illustrate the need for future study. One issue that would readily need to be addressed is the amount of jitter of the subjects. It can be seen from Figures 5.4 and 5.5 that a high variability of subsamples exist. In the case of overall peak as a dependent variable, the standard deviation of the means of all samples is 57.9. The average of the standard deviations for each sample is 43.2. This jitter is most likely caused due to the amount of time it takes for a single scan (approximately 10 seconds). Minor fluctuations in the position of the finger can cause an increase in specular reflection, throwing off the data peak. One method of decreasing this scan time would be the use of chromatic confocal microscopy as a means of axial scanning[7,27,55] which uses a broadband light source combined with a non-achromatic objective for depth profiling. This technique is further explained in Section 2.6 of Chapter 2 and Section 6.3.2 of Chapter 6 in this dissertation.

It may also be necessary to calibrate laser output with a power meter between visits. This is because small changes in intensity of laser light can show

a significant effect on the results. However, our technique of using the specular reflection at the interface peak between the air and coverslip was effective in reducing this effect. As shown in Tables 5.4 and 5.5 the normalization had a major effect on these values, as the significant effects due to gender and skin type interaction are no longer present. The significant fixed effect of age still shows up after normalization as seen in Figure 5.7. The slope of the trend is extremely small, and it is possible that the outliers are affecting the direction of the trend as described earlier.

However, another possible explanation for the rising slope may have to do with the top most layer of skin, the stratum corneum. It is likely the intensity of the data peak is the specular reflection caused from the refractive index mismatch of air to skin. The refractive index of the stratum corneum is approximately 1.45[38] and is highly scattering. It is also known that as people age, dead skin cells slough off at a slower rate, thickening the stratum corneum[81]. It is possible that this slight increase in thickness of the stratum corneum results in high specular reflection and diffuse reflectance near the incident beam. This may be the cause of the increase in the total signal that is seen from the overall data peak with age.

In order to determine the feasibility of this explanation, Monte Carlo for Multi-Layered media (MCML) was used to model diffuse reflectance within a radius of 10µm of the incident light at the surface of skin. This was performed using the Monte Carlo code from Wang and Jacques[79,80]. A three layer skin model was used consisting of the stratum corneum, epidermis, and dermis. Bulk optical parameters for these layers were estimated from the consolidated work of Van

Gemert and Jacques[74] consisting of data from Anderson and Parrish[2], Wan *et al.*[78], and Everett *et al.*[22] It is important to note that Everett's data on the stratum corneum is only for ultraviolet light, so the bulk optical properties are extrapolated according to the trends found for the epidermis and dermis. A summary of the parameters used in the MCML program is given in Table 5.6.

Table 5.6 Optical parameters used in MCML.

Layer	n	μ_a(cm-1)	μ_s(cm-1)	g	thickness(μm)
Stratum Corneum	1.45	80	2000	0.9	10-28
Epidermis	1.4	40	500	0.8	80
Dermis	1.4	4	400	0.8	1900

One million incident photons were used in order to model the diffuse reflectance. It can be seen from Figure 5.8 that the diffuse reflectance within a ring of diameter 10μm appears to increase with thickness change of the stratum corneum. While it is necessary to note that modeling of skin using parallel planes is not ideal, and the estimations of the bulk properties do not necessarily follow what is seen in normal variations in nature, the results of
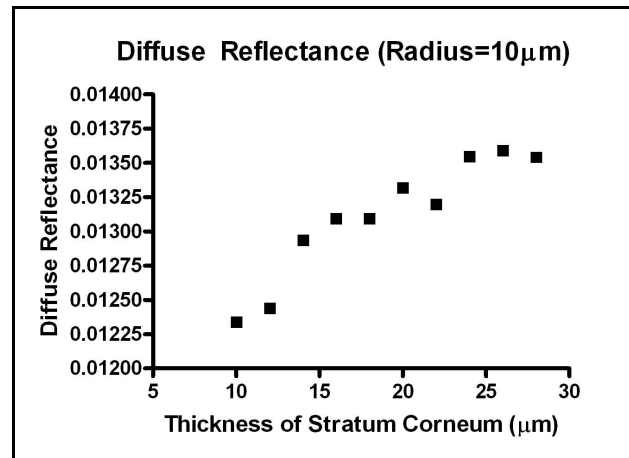
Figure 5.8. Measurement of diffuse reflectance using MCML varying the thickness of the stratum corneum.

the MCML analysis appear to support the explanation as why the fixed effect of age appears to be signifcant with the data peak.

While the data peak here may be significant due to thinkness changes in the stratum corneum, it interferes with the overall goal of looking at collagen in the extracellular matrix. In order to combat this, a drop of glycerol (refractive index of 1.47) could be placed between the coverslip and the sample. This would reduce the amount of specular reflection due to the interface between air and skin. With specular reflection reduced, contrast is effected by absorption and scattering coefficient. This would ensure that the information that we are seeing is related to collagen rather than the stratum corneum. An additional solution would involve using a wavelength in the near-infrared spectrum to provide greater penetration depth.

In conclusion, while the confocal device was able to measure backscattering from skin, it is unclear on whether or not we were able to obtain the signal directly from collagen. Although we are still confident that a trend of collagen backscattering based on age can still be found, it is necessary to make thorough improvements to the device itself before repeat measurements should be sought after. The primary goal is to reduce jitter among patients caused by the amount of time it takes to acquire ten scans. Using chromatic confocal microscopy, this is something that can be easily attained, as multiple scans can be taken in a matter of seconds. A more balanced data set should also be acquired, with special consideration given to the stratification of types of patients who visit the dermatology clinic. This study laid the

groundwork for a thorough repeat of this project, and it is recommended that

providing the aforementioned changes take place that this study should be repeated.

CHAPTER 6

CONCLUSIONS AND FUTURE OF PROJECT

This dissertation has introduced a fully-automated fiber-optic confocal scanner. Three uses have been presented along with the iterations of the prototype development. In Chapter 1, an introduction to the method of confocal microscopy was presented from the original patent application to the modern versions in use today. An overview of the mathematics involved with producing contrast was provided in order to explain the confocal mechanism. Chapter 2 described in detail the development of the confocal scanner from original free-space conceptions to the self-aligning fiber-optic device currently in use. A few methods of improvement were also offered and will be elaborated on at the end of this chapter. In Chapter 3 the ability of the confocal scanner to quantify thickness for tissue-engineered cell sheets was described. Our method was compared with a commercial spectral-radar optical coherence tomography device. Both methods demonstrated an ability to serve as quality control mechanisms for identifying thickness, density, and homogeneity in tissue-engineered constructs. Chapter 4 presented the confocal scanner as a method which can quantify scattering at shallow image depths. Using Intralipid, we showed that scattering coefficient could be identified through light attenuation before and after specular reflection. We then used the scanner in order to look at direct backscattering in the collagen gels. Finally, the ability of the confocal scanner to be

used in a clinical setting was examined in Chapter 5, as we attempted to quantify the aging of skin.

6.1 Benefits of the Confocal Scanner

This dissertation thoroughly elaborated on the abilities of our prototype confocal scanner. The automated xy-translation stage allows for the comprehensive scan of samples up to 225cm^2 (Chapter 2), which is particularly useful in the quantitative assessment of tissue-engineered cell sheets (Chapter 3). While many customized scanners use free space optics, the confocal scanner is alignment free with its use of fiber-optics (Chapter 2), which can be tailored for use in different applications, such as using a single-mode fiber for higher penetration depth (Chapter 4) or a larger fiber for maximizing the scattering signal (Chapter 5). The scanner is able to recognize defects in a sample as well as determine thickness (below 300μm) as well as a commercially available optical coherence tomography system (Chapter 3). The fully-automated functions also allow for complete three-dimensional scanning and the ability to generate two-dimensional maps in determining homogeneity in a sample (Chapters 2 and 3).

The applications of the confocal scanner are diverse as well, and have been discussed throughout this dissertation. In addition to showing the ability to be a tool for quality control (Chapter 3), the confocal scanner can also be a diagnostic device in a clinical setting (Chapter 5). The device can also be used to identify scattering as a source of contrast at low penetration depths (Chapter 4). The confocal scanner

was also shown to have the ability to estimate scattering coefficient in low absorbing media (Chapter 4). The system itself can be made portable (Chapters 2 and 5) and be modified for a multitude of other applications (Chapter 2).

6.2 Shortcomings of the Confocal Scanner

While the benefits of the confocal scanner are promising, there are also a few shortcomings that need to be remedied for continuation of this project. Depth resolution is limited by Gaussian blur introduced by a number of factors that include an oversized pinhole for the system, possible underfilling of the objective, and sacrifice of numerical aperture for working distance (Chapter 3). While a smaller pinhole remedies this, the system is introduced to Haidinger fringes, affecting contrast near a refractive index mismatch (Chapter 2). Use of an air-immersion objective leads to high-index mismatches in *in vivo* applications (Chapter 5). Scanning at high imaging depths also leads to specimen-induced spherical aberration, which decreases overall axial resolution (Chapter 4).

Perhaps the greatest shortcoming of the device is the lengthy scan times for signal acquisition. The slow mechanical scanning process can not only lead to overly excessive scan times in quality control (Chapter 3) but can also increase the likelihood of jitter from subjects in *in vivo* applications (Chapter 5). These scan times appear to be one of the primary limiting factors in the versatility of the confocal scanner.

6.3 Future Direction of Project

6.3.1 Overview

As mentioned throughout this dissertation, the ideal confocal scanner would be portable and versatile and could scan quickly with high resolution and repeatability. The full-width at half-maximum of the Gaussian blur needs to be minimized. This can be accomplished by using a single-mode fiber, which greatly improves the optical sectioning capability of the confocal system. Another method is to increase the numerical aperture of the objective. However, due to the current workings of the device, a long-working distance is needed in order to scan through the tissue. Typically, numerical aperture is sacrificed for this working distance, thus reducing the axial resolution of the confocal system.

The more pressing issue limiting the marketability of the current state of the confocal scanner is the lengthy scan times. Currently, scans are mechanical and typically take about ten to fifteen seconds per scan. The time costs of using this device are currently not greater than the benefits. While uses such as investigating localized areas of thickness in cell sheets or determining scattering coefficient for low absorbers are not dependent on these time costs, the idea of doing an exhaustive scan on an entire cell sheet is ridiculous considering the present shortcomings. For this reason, scan time needs to be readily addressed.

In order to account for all issues above, I recommend the following improvements in the confocal scanner.

6.3.2 Chromatic Confocal Microscopy

One of the employed methods of optical coherence tomography involves the use of a spectrometer to obtain frequency related depth information. The intensities of the different wavelengths detected by the spectrometer from illumination of the broadband source provides depth information that can be mathematically resolved. This information takes place on the millisecond time scale, resulting in extremely fast acquisition times. Normally this is coupled with a line scanning mirror, resulting in B-mode scans that are refreshed at video rate.

The idea of using a spectrometer in order to look at depth information of the sample can be easily applied to confocal microscopy. The primary changes involves the laser source, which can no longer be monochromatic,
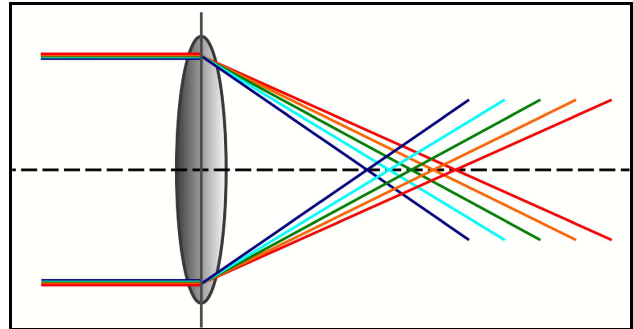
Figure 6.1. Chromatic aberration. The lens focuses different wavelengths at different points.

and the objective lens. Most objective lenses for confocal microscopy are apochromatic, which are corrected for spherical and chromatic aberration at multiple wavelengths. In order to use the spectrometer as a detector, the objective lens must have no correction for chromatic aberration. As shown in Figure 6.1, chromatic aberration results in a change of focal length for increasing wavelengths. When combined with a broadband light source, depth information can be gathered by recording the spectral information due to reflections and backscatterers at different focal lengths. Rather than mechanical translation of a single focal plane,

a non-achromatic objective would illuminate all focal planes at once, and can be recorded easily by the spectrometer[27,55], a process that is illustrated in Figure 6.2.
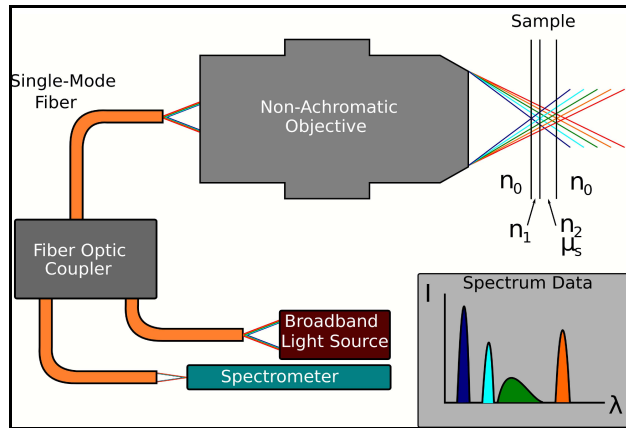
Figure 6.2. Schematic of chromatic confocal microscopy. The non-achromatic objective focuses the wavelengths at different points. The intensity of each wavelength is recorded by the spectrometer, supplying depth information.

The scan depth attainable by this system is largely due to the objective lens used in the application along with the wavelength. Since chromatic aberration is introduced from the wavelength-dependent refractive index of the lens, optimization of these two factors is application dependent. In methods where precision is needed, scan depth can be adjusted to 7µm[67], while in microtopography applications, this can be as high as 700µm[54].

6.3.3 Optimizing Axial Resolution

In order to provide for the maximum axial resolution, a single-mode fiber with center wavelength matching the center wavelength of the broadband light source

would be used (similar to OCT). This would not only allow for precise optical sectioning, but the small aperture would increase penetration depth as well. Furthermore, the long working distance can be sacrificed as mechanical scanning is no longer necessary. This leads to an increase in numerical aperture, and thus an increase in axial resolution. It would even be possible to vary the working distance of the objective for the application, as a long working distance would be more suitable in cases where cell sheets or samples are contained in thick containers, and small working distance may be more suitable for *in vivo* applications.

6.3.4 Physical Concerns

Physical concerns involving the use of chromatic confocal microscopy revolve primarily around the non-achromatic objective and the spectrometer. Axial pixel size is determined by these two parameters. For the objective, the amount of chromatic aberration plays a role in the precision. It would be necessary to find an objective that would shift the focal length by less than a micron per nanometer wavelength. The spectrometer resolution balances this. If the spectrometer can resolve less than nanometer scale for wavelength, the focal shift due to chromatic aberration can be longer per unit wavelength. Ideal sampling would be around 500nm in the axial direction, and these parameters need to be chosen carefully in order to achieve this.

On the reverse side, it is necessary to scan a long enough distance over the bandwidth of the incident light. Currently, the confocal scanner's translational stage allows for a scanning distance of well over a couple of millimeters, even though this kind of penetration is not likely. Nevertheless, it would be useful to be able to cover

the range of around 500µm in the case of low scattering media. For this reason, broadband illumination should be selected with a large enough bandwidth to cover this range. Essentially, a proper balance needs to be maintained among the incident light source, the non-achromatic objective, and the spectrometer in order to achieve maximum scan distance, and to meet Nyquist sampling. It should also be noted that since the detector would become a spectrometer rather than a PMT, corrections need to be made in order to account for SNR. Although, this can be achieve in adjusting the integration time of the spectrometer and by averaging the spectrum.

6.3.5 Software Concerns

In utilizing different wavelengths, corrections must be made to handle the variations due to sample parameters that are wavelength dependent. This includes index of refraction, absorption coefficient, scattering coefficient, and to some degree anisotropy. Since this will no doubt differ from sample to sample, these corrections are going to be specific towards the end use of the device. This eliminates some of the versatility that the device has with monochromatic light, as these parameters are the same throughout the sample. Combined with intensity attenuation due to depth, corrections for these factors could become extremely complex, particularly if there is a large bandwidth for the incident light.

In order to combat this, a mechanical scan may need to be taken in order to view the depth profile so each wavelength runs over the depth of the sample. This information may be used in order to perform the needed correction for exhaustive

106

scanning. Nevertheless, there is a desire to be completely rid of mechanical scanning, resulting in a need for additional ideas in this manner.

6.3.6 Summary

It appears that while chromatic confocal microscopy may prove to be a challenging method to implement at first, the strong gains in signal acquisition time makes the process worthwhile. A carefully chosen incident broadband light source, coupled with a worthy non-achromatic objective and spectrometer would result in an extremely efficient device while obtaining sufficient sampling at high resolutions. The fiber optics could make the scan head portable for easier sampling of subjects *in vivo*. The future of this project lies in the ability to improve the versatility of this device, reduce overall scan time, and increase axial resolution to approach industry standards.

APPENDIX

1. IRB APPROVAL LETTER

MU **Institutional Review Board**
Health Sciences Section

University of Missouri-Columbia

School of Medicine/N521-D
One Hospital Drive
Columbia, MO 65212
PHONE (573) 882-3181
FAX (573) 884-4401
E-MAIL: irb@missouri.edu
WEB: www.research.missouri.edu/hsirb

December 3, 2008

Jeffrey LaCroix
Biological Engineering
254 Agricultural Engineering Building
Columbia, MO 65212

Dear Jeffrey LaCroix,

Regarding your application for approval of the research project, *Measuring dermal scattering using a prototype confocal scanner*, the Health Sciences Institutional Review Board (HS IRB) took the following action:

a. Approved your study through full board review on November 19, 2008.
b. Found this protocol, dated November 4, 2008 to impose minimal risk to the research participant.
c. Requires that the principal investigator obtain the informed written consent of each research participant.
d. Reviewed and approved the final version of the consent form on December 2, 2008. Please use the approved consent displaying the signed IRB approval box when consenting patients.
e. Reviewed and approved the final version of the assent form on December 2, 2008. Please use the approved assent displaying the signed IRB approval box when obtaining assent.
f. Under 45 CFR, 46.404, written child assent required if determined capable by the investigator. One parent signature is required on the consent form.
g. Reviewed and approved any advertisements or other recruitment materials that were submitted with your application.
h. The board determined the medical device in this study is a non-significant device for FDA purposes. NSR device studies must follow the abbreviated requirements at 21 CFR 812.2(b).
i. Reviewed and approved the HIPAA Authorization on December 2, 2008.
j. Approval for this protocol will expire on November 19, 2009. A Continuing Review Report must be submitted a minimum of one month prior to this date.
k. Upon completion of the study a Completion Form must be submitted to the HS IRB office. If the closure is not documented on the Completion Form, you may close the study at the time of the annual review.

Please reference **IRB Project # 1124077** in all future communications regarding this project.

Pursuant to the HS IRB conflict of interest policy, investigators who are HS IRB members do not vote on protocols in which they are involved.

Death occurring in a study at this site must be reported to the HS IRB office within 24 hours of occurrence, whether or not the death is related to the study. All on-site serious adverse events must be reported to the HS IRB office within five (5) days of occurrence.

No change may be made in an approved protocol or recruitment materials unless the change is submitted to and approved by the HS IRB.

Do not depend on the HS IRB for your record keeping. Pursuant to federal regulations, the IRB retains files of only three years after termination of a research project.

Sincerely,
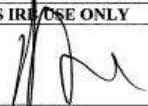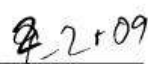
Niels Beck, PhD
Chair

Enclosure

109

2. ADULT CONSENT FORM

CONSENT FORM TO PARTICIPATE IN A RESEARCH STUDY

INVESTIGATOR'S NAME: JEFFREY T. LACROIX
PROJECT # 1124077
DATE OF PROJECT APPROVAL: NOVEMBER 19, 2008

FOR HS IRB USE ONLY
HS IRB Authorized Representative   Date
EXPIRATION DATE: 11-19-2009

STUDY TITLE: MEASURING DERMAL SCATTERING USING A PROTOTYPE CONFOCAL SCANNER

INTRODUCTION

This consent may contain words that you do not understand. Please ask the investigator or the study staff to explain any words or information that you do not clearly understand.

This is a research study. Research studies include only people who choose to participate. As a study participant you have the right to know about the procedures that will be used in this research study so that you can make the decision whether or not to participate. The information presented here is simply an effort to make you better informed so that you may give or withhold your consent to participate in this research study.

Please take your time to make your decision and discuss it with your family and friends.

You are being asked to take part in this study because you are a healthy human volunteer.

In order to participate in this study, it will be necessary to give your written consent.

WHY IS THIS STUDY BEING DONE?

The purpose of this study is to find out if a laser can be used to determine how much collagen (a protein that helps make up skin) is in your skin.

HOW MANY PEOPLE WILL TAKE PART IN THE STUDY?

About 150 people will take part in this study at the University of Missouri.

UMC, HS IRB: CONSENT   REVIEW #:
VERSION 1.4
NOVEMBER, 2004   1 of 5

WHAT IS INVOLVED IN THE STUDY?

Participation in this study will involve one visit to the MU Dermatology office, or one visit to 244 Bond Life Sciences Center, where you will place your hand on the scanning device.

The device will scan for about 10 seconds. We will repeat the experiment multiple times in order to make sure we have an accurate measurement.

HOW LONG WILL I BE IN THE STUDY?

We think you will be in the study for ten minutes, with no follow-up.

The investigator may decide to take you off this study if you are physically unable or uncomfortable.

You can stop participating at any time. Your decision to withdraw from the study will not affect you in any way.

WHAT ARE THE RISKS OF THE STUDY?

A laser is used in this procedure. It is never a good idea to look directly into the laser as eye damage can occur. However, as long as you do not stare at the laser directly coming from the scanner, and wear provided laser safety eyewear there is very low risk for eye damage from this procedure. You may experience a slight warm sensation on your hand due to the light.

> If you have any worrisome symptoms or symptoms that the investigator or his associates have described to you, notify the investigator immediately at 573-884-2862.

ARE THERE BENEFITS TO TAKING PART IN THE STUDY?

If you agree to take part in this study, there will not be direct medical benefit to you. You may expect to benefit from taking part in this research to the extent that you are contributing to medical knowledge. We hope the information learned from this study will benefit others in the future.

WHAT OTHER OPTIONS ARE THERE?

Instead of being in this study, an alternative is to not participate in this research study.

WHAT ABOUT CONFIDENTIALITY?

Information produced by this study will be stored in the investigator's file and identified by a code number only. The code key connecting your name to specific information about you will be kept in a separate, secure location. Information contained in your records may not be given to anyone unaffiliated with the study in a form that could identify you without your written consent, except as required by law. If the investigator conducting this study is not your primary, or regular doctor, he must obtain your permission before contacting your regular doctor for information about your past medical history or to inform them that you are in this trial.

It is possible that your medical and/or research record, including sensitive information and/or identifying information, may be inspected and/or copied by the study sponsor (and/or its agent), the Food and Drug Administration (FDA), federal or state government agencies, or hospital accrediting agencies, in the course of carrying out their duties. If your record is inspected or copied by the study sponsor (and/or its agents), or by any of these agencies, the University of Missouri will use reasonable efforts to protect your privacy and the confidentiality of your medical information.

The results of this study may be published in a medical book or journal or used for teaching purposes. However, your name or other identifying information will not be used in any publication or teaching materials without your specific permission.

WHAT ARE THE COSTS?

There is no cost to you for the laser scanning procedure.

Please note that added costs may include transportation, parking, and/or other possible expenses during your participation in this study. Please discuss these issues with the study investigator.

You will not be charged for experimental analysis of the data collected.

WILL I BE PAID FOR PARTICIPATING IN THE STUDY?

You will receive no payment for taking part in this study.

WHAT IF I AM INJURED?

It is not the policy of the University of Missouri to compensate human subjects in the event the research results in injury. The University of Missouri, in fulfilling its public responsibility, has provided medical, professional and general liability insurance coverage for any injury in the event such injury is caused by the negligence of the University of Missouri, its faculty and staff. The University of Missouri also will provide, within the limitations of the laws of the State of Missouri, facilities and medical attention to subjects who suffer injuries while participating in the research projects of the University of Missouri. In the event you have suffered injury as the result of participation in this research program, you are to contact the Risk Management Officer, telephone number (573) 882-1181, at the Health Sciences Center, who can review the matter and provide further information. This statement is not to be construed as an admission of liability.

WHAT ARE MY RIGHTS AS A PARTICIPANT?

Participation in this study is voluntary. You do not have to participate in this study. Your present or future care will not be affected should you choose not to participate. If you decide to participate, you can change your mind and drop out of the study at any time without affecting your present or future care in the University of Missouri. Leaving the study will not result in any penalty or loss of benefits to which you are entitled. In addition, the investigator of this study may decide to end your participation in this study at any time after he has explained the reasons for doing so and has helped arrange for your continued care by your own doctor, if needed.

UMC, HS IRB: CONSENT
VERSION 1.4
NOVEMBER, 2004

REVIEW #:

3 of 5

112

You will be informed of any significant new findings discovered during the course of this study that might influence your health, welfare, or willingness to continue participation in this study.

WHOM DO I CALL IF I HAVE QUESTIONS OR PROBLEMS?

If you have any questions regarding your rights as a participant in this research and/or concerns about the study, or if you feel under any pressure to enroll or to continue to participate in this study, you may contact the University of Missouri Health Sciences Institutional Review Board (which is a group of people who review the research studies to protect participants' rights) at (573) 882-3181
You may ask more questions about the study at any time. For questions about the study or a research-related injury, contact Jeffrey T. LaCroix via John A. Viator at 573-884-2862.

A copy of this consent form will be given to you to keep.

SIGNATURE

I confirm that the purpose of the research, the study procedures, the possible risks and discomforts as well as potential benefits that I may experience have been explained to me. Alternatives to my participation in the study also have been discussed. I have read this consent form and my questions have been answered. My signature below indicates my willingness to participate in this study.

_____   _____
Subject/Patient*   Date

_____   _____
Legal Guardian/Advocate/Witness (if required)**   Date

_____   _____
Additional Signature (if required) (identify relationship to subject)***   Date

*A minor's signature on this line indicates his/her assent to participate in this study. A minor's signature is not required if he/she is under 7 years old. Use the "Legal Guardian/Advocate/Witness" line for the parent's signature, and you may use the "Additional Signature" line for the second parent's signature, if required.

**The presence and signature of an impartial witness is required during the entire informed consent discussion if the patient or patient's legally authorized representative is unable to read.

***The "Additional Signature" line may be used for the second parent's signature, if required. This line may also be used for any other signature which is required as per federal, state, local, sponsor and/or any other entity requirements.

"If required" means that the signature line is signed only if it is required as per federal, state, local, sponsor and/or any other entity requirements.

SIGNATURE OF STUDY REPRESENTATIVE

I have explained the purpose of the research, the study procedures, identifying those that are investigational, the possible risks and discomforts as well as potential benefits and have answered questions regarding the study to the best of my ability.

_____   _____
Study Representative****   Date

****Study Representative is a person authorized to obtain consent. Per the policies of the University of Missouri Health Care, for any 'significant risk/treatment' study, the Study Representative must be a physician who is either the Principal or Co-Investigator. If the study is deemed either 'significant risk/non-treatment' or 'minimal risk,' the Study Representative may be a non-physician study investigator.

UMC, HS IRB: CONSENT
VERSION 1.4
NOVEMBER, 2004

REVIEW #:

5 of 5

114

3. ASSENT FORM AGE 12 AND OVER

ASSENT FORM TO PARTICIPATE IN A RESEARCH STUDY
NON-MEDICAL STUDY – AGE 12 AND OVER

INVESTIGATOR'S NAME: JEFFREY T. LaCROIX
PROJECT # 1124077
DATE OF PROJECT APPROVAL: NOVEMBER 19, 2008

FOR HS IRB USE ONLY
HS IRB Authorized Representative   12/2/08   Date
EXPIRATION DATE: 11-19-2009

STUDY TITLE: MEASURING DERMAL SCATTERING USING A PROTOTYPE CONFOCAL SCANNER

This is a study about how collagen (a protein that helps make up skin) scatters light in skin.

Why YOU are invited

You are invited to be in this study because your skin contains collagen, and we want to see how much collagen is there using a special light.

What will happen?

You will place your hand on top of the platform. A laser will shine on your skin. A device below your hand will scan for about 10 seconds. We will repeat the process a couple of times to make sure the data is accurate.

Can anything bad happen to me?

The procedure will be just like shining a bright light on the back of your hand. Nothing bad will happen to you from this laser. However, just to be safe, do not look directly into the laser.

Can anything good happen to me?

The results of this study may help others in the future

UMC, HS IRB: CONSENT   REVIEW #:
VERSION 1.4
NOVEMBER, 2004   1 of 2

What if I don't want to do this?

If you say you do not want to be in the study, you just have to tell us. No one will be mad at you. You can also say yes and later if you change your mind, you can quit the study. The choice is up to you.

Who will (know my answers, see my information)?

- We will do our best to make sure your (answers to these questions/information) is/are kept a secret.
- We will only use the information from this test to do a scientific study to help youth like you in the future.

Who can I talk to about the study?

You can ask questions any time. You can ask now. You can ask later. You can talk to me.

Do you have any questions about the study?

Do you want to be in the study?

☐ *YES*   ☐ *NO*

_____   _____
Signature of Youth   **Date**

UMC, HS IRB: CONSENT
VERSION 1.4
NOVEMBER, 2004

REVIEW #:

2 of 2

116

4. ASSENT FORM UP TO AGE 11

ASSENT FORM TO PARTICIPATE IN A RESEARCH STUDY
NON-MEDICAL STUDY – UP TO AGE 11

INVESTIGATOR'S NAME: JEFFREY T. LaCROIX
PROJECT # 1124077
DATE OF PROJECT APPROVAL: NOVEMBER 19, 2008

FOR HS IRB USE ONLY
HS IRB Authorized Representative   Date
EXPIRATION DATE: 11-19-8009

(signed) 12/2/08

STUDY TITLE: MEASURING DERMAL SCATTERING USING A PROTOTYPE CONFOCAL SCANNER

This is a study about how stretchy skin is.

Why YOU are invited

You are invited to be in this study because your skin is stretchy, and we want to see how stretchy your skin is using a special light.

What will happen?

You will place your hand on top of the platform. A bright light will shine on your skin. A device below your hand will raise and lower for about 10 seconds. We will repeat the process a couple of times to make sure everything worked properly.

Can anything bad happen to me?

The procedure will be just like shining a bright light on the back of your hand. Nothing bad will happen to you from this light. However, just to be safe, do not look directly into the bright light.

Can anything good happen to me?

The results of this study may help others in the future.

What if I don't want to do this?

If you say you do not want to be in the study, you just have to tell us. No one will be mad at you. You can also say yes and later if you change your mind, you can quit the study. The choice is up to you.

Who will (know my answers, see my information)?

- We will do our best to make sure your (answers to these questions/information) is/are kept a secret.
- We will only use the information from the light to do a scientific study to help children like you in the future.

Who can I talk to about the study?

You can ask questions any time. You can ask now. You can ask later. You can talk to me.

Do you have any questions about the study?
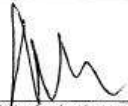
Do you want to be in the study?

☐ *YES*   ☐ *NO*

_____   _____
Signature of Child   **Date**

UMC, HS IRB: CONSENT
VERSION 1.4
NOVEMBER, 2004

REVIEW #:

2 of 2

118

5. HIPAA AUTHORIZATION FORM

HIPAA AUTHORIZATION FORM

Authorization for the Use and Disclosure of Personal Health Information Resulting from Participation in a Research Study

FOR HS IRB USE ONLY
12/2/08
HS IRB Authorized Representative   Date

Principal Investigator's Name: Jeffrey T. LaCroix
Project # 1124077
PROJECT TITLE: MEASURING DERMAL SCATTERING USING A PROTOTYPE CONFOCAL SCANNER

1. Description of the information
My authorization applies to the information described below. Only this information may be used and/or disclosed in accordance with this authorization: Name, age, sex, and Fitzpatrick skin type of participant.

2. Who may use and/or disclose the information
I authorize the following persons (or class of persons) to make the authorized use and disclosure of my PHI:
Jeffrey T. LaCroix, John A. Viator, Ph.D., Jon Dyer, M.D., Karen Edison, M.D.

3. Who may receive the information
I authorize the following persons (or class of persons) to receive my personal health information:
Jeffrey T. LaCroix, John A. Viator, Karen Edison, and Jon Dyer

4. Purpose of the use or disclosure
My PHI will be used and/or disclosed upon request for the following purposes:
☒ Auditing   ☐ My treatment during the study
☒ Study outcomes including safety and efficacy   ☒ Administrative and billing
☒ Submission to government agencies that may monitor the study
☒ Publications and presentations that may NOT identify me as a subject
☐ Other: _____

5. Expiration date or event
This authorization expires upon:
☐ The following date: _____
☒ End of research study
☐ No expiration date
☐ Other: _____

6. Right to revoke authorization
I understand that I have a right to revoke this authorization at any time. My revocation must be in writing in a letter sent to the Principal Investigator at 240C Life Sciences Center, Columbia, MO 65211. I am aware that my revocation is not effective to the extent that the persons I have authorized to use and/or disclose my PHI have already acted in reliance upon this authorization.

HIPAA Authorization
Version 2.1
February, 2003

Page 1

7. Statement that re-disclosures are no longer protected by the HIPAA Privacy Rule

I understand that my personal health information will only be used as described in this authorization in relation to the research study. I am also aware that if I choose to share the information defined in this authorization to anyone not directly related to this research project, the law would no longer protect this information. In addition, I understand that if my personal health information is disclosed to someone who is not required to comply with privacy protections under the law, then such information may be re-disclosed and would no longer be protected.

8. Right to refuse to sign authorization and ability to condition treatment, payment, enrollment or eligibility for benefits for research related treatment

I understand that I have a right not to authorize the use and/or disclosure of my personal health information. In such a case I would choose not to sign this authorization document I understand I will not be able to participate in a research study if I do not do so. I also understand that treatment that is part of the research project will be conditioned upon my authorization for the use and/or disclosure of my personal health information to and for use by the research team.

9. Suspension of right to access personal health information

I agree that I will not have a right to access my personal health information obtained or created in the course of the research project until the end of the study.

10. If I have not already received a copy of the University of Missouri Healthcare Privacy Notice, I may request one. If I have any questions or concerns about my privacy rights I should contact, the Privacy Officer at 573-882-9054.

11. Individuals' signature and date

I certify that I have received a copy of the authorization.

_____   _____
Signature of Research Participant   Date

_____   _____
Research Participant's Legally Authorized Representative   Date

_____
Describe Representative Authority to Act for the Participant

REFERENCES

1. Amos WB. Appendix I: Optical Units. In: Pawley JB, editor. Handbook of Biological Confocal Microscopy. Second ed. New York, NY: Plenum Press; 1995. p. 579-80.

2. Anderson RR, Parrish JA. The optics of human skin. J Invest Dermatol 1981 Jul;77(1):13-9.

3. Arifler D, Pavlova I, Gillenwater A, Richards-Kortum R. Light scattering from collagen fiber networks: micro-optical properties of normal and neoplastic stroma. Biophys J 2007 May 1;92(9):3260-74.

4. Booth MJ, Neil MA, Juskaitis R, Wilson T. Adaptive aberration correction in a confocal microscope. Proc Natl Acad Sci U S A 2002 Apr 30;99(9):5788-92.

5. Born M, Wolf E. Elements of the Theory of Diffraction. Principles of Optics: Electromagnetic Theory of Propagation Interference and Diffraction of Light. Sixth ed. Oxford, England; New York, NY: Pergamon Press; 1980. p. 370-458.

6. Brakenhoff GJ, Blom P, Barends P. Confocal scanning light microscopy with high aperture immersion lenses. Journal of Microscopy 1979;117(2):219-32.

7. Browne MA, Akinyemi O, Boyde A. Confocal surface profiling utilizing chromatic aberration. Scanning 1992;14(3):145-53.

8. Carlsson K. The influence of specimen refractive index, detector signal integration, and non-uniform scan speed on the imaging properties in confocal microscopy. J Microsc 1991 Aug;163(2):167-78.

9. Carlsson K, Åslund N. Confocal imaging for 3-D digital microscopy. Appl Opt 1987 Aug 15;26(16):3232-8.

10. Cheng PC, Kriete A. Image Contrast in Confocal Light Microscopy. In: Pawley JB, editor. Handbook of Biological Confocal Microscopy. Second ed. New York, NY: Plenum Press; 1995. p. 281-310.

11. Cheong WF, Prahl SA, Welch AJ. A review of the optical properties of biological tissues. Quantum Electronics, IEEE Journal of 1990;26(12):2166-85.

12.   Collier T, Arifler D, Malpica A, Follen M, Richards-Kortum R. Determination of epithelial tissue scattering coefficient using confocal microscopy. Selected Topics in Quantum Electronics, IEEE Journal of 2003;9(2):307-13.

13.   Collier T, Follen M, Malpica A, Richards-Kortum R. Sources of scattering in cervical tissue: determination of the scattering coefficient by confocal microscopy. Appl Opt 2005 Apr 10;44(11):2072-81.

14.   Corle TR, Kino GS. Confocal scanning optical microscopy and related imaging systems. San Diego: Academic Press; 1996.

15.   Delaney PM, Harris MR, King RG. Fiber-optic laser scanning confocal microscope suitable for fluorescence imaging. Appl Opt 1994 Feb 1;33(4):573-7.

16.   Diaspro A, Federici F, Robello M. Influence of Refractive-Index Mismatch in High-Resolution Three-Dimensional Confocal Microscopy. Appl Opt 2002 Feb 1;41(4):685-90.

17.   Driver I, Feather JW, King PR, Dawson JB. The optical properties of aqueous suspensions of Intralipid, a fat emulsion. Physics in Medicine and Biology 1989;34(12):1927-30.

18.   Dunn AK, Smithpeter C, Welch AJ, Richards-Kortum R. Sources of contrast in confocal reflectance imaging. Appl Opt 1996 Jul 1;35(19):3441-6.

19.   Eckes B, Krieg T, Nusgens BV, Lapiere CM. In vitro reconstituted skin as a tool for biology, pharmacology and therapy: a review. Wound Repair Regen 1995 Jul;3(3):248-57.

20.   Ehrmann RL, Gey GO. The growth of cells on a transparent gel of reconstituted rat-tail collagen. J Natl Cancer Inst 1956 Jun;16(6):1375-403.

21.   Elsdale T, Bard J. Collagen substrata for studies on cell behavior. J Cell Biol 1972 Sep;54(3):626-37.

22.   Everett MA, Yeargers E, Sayre RM, Olson RL. Penetration of epidermis by ultraviolet rays. Photochem Photobiol 1966 Jul;5(7):533-42.

23.   Farkas DL, Becker D. Applications of spectral imaging: Detection and analysis of human melanoma and its precursors. Pigment Cell Research 2001 Feb;14(1):2-8.

24.   Flock ST, Jacques SL, Wilson BC, Star WM, van Gemert MJ. Optical properties of Intralipid: a phantom medium for light propagation studies. Lasers Surg Med 1992;12(5):510-9.

25.   Fodor WL. Tissue engineering and cell based therapies, from the bench to the clinic: the potential to replace, repair and regenerate. Reprod Biol Endocrinol 2003 Nov 13;1:102.

26.   Fujimoto JG. Optical coherence tomography for ultrahigh resolution in vivo imaging. Nature Biotechnology 2003 Nov;21(11):1361-7.

27.   Garzón RJ, Meneses J, Tribillon G, Gharbi T, Plata A. Chromatic confocal microscopy by means of continuum light generated through a standard single-mode fibre. Journal of Optics A: Pure and Applied Optics 2004;6(6):544-8.

28.   Griffith LG, Naughton G. Tissue engineering - Current challenges and expanding opportunities. Science 2002 Feb 8;295(5557):1009-14.

29.   Haftek M, Mac-Mary S, Le Bitoux MA, Creidi P, Seite S, Rougier A, Humbert P. Clinical, biometric and structural evaluation of the long-term effects of a topical treatment with ascorbic acid and madecassoside in photoaged human skin. Exp Dermatol 2008 Nov;17(11):946-52.

30.   Harding CR. The stratum corneum: structure and function in health and disease. Dermatol Ther 2004;17 Suppl 1:6-15.

31.   Hrynchak P, Simpson T. Optical coherence tomography: An introduction to the technique and its use. Optometry and Vision Science 2000 Jul;77(7):347-56.

32.   Ilev I, Waynant R, Gannot I, Gandjbakhche A. Simple fiber-optic confocal microscopy with nanoscale depth resolution beyond the diffraction barrier. Review of Scientific Instruments 2007 Sep;78(9):093703-1-4.

33.   Inoué S. Foundations of Confocal Scanned Imaging in Light Microscopy. In: Pawley JB, editor. Handbook of Biological Confocal Microscopy. Second ed. New York,NY: Plenum Press; 1995. p. 1-17.

34. Izatt JA, Hee MR, Owen GM, Swanson EA, Fujimoto JG. Optical coherence microscopy in scattering media. Opt Lett 1994 Apr 15;19(8):590-2.

35. Juskaitis R, Wilson T. Imaging in reciprocal fibre-optic based confocal scanning microscopes. Optics Communications 1992 Sep 1;92(4-6):315-25.

36. Kafi R, Kwak HS, Schumacher WE, Cho S, Hanft VN, Hamilton TA, King AL, Neal JD, Varani J, Fisher GJ, Voorhees JJ, Kang S. Improvement of naturally aged skin with vitamin A (retinol). Arch Dermatol 2007 May;143(5):606-12.

37. Kino GS. Intermediate Optics in Nipkow Disk Microscopes. In: Pawley JB, editor. Handbook of Biological Confocal Microscopy. Second ed. New York, NY: Plenum Press; 1995. p. 155-65.

38. Kollias N. Polarized Light Photography of Human Skin. In: Wilhelm K-P, editor. Bioengineering of the Skin: Skin Surface Imaging and Analysis.Boca Raton: CRC Press; 1997. p. 95-104.

39. Kuehl RO. Experiments to Study Variances. Design of Experiments: Statistical Principles of Research Design and Analysis. Second ed. Pacific Grove, CA: Duxbury/Thomson Learning; 2000. p. 148-74.

40. L'Heureux N, Dusserre N, Marini A, Garrido S, de la Fuente L, McAllister T. Technology Insight: the evolution of tissue-engineered vascular grafts - from research to clinical practice. Nature Clinical Practice Cardiovascular Medicine 2007 Jul;4(7):389-95.

41. L'Heureux N, McAllister TN, de la Fuente LM. Tissue-engineered blood vessel for adult arterial revascularization. New England Journal of Medicine 2007 Oct 4;357(14):1451-3.

42. Lai JY, Chen KH, Hsiue GH. Tissue-engineered human corneal endothelial cell sheet transplantation in a rabbit model using functional biomaterials. Transplantation 2007 Nov 27;84(10):1222-32.

43. Mason RL, Gunst RF, Hess JL. Assessment of Model Assumptions. Statistical Design and Analysis of Experiments with Applications to Engineering and Science.New York, NY: John Wiley and Sons; 1989. p. 530-46.

44. Massig JH, Preissler M, Wegener AR, Gaida G. Real-time confocal laser scan microscope for examination and diagnosis of the eye in vivo. Appl Opt 1994 Feb 1;33(4):690-4.

45. Masters BR, Gonnord G, Corcuff P. Three-dimensional microscopic biopsy of in vivo human skin: a new technique based on a flexible confocal microscope. J Microsc 1997 Mar;185(Pt 3):329-38.

46. Masuda S, Shimizu T, Yamato M, Okano T. Cell sheet engineering for heart tissue repair. Advanced Drug Delivery Reviews 2008 Jan 14;60(2):277-85.

47. Minsky M, inventor; Microscopy Apparatus.3,013,467. 1961 Dec 19.

48. Moes CJM, van Gemert MJC, Star WM, Marijnissen JPA, Prahl SA. Measurements and calculations of the energy fluence rate in a scattering and absorbing phantom at 633 nm. Appl Opt 1989 Jun 15;28(12):2292-6.

49. Neuenschwander S, Hoerstrup SP. Heart valve tissue engineering. Transplant Immunology 2004 Apr;12(3-4):359-65.

50. Nordlund JJ. The melanocyte and the epidermal melanin unit: an expanded concept. Dermatol Clin 2007 Jul;25(3):271-81.

51. Patel DV, McGhee CN. Contemporary in vivo confocal microscopy of the living human cornea using white light and laser scanning techniques: a major review. Clin Experiment Ophthalmol 2007 Jan;35(1):71-88.

52. Rajadhyaksha M, Grossman M, Esterowitz D, Webb RH, Anderson RR. In vivo confocal scanning laser microscopy of human skin: melanin provides strong contrast. J Invest Dermatol 1995 Jun;104(6):946-52.

53. Ripandelli G, Coppe AM, Capaldo A, Stirpe M. Optical coherence tomography. Semin Ophthalmol 1998 Dec;13(4):199-202.

54. Ruprecht AK, Koerner K, Wiesendanger TF, Tiziani HJ, Osten W. Chromatic confocal detection for high-speed microtopography measurements. San Jose, CA, USA: SPIE; 2004 p. 53-60.

55. Ruprecht AK, Wiesendanger TF, Tiziani HJ. Chromatic confocal microscopy with a finite pinhole size. Opt Lett 2004 Sep 15;29(18):2130-2.

56.   Sakai S, Yamanari M, Miyazawa A, Matsumoto M, Nakagawa N, Sugawara T, Kawabata K, Yatagai T, Yasuno Y. In vivo three-dimensional birefringence analysis shows collagen differences between young and old photo-aged human skin. J Invest Dermatol 2008 Jul;128(7):1641-7.

57.   Sandison DR, Webb WW. Background rejection and signal-to-noise optimization in confocal and alternative fluorescence microscopes. Appl Opt 1994 Feb 1;33(4):603-15.

58.   Sandison DR, Williams RM, Wells KS, Strickler J, Webb WW. Quantitative Fluorescence Confocal Laser Scanning Microscopy (CLSM). In: Pawley JB, editor. Handbook of Biological Confocal Microscopy. Second ed. New York, NY: Plenum Press; 1995. p. 39-53.

59.   Sauermann K, Clemann S, Jaspers S, Gambichler T, Altmeyer P, Hoffmann K, Ennen J. Age related changes of human skin investigated with histometric measurements by confocal laser scanning microscopy in vivo. Skin Res Technol 2002 Feb;8(1):52-6.

60.   Schaudig U. [Optical coherence tomography]. Ophthalmologe 2001 Jan;98(1):26-34.

61.   Schmitt JM, Knüttle A, Yadlowsky M. Confocal microscopy in turbid media. J Opt Soc Am A 1994 Aug;11(8):2226-35.

62.   Schor SL, Court J. Different mechanisms in the attachment of cells to native and denatured collagen. J Cell Sci 1979 Aug;38:267-81.

63.   Serri R, Iorizzo M. Cosmeceuticals: focus on topical retinoids in photoaging. Clin Dermatol 2008 Nov;26(6):633-5.

64.   Sharma MD, Sheppard CJR. Axial resolution in the fibre-optical confocal microscope. Bioimaging 1998;6(2):98-103.

65.   Sheppard CJR, Gu M, Keith B, Zhou H. Influence of spherical aberration on axial imaging of confocal reflection microscopy. Appl Opt 1994 Feb 1;33(4):616-24.

66.   Sheppard CJR, Wilson T. The Image of a Single Point in Microscopes of Large Numerical Aperture. Proceedings of the Royal Society of London Series A, Mathematical and Physical Sciences 1982 Jan 8;379(1776):145-58.

67.　Shi K, Li P, Yin S, Liu Z. Chromatic confocal microscopy using supercontinuum light. Opt Express 2004 May 17;12(10):2096-101.

68.　Shimizu T, Yamato M, Kikuchi A, Okano T. Cell sheet engineering for myocardial tissue reconstruction. Biomaterials 2003 Jun;24(13):2309-16.

69.　Smithpeter CL, Dunn AK, Welch AJ, Richards-Kortum R. Penetration depth limits of in vivo confocal reflectance imaging. Appl Opt 1998 May 1;37(13):2749-54.

70.　Southwood WFW. The thickness of the skin. Plast Reconstr Surg (1946) 1955 May;15(5):423-9.

71.　Tabaksblat R, Meier RJ, Kip BJ. Confocal Raman microspectroscopy: Theory and application to thin polymer samples. Appl Spectrosc 1992;46(1):60-8.

72.　Török P, Wilson T. Rigorous theory for axial resolution in confocal microscopes. Optics Communications 1997 Apr 15;137:127-35.

73.　van Elburg HJ, Kuypers LC, Decraemer WF, Dirckx JJ. Improved correction of axial geometrical distortion in index-mismatched fluorescent confocal microscopic images using high-aperture objective lenses. J Microsc 2007 Oct;228(Pt 1):45-54.

74.　van Gemert MJ, Jacques SL, Sterenborg HJ, Star WM. Skin optics. IEEE Trans Biomed Eng 1989 Dec;36(12):1146-54.

75.　van Staveren HJ, Moes CJM, van Marie J, Prahl SA, van Gemert MJC. Light scattering in Intralipid-10% in the wavelength range of 400-1100 nm. Appl Opt 1991 Nov 1;30(31):4507-14.

76.　Vesely I. Heart valve tissue engineering. Circulation Research 2005 Oct 14;97(8):743-55.

77.　Visser TD, Oud JL, Brakenhoff GJ. Refractive index and axial distance measurements in 3-D microscopy. Optik 1992;90(1):17-9.

78.　Wan S, Anderson RR, Parrish JA. Analytical modeling for the optical properties of the skin with in vitro and in vivo applications. Photochem Photobiol 1981 Oct;34(4):493-9.

79.   Wang L, Jacques SL, Zheng L. MCML--Monte Carlo modeling of light transport in multi-layered tissues. Comput Methods Programs Biomed 1995 Jul;47(2):131-46.

80.   Wang L, Jacques SL, Zheng L. CONV--convolution for responses to a finite diameter photon beam incident on multi-layered tissues. Comput Methods Programs Biomed 1997 Nov;54(3):141-50.

81.   Washington N, Washington C, Wilson CG. Transdermal Drug Delivery. Physiological Pharmaceutics: Barriers to Drug Absorption. Second ed. London: Taylor and Francis; 2001. p. 181-98.

82.   Watson RE, Long SP, Bowden JJ, Bastrilles JY, Barton SP, Griffiths CE. Repair of photoaged dermal matrix by topical application of a cosmetic 'antiageing' product. Br J Dermatol 2008 Mar;158(3):472-7.

83.   Welzel J. Optical coherence tomography in dermatology: a review. Skin Research and Technology 2001 Feb;7(1):1-9.

84.   White CR, Barnhill RL. Alterations of Collagen and Elastin. In: Barnhill RL, Crowson AN, editors. Textbook of Dermatopathology. Second ed. New York: McGraw-Hill, Medical Pub. Division; 2004. p. 405-26.

85.   White JG, Amos WB, Fordham M. An evaluation of confocal versus conventional imaging of biological structures by fluorescence light microscopy. J Cell Biol 1987 Jul 1;105(1):41-8.

86.   Yang J, Yamato M, Nishida K, Hayashida Y, Shimizu T, Kikuchi A, Tano Y, Okano T. Corneal epithelial stem cell delivery using cell sheet engineering: Not lost in transplantation. Drug Targeting 2006;14(7):471-82.

87.   Yang J, Yamato M, Nishida K, Ohki T, Kanzaki M, Sekine H, Shimizu T, Okano T. Cell delivery in regenerative medicine: The cell sheet engineering approach. Controlled Release 2006 Nov 28;116(2):193-203.

VITA

Jeffrey Thomas LaCroix was born March 23, 1983 in Paducah, Kentucky. He graduated from Sacred Heart-Griffin High School in Springfield, Illinois in 2001, and was accepted into the Biological Engineering program at the University of Missouri in Columbia. Jeff graduated with a bachelor's degree in December 2004 before working for six-months as a non-degree graduate research assistant for Dr. Xudong Fan. He was awarded the Life Sciences Predoctoral Fellowship at the University of Missouri to begin his graduate work for Dr. Mark Haidekker in the department of Biological Engineering. Jeff graduated with his Ph.D. in May 2009 and now resides in Columbia, Missouri with his wife, Tiffany, and his dog, Maverick.